Gaseous Studies of Ionic Chromophores and Peptide Cation Radicals Generated from Electron Transfer

Robert Pepin

A dissertation

Submitted in partial fulfilment of the

Requirements for the degree of

Doctor of Philosophy

University of Washington

2016

Reading Committee:

František Tureček, Chair

Robert Synovec

Bo Zhang

Program Authorized to Offer Degree:

Department of Chemistry

University of Washington

Abstract

Gaseous Studies of Ionic Chromophores and of Peptide Cation Radicals Generated from Electron Transfer

Robert H. Pepin

Chair of the Supervisory Committee:

Professor František Tureček

Department of Chemistry

Electron transfer to multiply protonated peptide cations from anion radical donors in the gas phase has become an increasingly popular method for peptide and protein sequence analysis. Electron Transfer Dissociation (ETD) of peptides generate energetic cation radical species which usually undergo non-specific N-C_α bond dissociation to generate N-terminal ***c*** fragments and C-terminal $\boldsymbol{z}^{\bullet}$ radical fragments. The mechanism by which this N-C_α bond dissociation occurs is not yet fully understood. With ETD's ability to preserve labile post translational modifications and thereby aid in the localization of modified amino acid residues it becomes easier for clinicians to understand abnormalities in proteoforms and thus more accurately diagnose and treat cancers. Given the potential for personalized medicine afforded by proteomics it is certainly a worthy goal to further our understanding by which the ETD fragmentation process works. Theoretical and experimental investigations reported herein are all targeted towards elucidating

ETD fragmentation mechanistic details be it conformational effects, energy distribution or electronic structure of peptide cation radicals in the gas phase.

Theoretical modeling of model systems has suggested several aspects of the fragmentation mechanism for electron based fragmentation methods, such as ETD. Calculations indicate that in the presence of a remote charge amide groups can capture electrons and become superbases, abstracting protons from even the highly basic arginine guanidinium group and facilitating formation of labile aminoketyl radicals leading to N-C_α bond dissociations. A thorough computational and experimental study of the ETD behavior of a relatively simple Gly-Leu-Gly-Gly-Lys pentapeptide is presented wherein electron attachment at various amide groups along the peptide backbone are modeled and shown to lead to the formation of the ETD products experimentally observed.

Electron Capture Dissociation (ECD), a fragmentation method related to ETD, at very cold temperatures has been shown to have a reduced number of backbone cleavages when compared to ambient temperature measurements. This demonstrates the importance of peptide ion conformation in the gas phase when activated by electrons. In a study of a series of heptapeptide ions designed to have tightly folded conformations in the gas phase, it was found that low energy conformer searching, subsequent collision cross section calculations and experimentally derived cross sections are insufficient to distinguish between low energy peptide ion conformers on their own and that an additional structure probing method was needed. ETD fragmentation of these ions did show interesting effects that can be ascribed to the tightly compact structures the ions were designed with.

A defining aspect of the initially proposed mechanism for ECD was that fragmentations occurred before energy redistribution and randomization; that is, ECD was considered to be a

non-ergodic process. We present an experimental study utilizing the secondary radical-induced dissociation of the leucine side chain as a "thermometer" for the energies involved in the ETD process and arrive at the conclusion that ETD must be an ergodic process and that the neutral electron donor molecule formed by the ETD reaction cannot be formed in an excited electronic state.

In a further attempt to probe the 3-D conformations of peptide ions in the gas phase, we are exploring the use of diazirine-carbene insertion photochemistry as a way of freezing gas phase conformations of peptide ions and interrogating these ions via various fragmentation methods in an attempt to locate the correct predicted ion conformations. We present here a study of a newly developed amino acid, photo-lysine, which is tagged with a diazirine chromophore for carbene insertion reactions. In order to more fully understand the factors which lead to a successful bond insertion reaction, non-covalent complexes of proton bound peptide dimers are formed via electrospray ionization, covalently "stitched" together and then analyzed for trends involving stitching efficiency and localization of the insertion point.

Finally, initial ion absorbance action spectroscopy experiments are reported. Knowledge of the gas phase absorbance behaviors of charge reduced peptide cation radicals and studies of the $\boldsymbol{z}^{\bullet}$ radical fragments both generated via electron transfer will be useful in probing the electronic structures of these ions and thus the mechanistic details of ETD in more depth. Presented here is the action spectroscopy of two common organic dye molecular ions and a study of the absorbance bands of the diazirine chromophore in the newly synthesized photo-lysine amino acid as a prelude to peptide cation radical studies.

Table of Contents

Acknowledgments

I would like to thank my advisor, Professor František Tureček, for his years of support and guidance during my graduate career. You are a wonderful mentor and generous in providing me with many opportunities to grow as a scientist. Your collaborative nature and enthusiasm for your field have given me an excellent model for how to grow myself as a scientist in the future.
I would like to thank my exam committee for agreeing to serve in this capacity. I would not be able to advance without your participation.
I would like to thank the Department of Chemistry at the University of Washington for admitting me to the program and allowing me to earn my doctorate.
I would like to thank all members of the Tureček research group, past and present, each of you contributed in some way to making me the doctoral graduate I am now. I would especially like to thank Drs. Mariana Barcenas and Christopher Shaffer for reading draft chapters of my dissertation. Your contributions and assistance are greatly appreciated.
I would like to thank all of my friends and family for their support and patience. I appreciate your forgiveness for those times when I couldn't participate in gatherings or parties because I "had to write."
I would also like to acknowledge the faculty and staff of the Pacific Lutheran University Chemistry department. Your efforts, and the design of your curriculum, during my undergraduate years made me an exceptionally well prepared candidate for graduate studies.
Finally, funding from the National Science Foundation (Grant # CHE-1359810) is appreciated.

Dedication

This dissertation is dedicated to my parents Anthony Pepin and Marie Hollinshead. Your love and support and belief in education inspired me to pursue this course. This is also dedicated to my wife Christina. Quite simply this would not have been possible without your love and support and I thank you for sharing my passion for higher education. Finally, this dissertation is dedicated to the memory of my son Ethan Thomas Pepin. I miss you every day and I pray that I am someone you would have been proud of.

Chapter 1.

Introduction.

1.1 Mass Spectrometry

At its most basic level, a mass spectrum is a histogram showing a range of mass to charge ratios, often abbreviated as m/z, and the relative amounts to which those m/z values are detected. A mass spectrometer is an instrument which outputs such a spectrum. Defining characteristics of a mass spectrometer include that the instrument have a way of generating ions, an *ion source*, a way of sorting ions, a *mass analyzer*, and a way of counting the sorted ions, a *detector*. These are not the only components possible to have in a mass spectrometer by a long ways, but all instruments which have these basic unifying features can be labeled as mass spectrometers.

The reputed father of mass spectrometry, Sir J.J. Thomson, had an instrument which the modern mass spectrometrist might have difficulty as recognizing to be the ancestor of their own modern instruments.

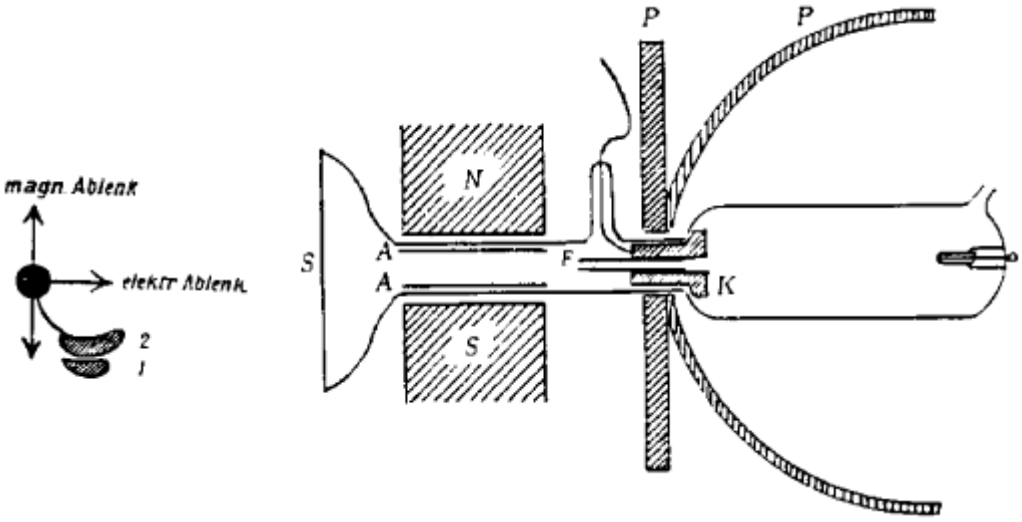

Figure 1: A drawing of Sir J.J. Thomson's first mass spectrometer. Image taken from http://www.scielo.br/img/fbpe/bjp/v29n3/401f7.gif

This instrument, shown in Figure 1 above, has all the elements which define a mass spectrometer. An electrical discharge is created between cathode K and the unlabeled anode at the right of the sample chamber. This electrical discharge will create both positive and negative ions out of any gases contained within the sample chamber. This *ion source* is non-specific in that it may make ions out of all gases present in the chamber and as such particular care must be made to introduce pure samples. The ions generated by the discharge then pass through the orifice of the cathode and between parallel plates A which are electrically charged to some fixed value and are themselves between the positive (N) and negative (S) poles of a magnet. These electrostatic and magnetostatic fields will cause some deflection of the path of the ions which vary by the mass to charge ratios of the ions and so work as a *mass analyzer*. Finally the ions hit a phosphorescent screen and are *detected* via the color induced by their collisions with the screen in positions that were functions of their mass to charge ratios.[1]

1.1.1. Ion Sources

Sir J.J. Thomson's ionization source, while crude by today's standards, provided the inspiration for all ion sources which followed. The most common ion source for decades was the electron impact ionization source. Gaseous samples of analytes to be studied were flowed into the ionization chamber at 10^{-5} Torr. Electron were emitted from a heated filament, accelerated, directed inside the chamber where they collide with some analyte molecules, ejecting electrons and creating ions. These ions can then be sorted by means of a suitable mass analyzer and detected. This method was simple, robust and reliable but had some experimental drawbacks. There was a practical limit to the size of molecule that could be analyzed as it required the molecule to be volatile enough to be able to vaporized. As a general rule, one could not expect to measure an analyte any higher than m/z 1200. This was also a "hard" ionization method. The

electron impacts transferred much energy into analyte molecules and could often result in the fragmentation of the molecule before detection. This would complicate spectral analysis, especially in the case of identification of unknown compounds as there might be no signal from a molecular ion.

A lack of molecular ion could be a big problem for identification of unknown compounds. For more fragile compounds, the "hardness" of the electron impact made analysis by mass spectrometry difficult, if not impossible. A new method was developed for ionizing more fragile compounds during the 1960s which was a much "softer" method.[2] Conceptually, chemical ionization involved increasing the pressure in the electron impact source. At approximately 0.5 - 1 Torr of a reagent gas such as H_2O or CH_4 the analyte becomes a minor component in the source region allowing reactions between reagent gas molecules. Collisions with high energy electrons from the filament causes these reagent gases to form highly reactive species as shown below in the case of positive polarity chemical ionization.

$$CH_4 + e^-(\sim 200eV) \text{ -----> } CH_4^{+\bullet} + 2e^-$$

In this example, the highly reactive methane cation radical is then free to react with other non-ionized methane molecules, as shown.

$$CH_4^{+\bullet} + CH_4 \text{ -----> } CH_5^+ + CH_3^\bullet$$

This protonated methane can now transfer a charging proton to an analyte of interest. This method relies on generating reagent cations which are gas phase acids capable of transferring a proton to the analytes of interest. Careful selection of reagent gas would minimize any exothermicity for the ionization of the analytes and lead to stable molecular ions for the analyte.

In negative polarity chemical ionization the conceptual model of an electron impact source operating at higher pressures still holds true, though the mechanism of interaction relies

on gas phase electron affinity rather than proton affinity. As an example consider the negative chemical ionization of fluoranthene in N_2 gas. When struck by a high energy electron, diatomic nitrogen gas will eject lower energy electrons, as shown below.

$$N_2 + e^-(\text{high eV}) \text{ ----> } N_2^{+\cdot} + e^-(\text{high eV}) + e^-(\text{thermal})$$

$$C_{16}H_{10} + e^-(\text{thermal}) \text{ ----> } C_{16}H_{10}^{-\cdot}$$

The thermal electrons ejected by the nitrogen are then absorbed by analyte molecules provided they have sufficient electron affinity. If the nitrogen gas were to have a higher electron affinity than the fluoranthene, it is unlikely that the fluoranthene would retain the electron.

Chemical and electron impact ionizations were the most common forms of mass spectrometric ionization sources for decades and were applied to a great variety of applications. These applications were all limited to certain classes and masses of compounds because both methods still required the analyte to be volatile. In 1984, John Fenn published a new method of ionization of molecules which did not have this difficulty with volatility and thus enabled the ionization of much larger and non-volatile compounds.[3,4] Not long afterwards this method of ionization began to appear in many places in the literature which was a strong indicator for the utility of the method. John Fenn shared the 2002 Nobel Prize in Chemistry for his invention of this method. Electrospray Ionization (ESI) enabled the transfer to the gas phase of ions with extraordinarily high masses and extremely low volatilities including synthetic polymers, large proteins, carbohydrates and nucleic acids.[5] ESI is considered a "soft" ionization method in that it transfers ions to the gas phase with a small enough amount of energy deposited in the analytes leading to little, if any, bond breakage. Thus, the vast majority of ions generated via ESI are molecular ions. An additional benefit of the ESI method is that it creates multiple charge states for many molecules which is especially useful when considering biomolecules which have mass

on the order of 10,000-1,000,000+ daltons. Few mass analyzers can sort ions with an m/z of 1,000,000, but some can handle m/z 10,000 (mass of 1,000,000 but charge state of z = 100). ESI also proved to be readily interfaced with liquid chromatography instruments allowing separations and online analysis of complex mixtures such as enzymatic digestions of proteins and cell lysates.

ESI is accomplished by application of a high strength potential difference between an atmospheric inlet and the pointed tip of a sample-containing capillary. The combination of the analyte solution's surface tension, the pressure from the capillary (supplied via a chromatographic system or a syringe pump) and the high strength potential difference between

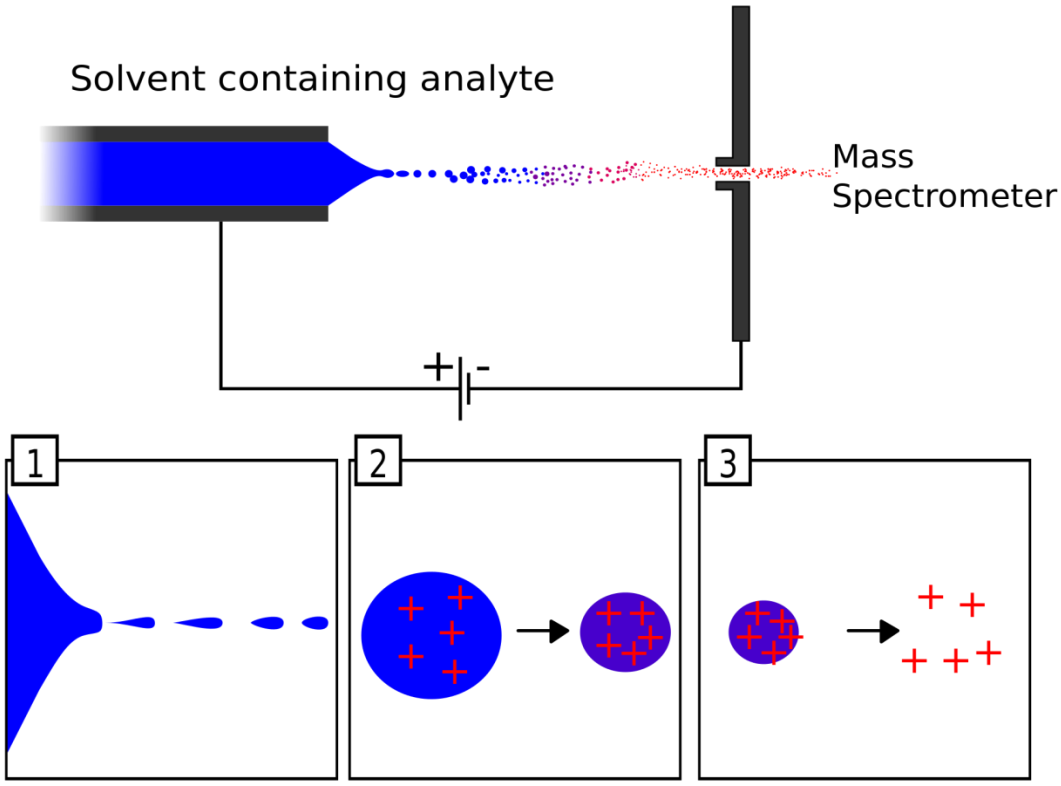

Figure 2: Cartoon schematic of Electrospray Ionization. Subpanel 1 shows the tip of a Taylor cone emitting charged droplets. Subpanel 2 shows droplet evaporation to produce a highly charged droplet. Subpanel 3 shows a highly charged droplet having reached the Raleigh limit and the resultant bare ions that are produced. Image taken from: https://upload.wikimedia.org/wikipedia/commons/thumb/b/b4/Electrospray_Ionization_Spectroscopy.svg/2000px-electrospray_Ionization_Spectroscopy.svg.png

the capillary tip and the atmospheric inlet lead to the formation of a Taylor Cone which is a very sharply pointed needle of solution. Charged droplets are then emitted from the tip of the Taylor Cone. These droplets are then attracted down the potential gradient to the atmospheric inlet at which point completely desolvated ions enter the vacuum manifold and are steered via ion optics into a mass analyzer as shown in the cartoon of Figure 2. The mechanism whereby these ions are desolvated and the charges apportioned is still an open question in the literature. The charge residue mechanism[6] and the ion evaporation mechanism are the leading candidate mechanisms. In the ion evaporation mechanism, charged droplets emitted from the Taylor Cone are subjected to evaporation of neutral solvent molecules until the droplet reaches the Rayleigh stability limit for the amount of charge that can be present on a droplet of that size and remain intact. As this limit is passed, smaller droplets bud off the parent droplet and form even more highly charged droplets which then follow the same pattern until all solvent molecules are evaporated and the ions are bare. The charge residue mechanism assumes that the Taylor cone produces droplets small enough that only one analyte molecule is present in each droplet and that the ions are exposed by solvent evaporation.[6] The Rayleigh limit is then invoked to explain how many charges can be attached to the analyte. The ions are typically charged by acidic protons from the electrospray solution, but other cations such as sodium or potassium are frequently found to provide charge as well.[7] Ions with low basicity can have their charge states increased by the adduction of transition metals in +2 and +3 oxidation states.[8] Electrospray ionization does generate negatively charged ions as well, but as the focus of this work is on ions generated from positive mode use, no further discussion of negative ion electrospray will be made here.

Electron impact, chemical ionization and electrospray are just a few of the modern methods of ionization available to mass spectrometrists today. Matrix assisted laser desorption[9]

ionization (MALDI), surface acoustic wave nebulization (SAWN)[10], desorption electrospray ionization (DESI)[11], fast atom bombardment (FAB)[12] as well as many other methods exist and are considered to be quite useful. This work is concerned only with ions generated via electrospray and as such none of these other ionization mechanisms will be discussed here.

1.1.2. Mass Analyzers

There are many different ways to sort ions. Sir J.J. Thomson's instrument used electrostatic and magnetostatic fields to simultaneously change the trajectory of ions as a function of their mass to charge ratio. Some modern mass spectrometers still make use of magnetostatic and electrostatic fields as mass analysis tools. These instruments are called "sector" type instruments as the ions are generally passed through the electrostatic or magnetostatic fields in separate regions or sectors. Depending on the particular sector instrument, rather high resolving powers can be obtained[13]. After generation of ions from any type of ion source, the ions are typically given some kind of acceleration before passing through the sectors. The ions are then separated in space as a function of their mass to charge ratio by the fields and detected. The time scale of mass spectrometric measurements made using a sector instrument is likely to be on the order of tens of microseconds or less.[14] Sector instruments then can be used to observe short lived species that other instruments with longer timescales would not observe.

In modern instruments, the quadrupole is by far the most common mass analyzer in use. Two pairs of rods are placed opposite to each other and are given AC and DC potentials with the AC frequency being in the radio frequency range. The rod pairs are given equal magnitude but opposite polarity AC potentials.

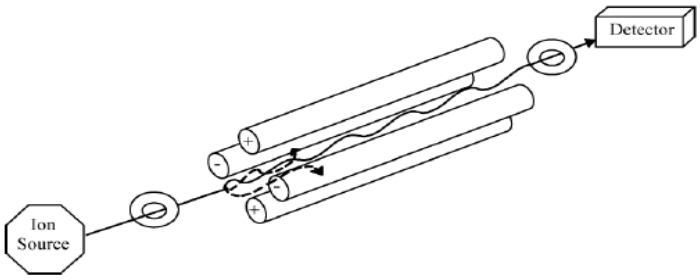

Figure 3: Schematic Diagram of a quadrupole mass filter. Taken from El-Aneed, A.; Cohen, A.; Banoub, J., Mass Spectrometry, Review of the Basics: Electrospray, MALDI and Commonly Used Mass Analyzers. *Applied Spectroscopy Reviews* 2009, 44(3), 210-330.

This creates a region where many mass to charge ratio ions have unstable trajectories. Only ions having a particular mass to charge ratio will pass through the quadrupole while all other ions will strike one of the rods and be neutralized.[15] By manipulation of the magnitudes of the AC and DC voltages, it is possible to scan a range of m/z values which will pass through the quadrupole thus generating a mass spectrum. Most gas chromatography-mass spectrometer hybrid (GC-MS) instruments use a single quadrupole mass analyzer to sort ions as they come off of the column. Quadrupoles are also used extensively in tandem mass spectrometer instruments as both reaction vessels for analyte fragmentation and as mass filters for selection of ions to be fragmented.

Other mass analyzer types, such as time-of-flight (TOF) and distance-of-flight[16] tubes exist, but are not used in the research presented in this work and so will not be discussed further.

1.1.3. Detectors

The detector used in Thomson's instrument was visual in nature. Ions of varying m/z would strike the detector in different positions changing the color of the screen in that position. Thomson measured the net deflection of the ions from center and quantitated the mass to charge of these ions by relating the magnetic and electric field strengths and the ions' deflections to known behaviors of ions moving in these fields. This detector did not allow for quantitation of

the number of ions hitting the detector, but it did allow the first experimental proof of the existence of atomic isotopes when he used it to measure the mass of neon.

Modern detectors are typically put to far more sophisticated applications than Thomson's detector, but they operate on fairy simple principles. Faraday cups are charged metal cups hooked up to a current meter. Whenever a charged ion (of opposite polarity) strikes the cup some electrons must move and the number of electrons can be measured via the current meter. The resulting current then measures how many ions are being delivered from the mass analyzer.

Electron multipliers (EM) are used as detectors in many modern mass spectrometers because of their high gain, fast response time and low noise. Ions striking a surface within the EM can cause electrons to be ejected from the surface and these electrons can then in turn be accelerated by a potential between that surface and another surface with this process repeated until the electrons are collected at an anode. The number of ions striking the surface will be proportional to the amount of electrons counted by the anode. Variations on EMs exist, such as the channel electron multipliers or microchannel plate detectors which can have implications for the types of experiments and instruments that these detectors can be used in.

1.2. Ion trapping

Many modern mass spectrometers have additional functional components in addition to the mandatory ion source, mass analyzer and detector components. One such component is what has come to be known as an ion trap. While strictly speaking, one could define an ion trap as a type of mass analyzer, the additional functionality of ion storage merits a separate discussion. Ion traps make use of the physics of quadrupolar fields and as such a deeper understanding of quadrupolar physics is necessary to understand the particular properties of trapped ions. This

section will give a brief overview of quadrupolar physics and then applications of that physics in both a traditional 3-D Paul trap and the more recent innovation, a 2-D linear trap.

1.2.1. 3-Dimensional Traps

Ions passing successfully passing through a quadrupole mass analyzer (see figure above) have a mass to charge ratio which allows them to maintain a steady trajectory when subjected to quadrupolar fields. For the purposes of discussion in this work, the term *quadrupolar* refers to fields with a quadratic dependence on distance from the generating electrodes, not the presence of four electrodes in the array.[15] If a quadrupole mass filter with ideal hyperbolic profiles is set up as shown in the figure above, and a potential of 2(U-Vcos(Ωt)) is applied across one pair of electrodes while -2(U-Vcos(Ωt)) is applied across the other pair of electrodes, the resulting electric field in the region between the rods is given in equation 1, below.

$$\emptyset_{x,y} = \frac{\emptyset_0}{r_0^2}(x^2 - y^2), \qquad \text{with } \emptyset_0 = 2(U + Vcos(\Omega t)) \qquad \textbf{(1)}$$

Splitting the field into components and considering each component individually gives the force in the x-direction as

$$F_x = -e\left(\frac{\partial \emptyset}{\partial x}\right)_y = -e\frac{\emptyset_0 x}{r_0^2} \qquad \textbf{(2)}$$

Recognizing that force is also equal to mass of the particle times the acceleration experienced by the particle, equation (2) becomes

$$m\left(\frac{d^2x}{dt^2}\right) = -2e\frac{(U+Vcos\,\Omega t)x}{r_0^2} \qquad \textbf{(3)}$$

which can be rearranged to equation (4)

$$\left(\frac{d^2x}{dt^2}\right) = -\left(\frac{2eU}{mr_0^2} + \frac{2eVcos\Omega t}{mr_0^2}\right)x \qquad \textbf{(4)}$$

And finally rearranged to equation (5)

$$\left(\frac{d^2x}{dt^2}\right) + \left(\frac{2eU}{mr_0^2} + \frac{2eVcos\Omega t}{mr_0^2}\right)x = 0. \qquad \textbf{(5)}$$

Equation (5) can be recognized as having the same form as the Mathieu Equation, a well-known differential equation with known solutions. A general form of the Mathieu Equation is shown in equation (6) with ξ defined as Ωt/2 with Ω having units of frequency as t is time and u represents displacement in some direction.

$$\left(\frac{d^2u}{d\xi^2}\right) + (a_u + 2q_u \cos 2\xi)u = 0. \qquad \textbf{(6)}$$

One can then see the relationships for a_u and q_u in equations (7)

$$a_u = \frac{8eU}{mr_0^2\Omega^2}, \qquad q_u = \frac{-4eV}{mr_0^2\Omega^2} \qquad \textbf{(7)}$$

An important consequence of the derivation of the a_u and q_u parameters is that ion trajectory stability is inversely proportional to the mass-to-charge ratio. Ion trajectory stability through the quadrupole mass filter is determined by β_u which is a complex function of a_u and q_u. Ions follow trajectories with complex harmonic oscillations along the x and y axes whose amplitudes are exponential functions of μξ. Stable trajectories result only when the trajectory amplitude does not increase with ξ, which holds only for μ = *i*β where β is not an integer and *i* is $\sqrt{-1}$. Thus, the boundaries between regions of stability in a-q space are the values for which β_u have integer values.

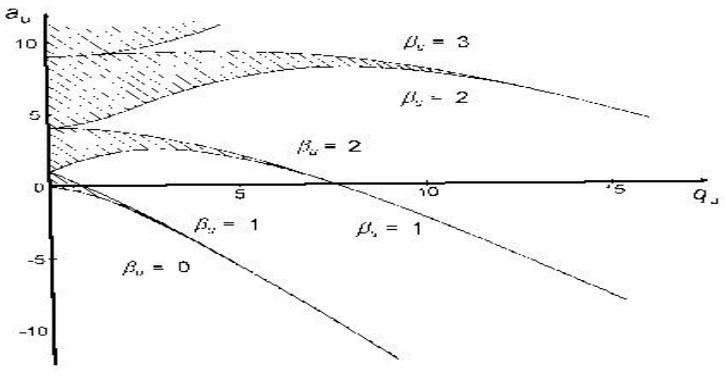

Figure 4: An example of a one dimensional Matheiu stability diagram. Shaded regions show which q and a values will lead to stable ion trajectories for the u dimension. Taken from www.physik.uni-mainz.de/werth/nlinres/pefig2s1.jpg

Figure 4 shows an example of a 1-dimensional Matheiu stability diagram. The requirement for a useful quadrupolar device is for the ion trajectory to be stable in both directions orthogonal to the ion's direction of travel. The overlap of these regions in a-q space would then describe the desired electric field conditions, as shown in Figure 5.

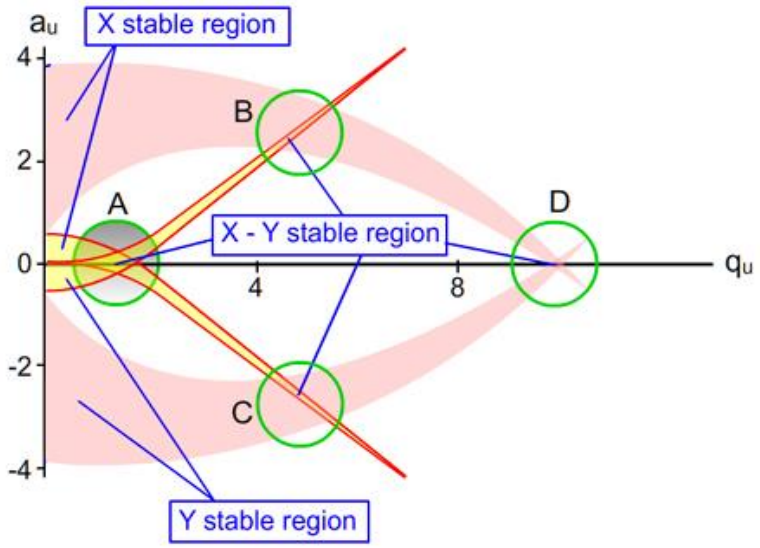

Figure 5: Overlaid stability diagrams for x and y dimensions. Regions A, B, C and D represent regions where ion trajectories are stable in both the x and y directions simultaneously. Ions passing through a quadruople mass filter in this example would be traveling in the z direction. Figure taken from www.chromacademy.com/essential-guide/dec2011/figure-05.jpg.

Most quadrupole mass filters will operate in the overlap region A shown in the Figure 3 above, but in principle any region of overlap could be used.

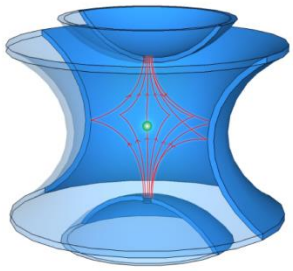

Figure 6: A drawing of a 3D ion trap consisting of a ring electrode and two end cap electrodes with hyperbolic surface geometry. Graphic taken from www.triumf.ca/sites/default/files/user-1029/Penning-Trap_1.png

A device having the cross section shape of four hyperbolic rods but having circular symmetry is shown in Figure 6. Two end cap electrodes are placed as shown in the figure relative to a ring electrode. This results in similar, but different, forms for the a and q values to what was shown above. Through a similar derivation and accounting for the cylindrical symmetry of the device one comes to the following equations for this geometry.

$$a_z = -\frac{16eU}{m(r_0^2+2z_0^2)\Omega^2} \qquad q_z = \frac{8eV}{m(r_0^2+2z_0^2)\Omega^2} \qquad a_z = -2a_r \qquad q_z = -2q_r \qquad \textbf{(8)}$$

Due to the differences in the symmetry of this device from that described above, the resulting stability diagrams do not have the same symmetric overlap defining regions of stability as before. Instead, the stability regions look like what is shown in Figure 7.

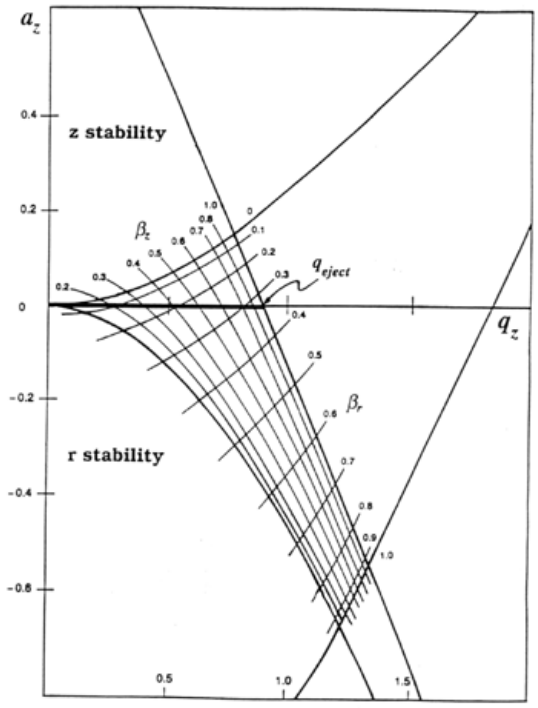

Figure 7: Stability diagram of a 3D ion trap. Due to the symmetries involved in the 3D trap, the stability diagram for the trap is not symmetric about the q axis. Graphic from https:/proteomicsresource.washington.edu/mascot/images /stability_diagram.gif

As can be clearly seen, the region of stability no longer is symmetric about the q axis. This device has come to be known as a Paul Trap or 3D trap. Its invention led to the 1989 Nobel Prize in Physics being awarded to Wolfgang Paul, Norman Ramsay and Hans Dehmelt (a member of the University of Washington Physics Department). The Paul trap was the standard ion trapping device for many years and much pioneering work in multi-stage mass spectrometry was performed using this device. However, little of the research reported in this work will make use of the 3D trap and as such the discussion is limited to what has been presented here and is to help place the 2D linear ion trap in proper context.

1.2.2. Linear Traps

Linear ion traps or 2D traps have several advantages over the classic 3D Paul trap. They retain the ability to resonantly excite and eject ions from the trap enabling multistage MS measurements (MS^n). The primary advantage is that the linear trap is less prone to space charge effects (too many charged species in a volume such that the mutually repelling charges perturb the path of the ions during ejection leading to incorrect mass assignment) owing to its physically bigger dimensions and higher ion trapping efficiencies. The stability diagram of a linear trap is symmetric about the q axis and is shaped exactly the same as the stability region of a quadrupole mass filter and is shown as the shaded region in Figure 6, below.

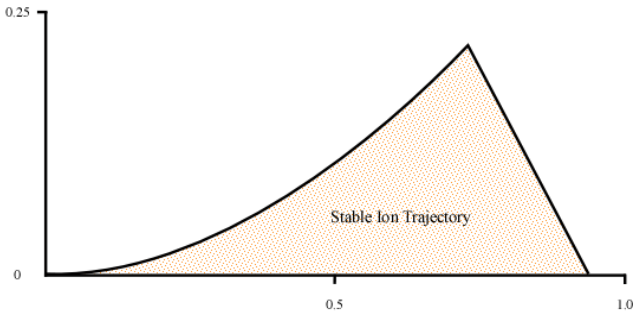

Figure 8: Region of x and y stability in q and a space for a linear ion trap. The region is symmetric about the q axis and so the portion corresponding to negative a values is often omitted. Graphic taken from: http://people.whitman.edu/~dunnivfm/C_MS_Ebook/CH5/Figures/Fig_5_13_Quad4.gif

Ions are trapped by placing a DC offset on to the stable ion potentials giving rise to stable ion trajectories in the radial direction and trapped axially by the application of DC potential to lenses at the front and rear of the trap.[15,17]

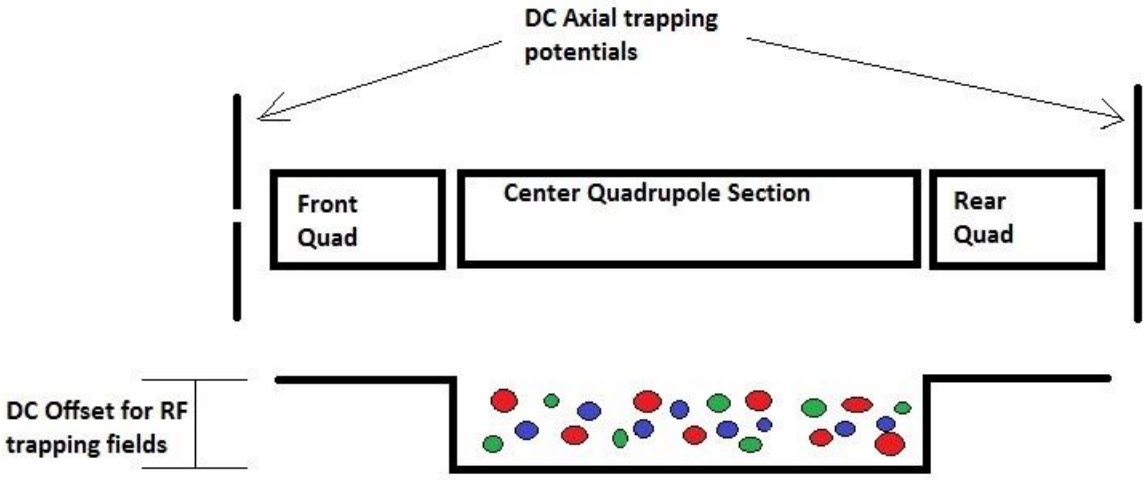

Figure 9: Cartoon drawing showing how ions are trapped in a linear trap. In addition to modulating RF potentials such that the ions have stable trajectories, a DC offset is applied to the trapping potentials to confine the ions radially and DC potentials are applied to front and back lenses for axial confinement.

Of particular interest to some of the research detailed in this work, the ions are tightly gathered around a central axis in the linear trap and as such the ion cloud is easily overlapped by a coaxial laser pulse.

1.3 Fragmentation Methods

As mentioned in the section regarding ionization sources, an instrument with an electrospray source has the advantage of delivering intact molecular ions to the gas phase. Because of the "softness" of the method, little structural information can be determined from the electrospray ionization mass spectrum, typically. Additional fragmentations must be applied to the analytes after ionization in order to determine any structural information. The following sections discuss a few fragmentation methods implemented on ion trap type mass spectrometers as well as a short description of the nomenclature for the fragments generated from these methods. The main focus of this work is peptide mass spectrometry and as such a more detailed description of peptide fragmentation techniques is in order.

1.3.1 Peptide fragmentation nomenclature

In a polypeptide there are three repeated backbone bond types. There are bonds between the carbonyl carbon and its alpha carbon (C-Cα), between the carbonyl carbon and the backbone nitrogen (amide bond) and bonds between backbone nitrogen and the alpha carbon (N-Cα). Fragmentation of the amide bond is typical of collision based fragmentation methods resulting in N-terminus containing ***b*** fragment ions and C-terminus containing ***y*** ions. Electron based methods have characteristic cleavages of the N-Cα bond which result in formation of N-terminal peptide amide ***c*** ions and C-terminal $\boldsymbol{z}^{\cdot}$ ion radical fragments. There are some experimental evidences for fragments which have the composition of having broken the C-Cα bond, though these are less commonly observed. A generic example of these fragment ion types and the backbone bond cleavages which lead to them are shown in Scheme 1 below.

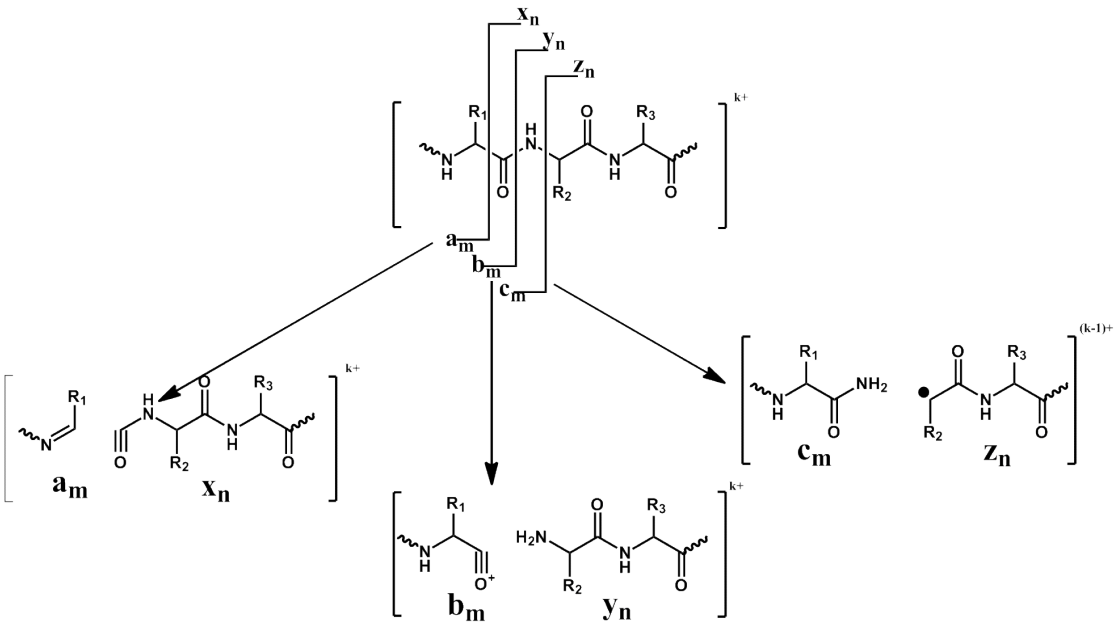

Scheme 1: Peptide backbone fragmentation scheme. Note that b ions are not believed to take an acylium ion type shape, but rather are expected to be oxazolones. Acylium shape is shown to clarify which bond is broken.

It should be noted that there is little experimental evidence for the existence of ***b*** ions as acylium ions as shown in the figure. Rather they are generally considered to take a protonated oxazalone structure. The example ***b*** ion in the figure is shown this way to clarify the location of the broken backbone bond. ***a*** type ions are the result of loss of CO from ***b*** ions and can be useful as a means of identifying the ion series type that an unknown m/z represents in a spectrum. ***x*** type ions have been reported as photodissociation products.[18]

Fragment ions are often observed which are not due solely to backbone dissociation such as fragments which contain neither the N nor the C termini or ones in which a secondary radical induced fragmentation has occurred. In the case where a secondary radical induced fragmentation has broken the beta-gamma carbon bond the resulting product ion is called a ***w*** ion. An example of a ***w*** fragment ion and the $z^{\bullet}$ ion radical it came from are shown in Scheme 2, below.

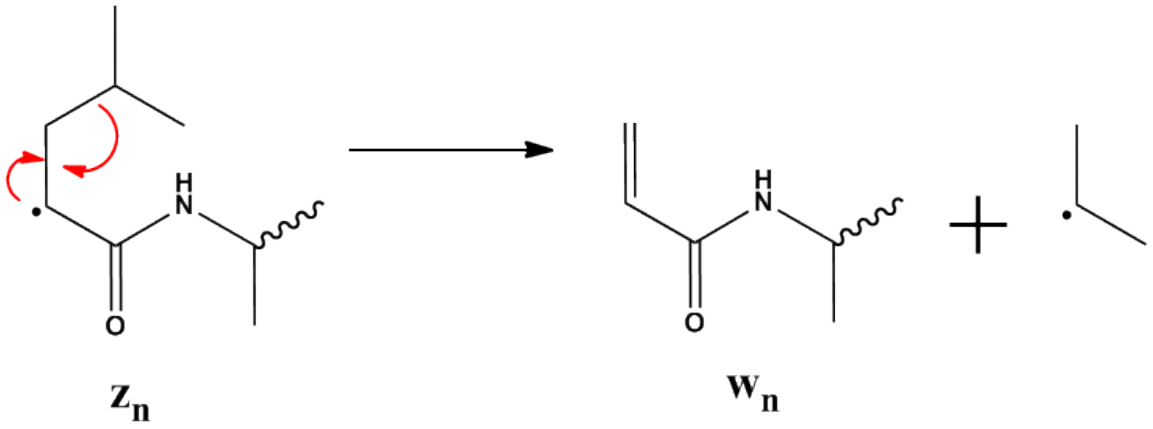

Scheme 2: Sequence ion z_n undergoing radical migration resulting in beta- gamma bond cleavage and formation of the w_n ion from a leucine residue.

1.3.2. Collision Induced Dissociation

Ions stored in ion traps are most commonly activated by collision induced dissociation (CID). Briefly, an additional A.C. potential is superimposed on top of the trapping potentials. This extra potential gives trapped ions extra kinetic energy causing them to have more collisions with the neutral bath gas of the trap. A substantial fraction of these collisions are inelastic with the extra energy translated into internal, vibrational energy distributed throughout the various available vibrational modes. Given a sufficient number of collisions, the internal energy of the ion rises until a vibrational mode exceeds the amount of energy necessary to break a bond and fragmentation occurs. CID, as implemented in ion traps, is considered a slow heating method because the number of collisions necessary to fragment ions is high.[19]

In this work, the majority of CID measurements presented will be activation of peptide ions. CID of peptide ions is explained by two models: the mobile proton and localized proton models. The mobile proton model applies to cases where the peptide has at least one more proton than number of highly basic sites. The extra energy imparted by CID causes the proton to move between various sites within the peptide including along the backbone amides. The presence of an extra proton attached to the backbone amide group causes the amide bond to

weaken and lowers the energy barrier for cleavage of that bond.[20] In some cases, the number of charging protons present on a peptide ion is equal to or less than the number of highly basic sites. In those cases, the proton is sequestered at the highly basic site (such as an arginine side chain) and is unable to cause fragmentation in the same way. The presence of acidic residues in the peptide sequence can often promote site specific fragmentation, as well. In this case the proton that is transferred to the peptide amide groups comes from the aspartic or glutamic acid side chain. Along with protonated histidines, these acidic proton driven cleavages are considered to be localized proton fragmentations because the charging protons are sequestered and not able to protonate amide groups.

1.3.3. Electron Based Fragmentation Methods (ExD)

Collision induced dissociation is a long standing technique for fragmenting ions in the gas phase. Ions in all charge states can be vibrationally heated to the point of fragmentation, but often the structural information generated from CID fragmentation of peptides is incomplete due to the sequestration of charge or the presence of a fragmentation-site-directing amino acid such as aspartic acid. Relatively new electron based fragmentation methods such as electron capture dissociation[21] or electron transfer dissociation[22] can often be more informative when it comes to sequencing peptide ions, particularly for higher charge state analytes.

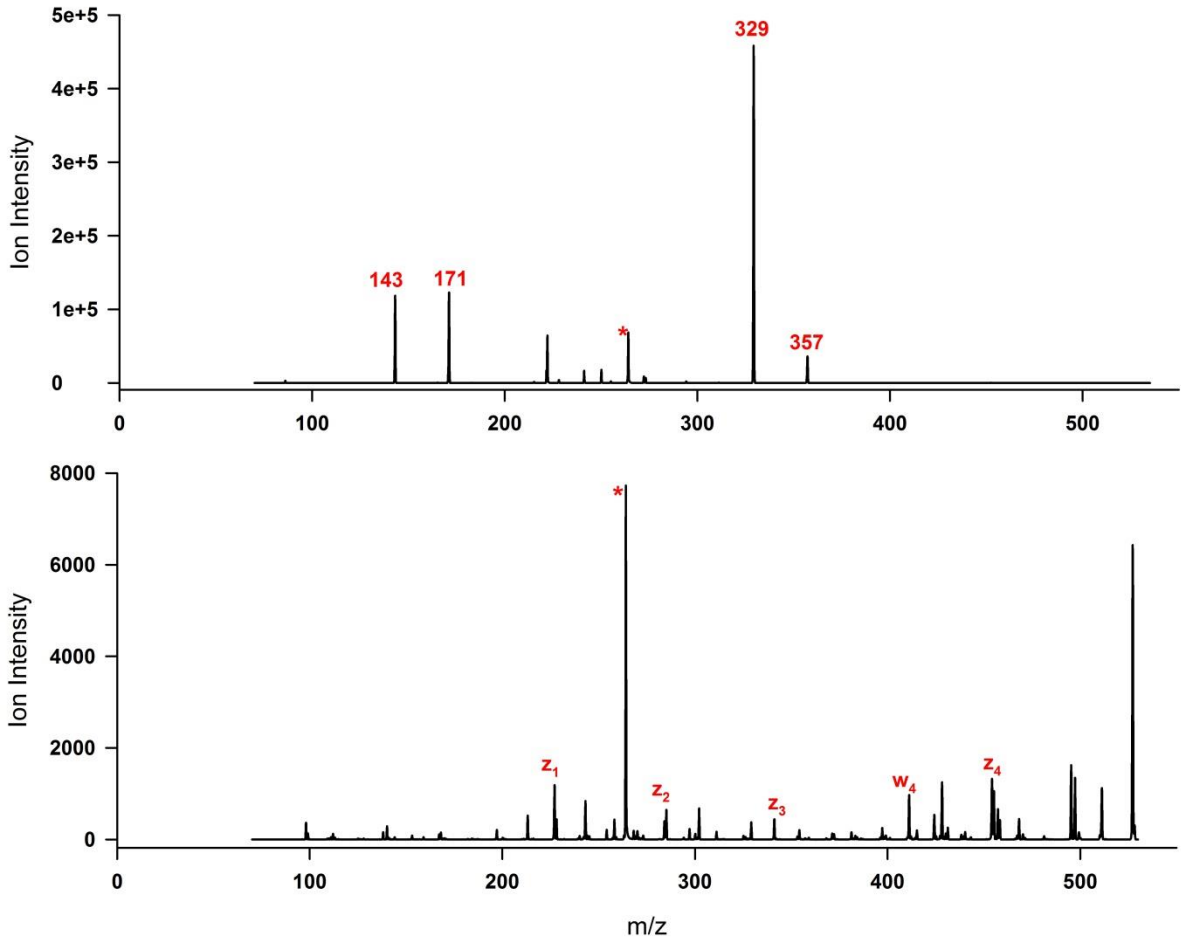

Figure 10: TOP: CID fragmentation of a doubly charged peptide ion. BOTTOM: ETD fragmentation of the same doubly charged ion.

Consider the two mass spectra shown in Figure 10 above. A doubly charged peptide ion was subjected to CID fragmentation in the top spectrum and the same ion was subjected to ETD in the bottom spectrum. In addition to the surviving doubly charged precursor ion, the CID based fragmentation yielded 4 sequence ions. If these were representative of 4 unique cleavage sites then it would be possible with the precursor mass to determine the amino acid sequence of this peptide. However, these 4 fragments actually represent cleavage at only a single backbone site. The dominant peak at m/z 329 is actually a sequence fragment which has lost a portion of an amino acid side chain (from m/z 357) as well. The peak at m/z 171 represents the

complementary portion of the peptide to the 329/357 pair while m/z 143 represents the loss of CO_2 from the 171 ion. So CID provided four redundant pieces of information towards sequencing in this case. In the bottom panel, the ETD spectrum of this peptide ion shows a much richer fragmentation as well as more sequence information. The fragments shown represent cleavage between all sets of residues leading to the complete peptide sequence information as well as side chain losses which can be diagnostic of isobaric residues of leucine/isoleucine.[23] This example is an extreme case, but in general the application of electron based methods of fragmentation yield improved sequence information and is complementary to collision based fragmentations.

Electron based fragmentation methods are relatively new fragmentation methods. The first paper describing ECD was in 1998[21] and the first paper describing ETD was in 2004.[22] Because of the relatively recent development of these methods, the mechanism by which ExD methods operate are not yet fully understood. Initial proposals from the McLafferty laboratory at Cornell University described the mechanism as involving the absorbance of electrons at charged sites followed by the transfer of a "hot hydrogen" to an amide group leading to backbone N-Cα bond cleavage of the charge-reduced peptide cation radical. The Cornell mechanism proposes a non-ergodic process; the proposed mechanism was too fast to allow redistribution of energy. A competing model for ExD has since been proposed by the Simons research group at the University of Utah and the Tureček research group at the University of Washington. The models proposed by Simons and Tureček are different, but very similar and are often referred to collectively as the UW model. The UW model relies on computational and experimental evidence to propose a method which is ergodic and which proposes that the reactant electrons enter into backbone amide orbitals rather than charge site amine, imidazole or guanidine groups.

Both the Cornell and UW models require knowledge of peptide ion conformation as well owing to the results of cold temperature ECD experiments which show backbone cleavages at fewer sites than ambient temperature ECD.[24]

Much of the work reported here is designed to probe the mechanism of ExD fragmentation. Chapter 3 details study of conformational effects on fragmentation patterns. Chapter 2 provides a detailed computational and experimental study of a simple pentapeptide and includes computational data which shows possible routes for the generation of all major fragment ions generated from ETD of the doubly charged precursor. Chapter 4 details the creation and use of a "thermometer ion" to probe the energetics of the ETD process. Chapter 5 presents some work studying the process by which diazirine derived carbenes perform bond insertion reactions with an eye towards conformational study applications for gas phase ions. Chapter 6 details some initial experiments with action spectroscopy of gas phase ions. The ability to probe the absorbance of gas phase ions will eventually lead to information about the structures of peptide cation radical $\boldsymbol{z}^{\bullet}$ fragments as well as intact charge-reduced peptide cation radicals generated from electron transfer.

1.4 References

(1) Thomson, J. J. *Rays of Positive Electricity and their Application to Chemical Analyses*; 1913.

(2) Munson, M. S. B.; Field, F. H. *J. Am. Chem. Soc.* **1966**, *88* (12), 2621–2630.

(3) Yamashita, M.; Fenn, J. B. *J. Phys. Chem.* **1984**, *88*, 4451–4459.

(4) Yamashita, M.; Fenn, J. B. *J. Phys. Chem.* **1984**, *88*, 4671–4675.

(5) Yamashita, M.; Fenn, J. B. *Iyo Masu Kenkyukai Koenshu* **1984**, *9*, 203–206.

(6) Wilm, M. *Mol. Cell. Proteomics* **2011**, *10* (7), M111.009407.

(7) Kruve, A.; Kaupmees, K.; Liigand, J.; Oss, M.; Leito, I. *J. Mass Spectrom.* **2013**, *48* (6), 695–702.

(8) Watson, H. M.; Vincent, J. B.; Cassady, C. J. *J. Mass Spectrom.* **2011**, *46* (11), 1099–1107.

(9) Kaufmann, R. *J. Biotechnol.* **1995**, *41* (2-3), 155–175.

(10) Huang, Y.; Yoon, S. H.; Heron, S. R.; Masselon, C. D.; Edgar, J. S.; Tureček, F.; Goodlett, D. R. *J. Am. Soc. Mass Spectrom.* **2012**, *23* (6), 1062–1070.

(11) Nefliu, M.; Smith, J. N.; Venter, A.; Cooks, R. G. *J. Am. Soc. Mass Spectrom.* **2008**, *19* (3), 420–427.

(12) Barber, M.; Bordoli, R. S.; Sedgwick, R. D.; Tyler, A. N. *Chem. Commun.* **1981**, 325–327.

(13) McBay, E. H.; Glish, G. L.; McLuckey, S. A.; Bertram, L. K. *Proc Conf Anal Chem Energy Technol Anal. Chem. Instrum.* 1986.

(14) Støchkel, K.; Milne, B. F.; Nielsen, S. B. *J. Phys. Chem. A* **2011**, *115* (11), 2155–2159.

(15) March, R. E.; Todd, J. F. J. *Quadrupole Ion Trap Mass Spectrometry, Second Edition*; 2005.

(16) Gundlach-Graham, A.; Dennis, E. A.; Ray, S. J.; Enke, C. G.; Barinaga, C. J.; Koppenaal, D. W.; Hieftje, G. M. *J. Anal. At. Spectrom.* **2013**, *28* (9), 1385–1395.

(17) Schwartz, J. C.; Senko, M. W.; Syka, J. E. P. *J. Am. Soc. Mass Spectrom.* **2002**, *13* (6), 659–669.

(18) Wysocki, V. H.; Resing, K. A.; Zhang, Q.; Cheng, G. *Methods* **2005**, *35* (3), 211–222.

(19) Sleno, L.; Volmer, D. A. *J. Mass Spectrom.* **2004**, *39* (10), 1091–1112.

(20) Wysocki, V. H.; Tsaprailis, G.; Smith, L. L.; Breci, L. A. *J. Mass Spectrom.* **2000**, *35* (12), 1399–1406.

(21) Zubarev, R. A.; Kelleher, N. L.; McLafferty, F. W. *J. Am. Chem. Soc.* **1998**, *120* (13), 3265–3266.

(22) Syka, J. E. P.; Coon, J. J.; Schroeder, M. J.; Shabanowitz, J.; Hunt, D. F. *Proc. Natl. Acad. Sci. U. S. A.* **2004**, *101* (26), 9528–9533.

(23) Tureček, F.; Julian, R. R. *Chem. Rev.* **2013**.

(24) Mihalca, R.; Kleinnijenhuis, A. J.; McDonnell, L. A.; Heck, A. J. R.; Heeren, R. M. A. *J. Am. Soc. Mass Spectrom.* **2004**, *15* (12), 1869–1873.

Chapter 2.

Comprehensive Analysis of Gly-Leu-Gly-Gly-Lys Peptide Dication Structures and Cation Radical Dissociations Following Electron Transfer: From Electron Attachment to Backbone Cleavage, Ion-Molecule Complexes, and Fragment Separation

Reproduced in part with permission from Pepin, Robert; Laszlo, Kenneth J.; Peng, Bo; Marek, Aleš; Bush, Matthew F.; and Tureček, František, J. Phys. Chem. A. Vol 118, No 1, Jan 9, 2014 pp308-324. Copyright 2014.

Abstract

Experimental data from ion mobility measurements and electron transfer dissociation were combined with extensive computational analysis of ion structures and dissociation energetics for Gly-Leu-Gly-Gly-Lys cations and cation radicals. Experimental and computational collision cross sections of $(GLGGK +2H)^{2+}$ ions pointed to a dominant folding motif that is represented in the low free-energy structures. The local folding motifs were preserved in several fragment ions produced by electron transfer dissociation. Gradient optimizations of $(GLGGK +2H)^{+\bullet}$ cation-radicals revealed local energy minima corresponding to distonic zwitterionic structures as well as aminoketyl radicals. Both these structural types can isomerize to low-energy tautomers that are protonated at the radical-containing amide group forming a new type of intermediates, $-C^{\bullet}O^{-}NH_2^{+}-$ and $-C^{\bullet}(OH)NH_2^{+}-$, respectively. Extensive mapping with B3LYP, M06-2X, and MP2(frozen core) calculations of the potential energy surface of the ground doublet electronic state of $(GLGGK +2H)^{+\bullet}$ provided transition state and dissociation energies for backbone cleavages of the N—C_α and amide C—N bonds leading to ion-molecule complexes. The complexes can undergo facile prototropic migrations that are catalyzed by the Lys ammonium group and isomerize enolimine ***c***-type fragments to the more stable amide tautomers. In contrast,

inter-fragment hydrogen atom migrations in the complexes were found to have relatively high transition energies and did not compete with fragment separation. The extensive analysis of the intermediate and transition state energies led to the conclusion that the observed dissociations cannot proceed competitively on the same potential energy surface. The reactive intermediates for the dissociations originate from distinct electronic states that are accessed by electron transfer.

2.1 Introduction

Electron attachment to multiply charged peptide ions in the gas phase is a highly exothermic process that can be realized as electron−ion recombination or electron transfer from a charged or neutral donor. Electron−ion recombination forms the basis of electron-capture dissociation (ECD), a mass spectrometric technique that is chiefly performed on Fourier Transform ion cyclotron resonance instruments.[1] Electron transfer in a gas phase anion−cation reaction is typically performed in ion traps using a plethora of gas-phase anions and is referred to as electron transfer dissociation (ETD).[2] Both processes, which are sometimes referred to under a common acronym ExD, result in extensive dissociation of peptide cation-radicals produced by electron attachment to the precursor, closed-shell, peptide ions. ExD have been of keen interest because of practical applications to peptide and protein sequencing,[3] as well as having been the target of fundamental studies of ion structures,[4–8] energetics,[6,9,10] electronic states,[6,11–13] and dissociation mechanisms, as recently reviewed.[14]

To achieve a comprehensive description of ExD of a peptide ion, one has to consider several consecutive and competitive processes that produce the fragment ions in the experimental ETD spectrum. This sequence begins with electron transfer from a molecular anion donor to the multiply charged peptide ion acceptor to form the charge-reduced peptide cation-radical in the

ground or excited electronic states. The formation of electronic states is thought to be affected by the dipolar field surrounding the ion and superimposed on the Coulomb field of the peptide ion charge.[15–17] The ion dipole moment depends on the molecular geometry and charge distribution, which usually are unknown and have to be investigated. The ion geometry is determined by the nature and sequence of amino acid residues, protonation sites, and folding in the gas phase. The last two structural factors are often a priori unknown, contributing to the uncertainties in relating the precursor ion structure with dissociations upon ETD.

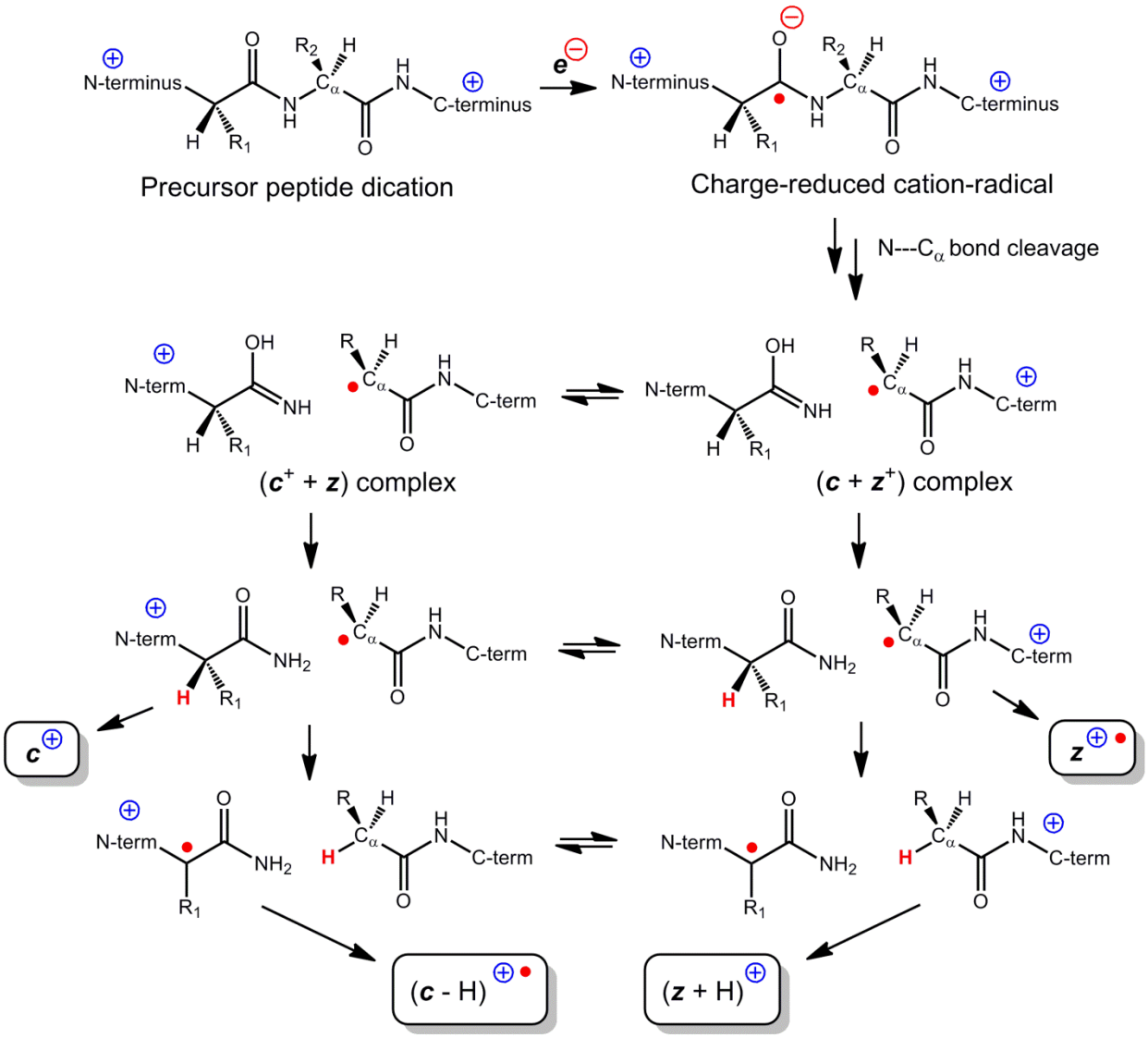

Scheme 3: ETD process whereby c and z backbone ions can be formed with a shift of 1 mass unit from the usual structure.

The peptide cation-radicals formed by electron transfer undergo competitive dissociations of N−H and N−Cα bonds producing first generation fragment ions and neutrals. These can undergo consecutive unimolecular dissociations to form second generation fragments.[18–24] N−Cα bond dissociations produce noncovalent complexes of N-terminal (c) and C-terminal (z) fragments that can react by proton or hydrogen atom transfers before separation. These reactions are generically depicted in Scheme 1.

Selected aspects of ExD have been studied by experiment and theory for a variety of peptide ions. However, comprehensive, "from the cradle to the grave", investigations of ETD, starting with the precursor ion 3D structure and including electron transfer and dissociation energetics, multiple intermediates, and product ion structures have been confined to simple systems, such as dipeptide ions.[6,25] Thus far, no analysis has been attempted to comprehensively investigate the formation upon ETD of first and second generation fragment ions, characterize fragment ion−molecule complexes, and illustrate the energetics and kinetics of the pertinent processes within a larger peptide ion.

Here, we report a comprehensive study of electron attachment to doubly protonated Gly-Leu-Gly-Gly-Lys, $(GLGGK + 2H)^{2+}$. This model peptide was chosen to satisfy several criteria. First, this ion incorporates eleven protons in seven polar groups that are capable of hydrogen bonding to five carbonyl electron donors. This feature was presumed to give the gas-phase precursor dication sufficient flexibility for intramolecular hydrogen bonding to define its gas-phase conformation. Second, this peptide has only two basic amino groups that become the energetically favored protonation sites in the dication. This feature removes the ambiguity of the formation of tautomeric precursor ions. Finally, the $(GLGGK + 2H)^{2+}$ dication has five N−Cα

bonds to be potentially cleaved upon electron transfer, thus allowing one to study several competitive reactions. We report several novel features describing the energies and electronic structure of the peptide cation radicals and transition states for their dissociations that shed light on the complex hydrogen and proton transfer reactions accompanying the backbone cleavages.

2.2. Experimental

2.2.1 Materials and Methods The peptides, Gly-Leu-Gly-Gly-Lys (GLGGK), (Gly-2,2-d2)-Leu-Gly-Gly-Lys (d2-GLGGK), and Ala-Leu-Gly-Gly-Lys (ALGGK), were synthesized on the solid phase (Wang resin, Bachem Americas, Torrance, CA, and Chem-Impex Intl., Wood Dale, IL) using standard f-moc methods,[26,27] and their purity was checked by electrospray mass spectrometry. The fully D-labeled peptide ions, $(GLGGK\text{-}d9 + 2D)^{2+}$, were generated by dissolving the peptide in 1:1 D_2O:CH_3OD (99.5% D) that contained 0.5% CD3COOD to achieve a 7−10 μM concentration and allowing the solution to stand for several hours, typically overnight, in a tightly capped vial. The peptide solution was infused with a syringe pump into an open electrospray source consisting of a pulled fused silica capillary as the ESI needle that was positioned 2 mm from the orifice of the source transfer capillary.[28] Simultaneously with electrospraying the D2O/CH3OD peptide solution, a stream of nitrogen that was saturated with D_2O vapor was blown over the orifice and tip of the ESI needle from a 20-mm o.d. Pyrex tubing that was brought within 2 mm of the ESI tip. Electron transfer dissociation (ETD) mass spectra were measured on a Thermo Fisher linear quadrupole ion trap (LTQ-ETD) instrument equipped with an auxiliary chemical ionization ion source for the generation of fluoranthene anions as electron donors. Doubly charged peptide ions were produced from 1 to 5 μM solutions in 50:50:1 methanol−water-acetic acid in an open electrospray ion source. The ions were mass selected, stored in the linear ion trap and reacted with mass selected fluoranthene anions for 25, 50, 75,

100, 150, 200, and 300 ms. High resolution ETD mass spectra were measured on a Thermo Fisher Orbitrap Velos ETD mass spectrometer with the resolving power set to 60,000 and on a Thermo Electron Fisher Orbitrap Elite ETD mass spectrometer at 120,000 resolution, using 200 ms ion−ion reaction times in both series of measurements. Ion mobility measurements of $(GLGGK + 2H)^{2+}$ and its ETD fragments were measured using a modified Waters Synapt G2 HDMS (Waters Co., Manchester, U.K.).[29,30] For ETD experiments, nitrogen gas seeded with azulene vapor was passed through a needle positioned behind the first source orifice.[31] A potential was applied to the needle for 100 ms to generate a glow discharge. The resulting azulene radical anions were selected with the quadrupole and accumulated in the trap cell. Then, $(GLGGK + 2H)^{2+}$ ions generated from nanoelectrospray ionization from a pulled borosilicate glass capillary were selected by the quadrupole and entered the trap cell to react with the stored anions for 1000 ms. Absolute mobilities (K) were measured using a 25.2 cm radio frequency confining drift cell containing 2.0 Torr of helium gas,[32] which replaced the traveling-wave ion mobility cell. Inside this cell, ions experience a constant time-average electric field; thus K can be determined directly from the measured drift times, pressure, and temperature. Most K values were determined from the slopes of a drift time versus reciprocal drift voltage plots ($r^2 > 0.998$) containing measurements at ∼10 drift voltages ranging from 104−353 V. Some values for low-intensity ions were determined by using a single drift time measurement and an estimate of the residence time of the ion between the exit of the ion mobility cell and the entrance of the mass analyzer (t_0). Collision cross sections were determined from K and the Mason−Schamp equation.[33]

2.2.2. **Calculations** Conformational analysis was carried out using the ConformSearch software described previously.[34] In this case, nine candidate structures were generated **1a**$^{2+}$-**1i**$^{2+}$.

Single-point energies for cation-radicals were obtained by UB3LYP, UM06-2X, and UMP2(frozen core) calculations with the 6-311++G(2d,p) basis set. The B3LYP and spin-projected MP2 energies were averaged (B3-PMP2) to cancel small errors inherent to both approximations.[35,36] This empirical procedure has been shown to provide relative energies of improved accuracy for peptide ions and radicals.[6,34] Excited-state energies were calculated using time-dependent DFT theory[37] and the B3LYP and M06-2X hybrid functionals with the 6-311++G(2d,p) basis set. All electronic structure calculations were carried out with the Gaussian 09 suite of programs.[55] Atomic charge and spin densities were calculated with the natural population analysis (NPA) method.[38]

Unimolecular rate constants were calculated for reactions occurring on the calculated B3-PMP2 and M06-2X potential energy surfaces that included zero-point vibrational energy corrections, using the Rice−Ramsperger−Kassel−Marcus (RRKM) theory[39] and the program of Zhu and Hase[56] that had been modified to deal with larger molecular systems with up to 1000 atoms, and recompiled to run under Windows XP[40] and Windows 7. The RRKM rate constants were obtained by direct count of quantum states at internal energies that were increased in 2 kJ mol^{-1} steps from the transition state up to 400 kJ mol^{-1} above the reactant.

Collision cross sections were calculated using the Mobcal program of the Jarrolds research group at Indiana University.[41,42] The impact parameters for the trajectory method used those from the work of Campuzano Et al.[43]

2.3. Results

2.3.1. Electron Transfer Dissociations The doubly charged $(GLGGK + 2H)^{2+}$ ions and their isotopologues underwent ion−ion reactions with fluoranthene anions that showed pseudo-first-order kinetics with apparent rate constants of 7.6−9.4 s^{-1}. Electron transfer resulted in a nearly

complete dissociation, so no charge-reduced $(GLGGK + 2H)^{+\bullet}$ ions were detected in the spectra. Most of the fragment ion relative intensities showed flat dependence on the ion−ion interaction time over 50−300ms, indicating that the dissociations were sufficiently fast to be complete at our shortest observation time. The fragment ion relative intensities are summarized in Table 1.

	GLGGK		G(2,2-d_2)LGGK		d_{11}-GLGGK	
Ion	m/z	Rel. Int.	m/z	Rel. Int.	m/z	Rel. Int.
M+(H,D)	431.2612	24(0.9)	433	24(0.5)	441	9.1(0.4)
M+2(H,D)-N(H,D)$_3$ (***z*****$_5$**)	415.2425	8.7(0.4)	417	8.2(0.3)	423	10(0.7)
z**$_5$**-C_3H_7	372.1877	4.9(0.1)	374	4.3(0.1)	380	4.5(0.3)
z**$_5$**-C_4H_8	359.1799	14(0.4)	361	13(0.2)	367	14(0.9)
z**$_4$**	358.2211	1.2(0.02)	358	1.1(0.02)	365	1.2(0.1)
z**$_4$**-C_3H_7	315.1663	3.7(0.1)	315	3.5(0.1)	322	3.5(0.2)
c**$_4$**	302.1823	11(0.2)	302	11(0.4)	310	11(0.8)
c**$_4$**-H	301.1745	0.1(0.01)	301	0.5(0.01)		
y**$_3$**	261.1557	1.7(1.2)	261	6.2(2.1)	269	10.5(4.2)
z**$_3$**+H	246.1448	0.2(0.01)			252	0.3(0.3)
z**$_3$**	245.1730	10(1)	245	11(1.4)	251	11(2.3)
c**$_3$**	245.1608	1	247	0.8(0.03)	252	1(0.1)
z**$_2$**+H	189.1233	1(0.03)	189	0.9(0.01)	194	1.2(0.1)
z**$_2$**	188.1155	2.1(0.08)	188	2.0(0.04)	193	2.1(0.2)
c**$_2$**	188.1393	<0.1	190	0.2		
y**$_1$**	147.1128	2.2(0.2)	147	2.3	153	1.6(0.2)
y**$_1$**-H	146.1050	1.2(0.1)	146	1.5	152	1.3(0.2)
z**$_1$**+H	132.1019	0.6				
z**$_1$**	131.0941	0.09				
Total Fragments		88(2)		80(1)		83(1)

Table 1: Ions identified, masses and intensities relative to the sum of all ETD fragment ions. Mean intensities and standard deviations from measurements at 50, 100, 200 and 300ms ion-ion reaction times. z_3 and y_3 ion intensities were time dependent. Ion intensities for z_1 and z_1+H were extrapolated from first-order decay kinetics.

A large fraction of ETD resulted in deprotonation or H atom loss, forming the m/z 431 ions from $(GLGGK + 2H)^{2+}$. This can be due to a peptide proton transfer to fluoranthene anion in an acid−base reaction, or electron transfer followed by hydrogen atom loss from the charge-reduced peptide cation-radical. These processes give rise to isobaric peptide ion products and cannot be readily distinguished in the spectra. The ETD mass spectrum of the $(d9\text{-}GLGGK + 2D)^{2+}$ ion, in

which all OH and NH protons were exchanged for deuterium, showed a markedly decreased m/z 441 $(d9\text{-}GLGGK + D)^+$ ion intensity of 9.1% compared to 24% $(GLGGK + H)^+$ formed from $(GLGGK + 2H)^{2+}$. This decrease can be attributed to isotope effects on both proton transfer and loss of H from the ammonium groups in the charge-reduced ion. In particular, loss of H from ammonium radicals has been reported to display large isotope effects.[44–48]

The majority (~60%) of ion fragments by ETD of $(GLGGK+ 2H)^{2+}$ were formed by N−Cα bond dissociations. Cleavage of the N−Cα bond at the N-terminal Gly_1 comprised 27% of fragments formed by loss of ammonia ($\boldsymbol{z_5}^{\bullet}$ fragment ion) and consecutive leucine side-chain dissociations by loss of C_3H_7 and C_4H_8 from the $\boldsymbol{z_5}^{\bullet}$ ions. The assignment of the loss of ammonia ions as $\boldsymbol{z_5}^{\bullet}$ fragments was based on previous studies that used specific ^{15}N labeling in homologous Lys C-terminated ions.

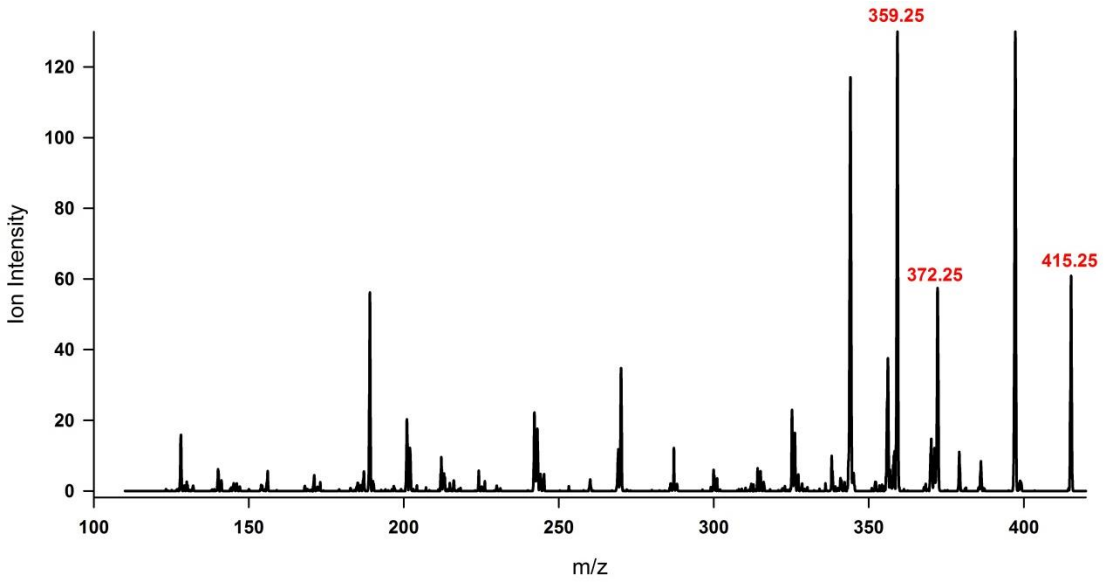

Figure 11: ESI-ETD-CID MS3 spectrum of z5 ion generated from ETD of the doubly charged GLGGK precursor. Peaks at m/z 372 and 359 represent loss of radical C_3H_7 and molecule C_4H_8.

[49] It was also supported by the CID-MS^3 mass spectrum of the $\boldsymbol{z_5}^{\bullet}$ ion (Figure 1) which showed radical-driven dissociations in the Leu and Lys residues, such as loss of C_3H_7 (43.0546 Da), C_4H_8

(56.0625 Da), C_3H_9N (59.0733 Da), and C_4H_9N (71.0734 Da) neutral radicals or molecules, which are typical of peptide ***z***-type cation-radicals.[21–23]Cleavage of the Leu_2 N−Cα bond gave rise to 4.9% of combined $\boldsymbol{z_4}^{\bullet}$ ions and their secondary ($\boldsymbol{z_4}^{\bullet}$ − C3H7) products. Dissociation at Gly_3 produced 11% of combined $\boldsymbol{z_3}^{\bullet}$, $\boldsymbol{z_3}^{\bullet}$ + H, and $\boldsymbol{c_2}$ ions. Cleavage at Gly_4 was less effective, producing 3.5% of combined $\boldsymbol{z_2}^{\bullet}$, $\boldsymbol{z_2}^{\bullet}$ + H, and $\boldsymbol{c_3}$ ions. Cleavage at Lys_5 formed 12% of combined $\boldsymbol{c_4}$, $\boldsymbol{c_4}$ − H, $\boldsymbol{z_1}^{\bullet}$, and $\boldsymbol{z_1}^{\bullet}$ + H ions. The N−Cα bond dissociation at Lys_5 involved proton transfer favoring the formation of the $\boldsymbol{c_4}$ fragment ion over the complementary $\boldsymbol{z_1}^{\bullet}$ ion. Note that the $\boldsymbol{z_3}^{\bullet}$ and $\boldsymbol{c_3}$ fragment ions at m/z 245 as well as the $\boldsymbol{z_2}^{\bullet}$ and $\boldsymbol{c_2}$ fragment ions at m/z 188 are nominally isobaric and overlap in the low-resolution ETD mass spectra of $(GLGGK + 2H)^{2+}$. The $\boldsymbol{z_3}^{\bullet}$ /$\boldsymbol{c_3}$ overlap was unambiguously resolved in high resolution ETD mass spectra, which showed a 10:1 ratio of $\boldsymbol{z_3}^{\bullet}$ (m/z 245.1364) and $\boldsymbol{c_3}$ (m/z 245.1603), favoring the $\boldsymbol{z_3}^{\bullet}$ ion. The $\boldsymbol{z_2}^{\bullet}$ and $\boldsymbol{c_2}$ ions were of very low relative intensity in the high-resolution ETD mass spectra. These fragments were distinguished using mass shifts in the ETD mass spectra of isotopically labeled derivatives. For example, in the ETD mass spectra of the $G(d_2)LGGK$ ion, the $\boldsymbol{z_2}^{\bullet}$ and $\boldsymbol{z_3}^{\bullet}$ ions did not contain the heavy Gly_1 residue and their m/z and were not shifted (Table 1).

The ETD mass spectrum of the completely D-exchanged $(d_9\text{-}GLGGK + 2D)^{2+}$ ion showed $\boldsymbol{z_5}^{\bullet}$, $\boldsymbol{z_4}^{\bullet}$, $\boldsymbol{z_3}^{\bullet}$, $\boldsymbol{z_2}^{\bullet}$, and $\boldsymbol{c_4}$ backbone fragments with mass shifts that were appropriate for the expected number of exchangeable protons in these ions (Table1). The respective fragment relative intensities, combined with those of their secondary dissociation products, were 28, 4.8, 12, 3.3, and 11%. These figures were very similar to those from ETD of $(GLGGK + 2H)^{2+}$ and $(G(d_2)LGGK + 2H)^{2+}$ ions and indicated very small isotope effects on the backbone dissociations.

The time dependence of the fragment ion relative intensities was monitored in the range 25−300 ms, as shown for $(d9\text{-GLGGK} + 2D)^{2+}$ (Figure 2).

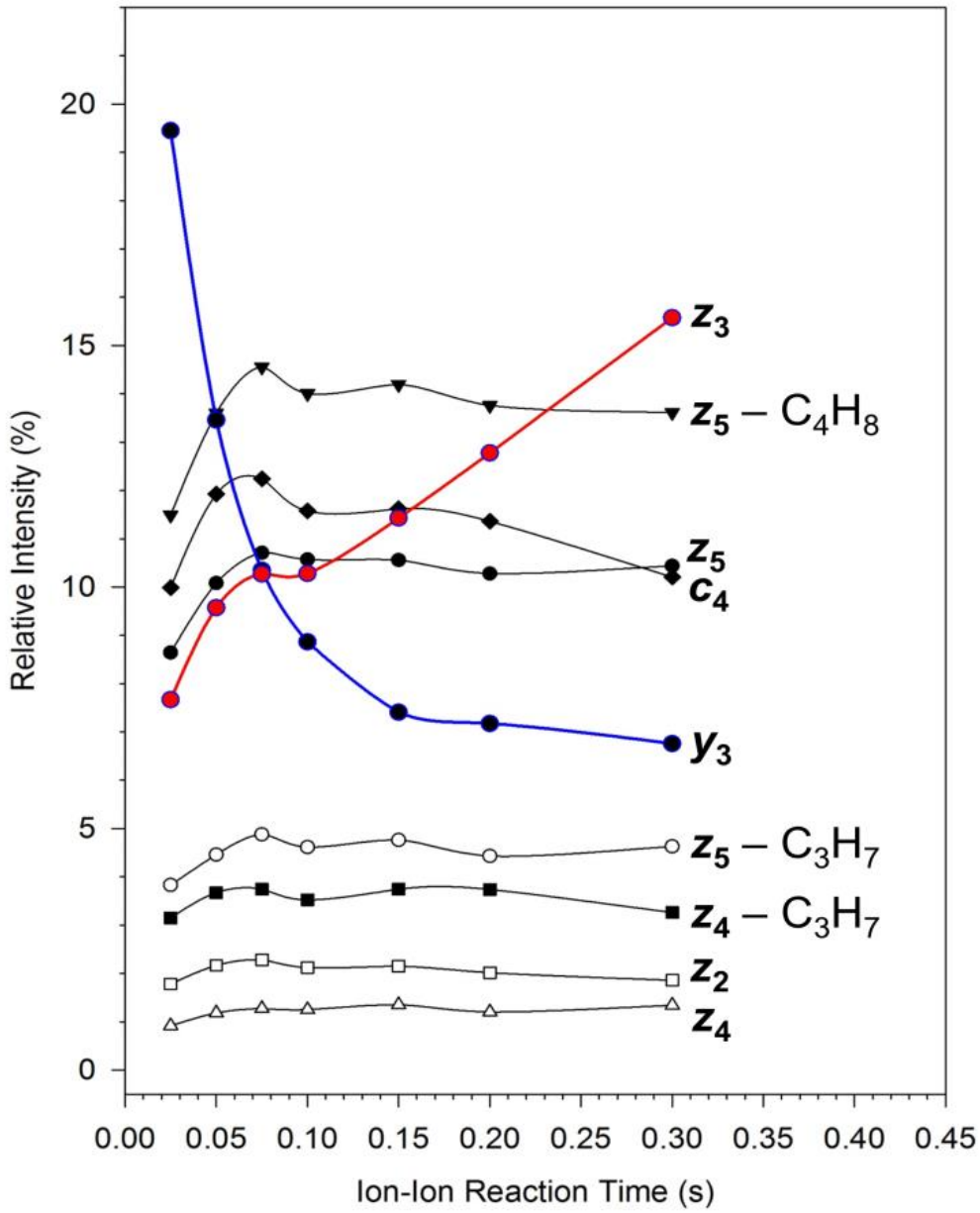

Figure 12: Time dependent Relative Intensities of d_{11}-GLGGK derived ETD sequence fragments.

Most fragment ions showed a flat time profile after 50 ms, indicating that the rate constants for their formation were greater than 100 s^{-1}. In contrast, the $z_3^{\bullet}$ and y_3 ions showed time-dependent intensity profiles. The $z_3^{\bullet}$ ion relative intensity increased with time with an apparent rate constant

estimated at 12−15 s^{-1}. This is much lower than the rate constants estimated for the other backbone cleavages, indicating that the dissociation leading to the $\boldsymbol{z_3^{\bullet}}$ ion did not proceed competitively from the same pool of charge-reduced precursor ions. The relative intensity of the $\boldsymbol{y_3}$ ions exponentially decreased at longer ion−ion reaction times. This is likely due to the depletion by electron transfer of the precursor dications by the pseudo-first order reaction with the fluoranthene anion.[8] The $\boldsymbol{y_3}$ ions are readily formed by collisional excitation of precursor dications.

In summary, the GLGGK ions demonstrated multiple backbone cleavages, side-chain losses, and proton and hydrogen atom transfers in their ETD mass spectra, which are reactions that are typical of the majority of charge-reduced peptide ions.[14]

2.3.2. Precursor and Fragment Ion Structures A conformational search of $(GLGGK + 2H)^{2+}$ ion structures identified several low-energy conformers. The lowest-energy conformers $\mathbf{1a^{2+}}$ − $\mathbf{1i^{2+}}$ are shown in Figure 2, and their energies are summarized in Table 2. Somewhat unexpectedly for such a small peptide ion, the calculated equilibrium population of conformers was dominated by conformers $\mathbf{1a^{2+}}$ and $\mathbf{1b^{2+}}$ (Figure 3). These showed nearly identical hydrogen bonding patterns where the charged lysine ammonium group formed hydrogen bonds to the Gly_3 and Gly_4 amide carbonyls, and the charged N-terminal ammonium group formed a hydrogen bond to the carboxyl group. This spatial arrangement allowed for efficient internal solvation of both charged groups while balancing the attractive ion-dipole interactions with Coulomb repulsion of the charged groups. Structures $\mathbf{1a^{2+}}$ and $\mathbf{1b^{2+}}$ showed two other hydrogen bonds between the neutral groups, one involving the leucine amide carbonyl and the Gly_4 amide proton, and the other involving the Gly_1 amide carbonyl and the Gly_3 amide proton. Conformer $\mathbf{1b^{2+}}$ differs from $\mathbf{1a^{2+}}$ in the rotation of the Leu side-chain isopropyl group.

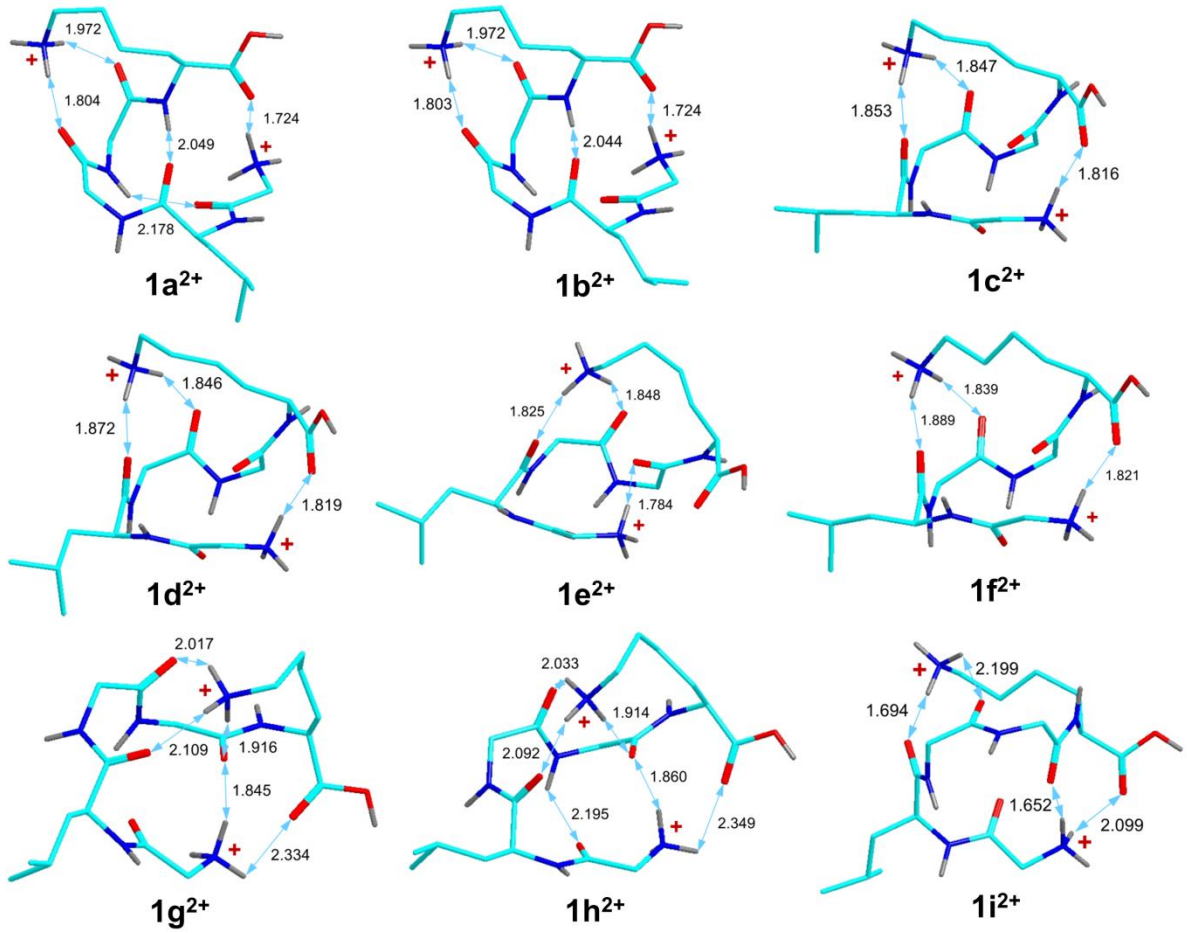

Figure 13: M06-2X/6-31+G(d,p) derived low energy ion conformers for doubly charged GLGGK.

	Relative Energy (kJ/mol)			Dipole Moment (D)	
Ion	B3LYP	M06-2X	MP2	B3LYP	M06-2X
1a^{2+}	0	0	0	5.3	5.7
1b^{2+}	4.8(4.6)	3.3(1.4)	4.4(4.2)	5.0	5.6
1c^{2+}	17(8.4)	17(11)	23(15)	5.0	3.9
1d^{2+}	16(12)	20(18)	24(23)	4.3	3.2
1e^{2+}	18(16)	20(18)	21(19)	4.2	4.4
1f^{2+}	25(25)	20(20)	21(24)	4.7	4.1
1g^{2+}	27(28)	19(20)	23(24)	6.3	5.6
1h^{2+}	28(31)	17(20)	21(24)	7.3	6.8
1i^{2+}	15(12)	25(19)	20(18)	3.9	4.0

Table 2: Relative Energies and Dipole Moments for doubly charged GLGGK conformer structures. Numbers in parantheses represent free energies corrected by the appropriate entropy, enthalpy and hindered rotor corrections at 298K.

Other conformers were calculated to have notably higher enthalpies and 298 K free energies than $\mathbf{1a}^{2+}$ and $\mathbf{1b}^{2+}$. The calculated free energies indicated that a 298 K equilibrium should be dominated by $\mathbf{1a}^{2+}$ (64−84%) and $\mathbf{1b}^{2+}$ (36−16%) with small populations of $\mathbf{1c}^{2+}$ (0.2−2.8%) and $\mathbf{1d}^{2+}$ (0.01−0.7%) being present. The population ranges reflect differences in the relative free energies calculated by B3LYP, M06-2X, and MP2 (Table2). The entropy effect can increase the populations of $\mathbf{1c}^{2+}$ and $\mathbf{1d}^{2+}$ if the ions were sampled at higher temperatures or excited by collisional activation. Higher energy structures $\mathbf{1e}^{2+}$−$\mathbf{1i}^{2+}$ listed in Table 2 and several others were calculated to have negligible populations at equilibrium. Fully optimized structures were also obtained for ETD fragment cation-radicals $\boldsymbol{z_1}^{\bullet}$, $\boldsymbol{z_2}^{\bullet}$, $\boldsymbol{z_3}^{\bullet}$, and $\boldsymbol{z_4}^{\bullet}$, and even-electron ions $\boldsymbol{z_4}^{\bullet}$ + H, and $\boldsymbol{c_4}$.

2.3.3. Collisional Cross Sections The optimized geometries and Mulliken atomic charges were used to calculate collisional cross sections (Ω) for the precursor ion conformers and fragment ions and compare them to the experimental data from ion mobility measurements. The experimental Ω of $(GLGGK +2H)^{2+}$ was measured as 136 ± 3 $Å^2$. The experimental and calculated Ω are summarized in Table 3.[41,50] It may be noted that calculations that used atomic charge densities from Mulliken and natural population analysis[38] gave collisional cross sections within 0.3% of each other and were considered equivalent. The data showed a narrow range of theoretical collisional cross sections, Ω = 132−140 $Å^2$ for $\mathbf{1a}^{2+}$, $\mathbf{1b}^{2+}$, $\mathbf{1c}^{2+}$, $\mathbf{1e}^{2+}$, and $\mathbf{1i}^{2+}$. In particular, the Ω of these conformers that were based on M06-2X geometries and charge densities were nearly identical (Table 3).

	Collision Cross Sections (Å^2)				
	B3LYP		M06-2X		
Structure	PA	TM	PA	TM	Experiment±Std. Deviation
1a^{2+}	138	140	135	136	136±2.5
1b^{2+}	137	139	134	136	
1c^{2+}	135	137	132	133	
1e^{2+}	136	138	134	134	
1i^{2+}	135	137	132	135	
c_4^+	109	107	107	104	103±0.5
$z_4^{+\bullet}$	125	122	119	117	121±0.1
c_3^+	99	94	98	92	89
$z_3^{+\bullet}$	94	89	93	88	89±0.9
y_1^+	72	66	71	65	66±0.5

Table 3: Calculated and Experimental Collision Cross Sections for selected ions.

This result followed from the very similar ionic hydrogen bonding patterns in the low-energy conformers where the N-terminal and lysine side-chain ammonium groups adopted an antiparallel orientation that ensured energetically most favorable internal solvation of both charged groups. Although the experimental and theoretical collisional cross sections did not allow us to assign a particular conformer to the gas−phase dications, they clearly pointed to the group of conformers with the hydrogen bonding pattern represented in all lowest free-energy structures. Another feature of ion structures **1a**$^{2+}$−**1i**$^{2+}$ was that they had a narrow range of dipole moments, μ = 3.9−5.3 D (Table 2), again consistent with the very similar alignments of the charged and polar groups in these ions.

Collisional cross sections were also measured and calculated for ETD fragment ions c_4, $z_4^{\bullet}$, $z_3^{\bullet}$, and y_1 (Table 3). The calculated cross sections showed a trend depending on the optimized geometry and method used to convert the geometry to the Ω values. The closest agreement was obtained for data from trajectory method calculations that were based on M06-2X optimized structures, which showed a 4.1% maximum and 2.9% root-mean square deviation from the experimental cross sections. The B3LYP optimized structures also gave a close

agreement with experiment (4.8% maximum, 2.9% rmsd) when treated with the trajectory method. These results showed that the calculated structures were representative of the fragment ion geometries even though these were obtained without an exhaustive conformational search. The close match of the calculated and experimental structures indicated that the fragments preserved the local folding motifs from the precursor ions.[34] This gave some confidence that also the calculated fragment ion energies could be used for realistic approximations of the dissociation energetics.

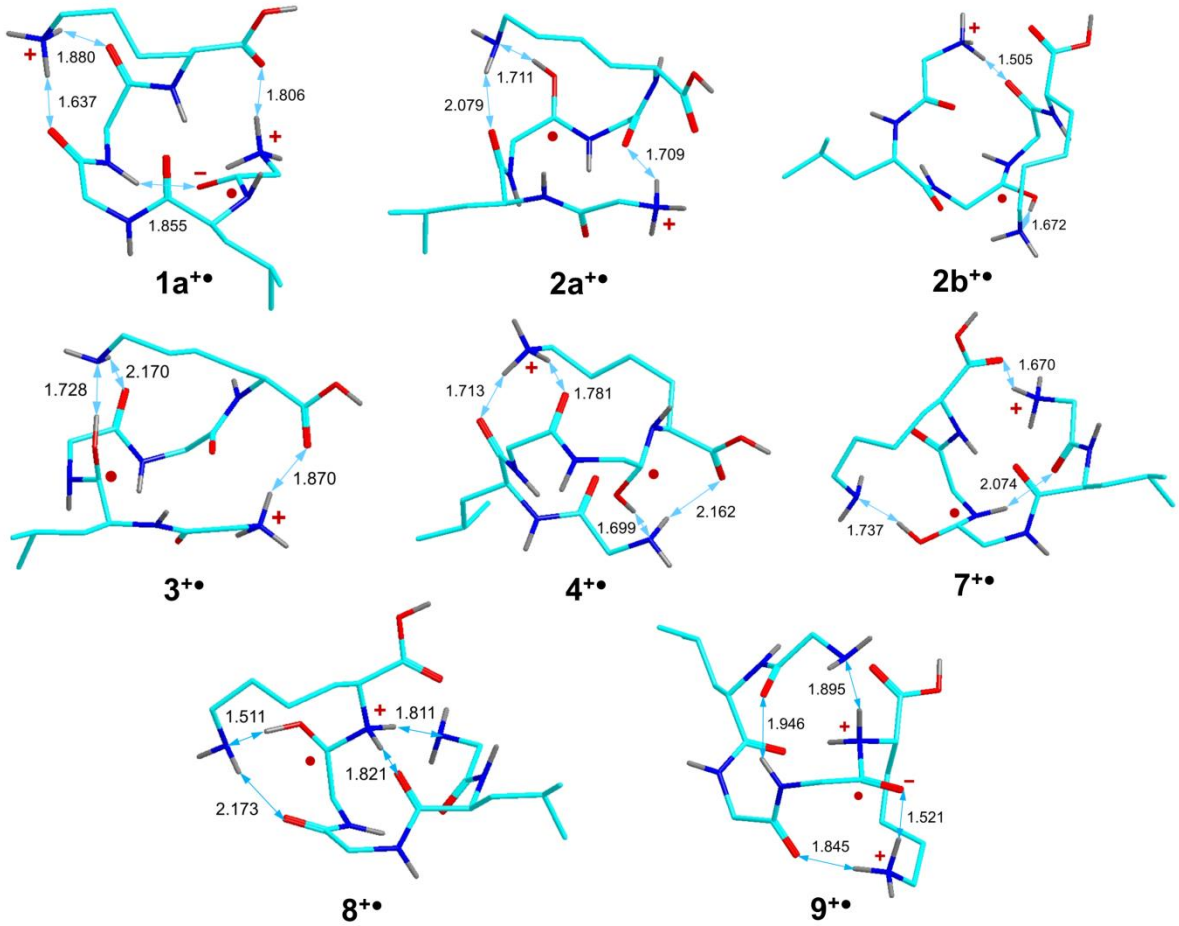

Figure 14: M06-2X/6-31+G(d,p) optimized structures for GLGGK cation radicals from the doubly charged precursor ions.

2.3.4. Cation-Radical Structures and Energies The geometries of the low-energy dication conformers $\mathbf{1a}^{2+}$, $\mathbf{1c}^{2+}$, and $\mathbf{1i}^{2+}$ were used as initial structures in a search for cation-radicals

formed by electron attachment. Several local energy minima were found for cation-radicals as summarized in Figure 3. The relationship of the cation-radical to its precursor dication is denoted by an arrow, as in $\mathbf{1a}^{2+} \rightarrow \mathbf{1a}^{+\bullet}$.

The pertinent local energy minimum obtained by both B3LYP and M06-2X corresponded to a zwitterionic structure ($\mathbf{1a}^{+\bullet}$, Figure 4) consisting of a Gly_1 amide anion-radical and the positively charged N-terminal and Lys ammonium groups. Analogous zwitterions have been reported for other peptide cation-radicals[51] and appear to represent a rather common structural type produced by electron attachment to peptide ions.[14]

Electron attachment to dications $\mathbf{1c}^{2+}$ and $\mathbf{1i}^{2+}$ was also studied. These were selected because their H-bonding patterns slightly differed from that in $\mathbf{1a}^{2+}$, a feature that could affect the electronic states accessed by electron transfer. Electron attachment to $\mathbf{1c}^{2+}$ followed by gradient optimization resulted in a spontaneous migration of a Lys ammonium proton to the Gly_3 amide, forming the Gly_3 aminoketyl radical $\mathbf{2a}^{+\bullet}$ (Figure3) which was at a slightly higher energy than $\mathbf{1a}^{+\bullet}$. This process could be altered by artificially puckering the Leu amide carbonyl in $\mathbf{1c}^{2+}$, in which case electron attachment and geometry relaxation resulted in Lys proton migration to the Leu amide group and formation of the Leu aminoketyl radical $\mathbf{3}^{+\bullet}$. The latter cation-radical was 19 kJ mol^{-1} less stable than $\mathbf{1a}^{+\bullet}$. Electron attachment to $\mathbf{1i}^{2+}$, followed by geometry relaxation, formed the Gly_4 aminoketyl radical $\mathbf{4}^{+\bullet}$, which was 10 kJ mol^{-1} more stable than $\mathbf{1a}^{+\bullet}$. An attempt to generate a Leu amide radical from $\mathbf{1i}^{2+}$ resulted in a collapse to another conformer of the Gly_3 aminoketyl radical ($\mathbf{2b}^{+\bullet}$).

2.3.5. Proton Migrations in Cation-Radicals Cation-radical $\mathbf{1a}^{+\bullet}$ that was spontaneously produced as a local energy minimum upon gradient optimization was further investigated regarding tautomer-forming proton migrations. Migration of a proton from the neutral Gly_3

amide group onto the negatively charged Gly_1 amide oxygen in $\mathbf{1a}^{+\bullet}$ formed cation-radical $\mathbf{5}^{+\bullet}$ (Scheme 2). This was a zwitterionic aminoketyl-imidate tautomer in which the spin density was localized in the neutral Gly_1 aminoketyl group, whereas the deprotonated Gly_3 amide group carried a negative charge. Tautomer $\mathbf{5}^{+\bullet}$ was 18 kJ mol^{-1} less stable than $\mathbf{1a}^{+\bullet}$ into which it could isomerize by a reverse proton migration after crossing a miniscule energy barrier in the transition state (TS1, E_{TS1} = 2 kJ mol^{-1} relative to $\mathbf{5}^{+\bullet}$).

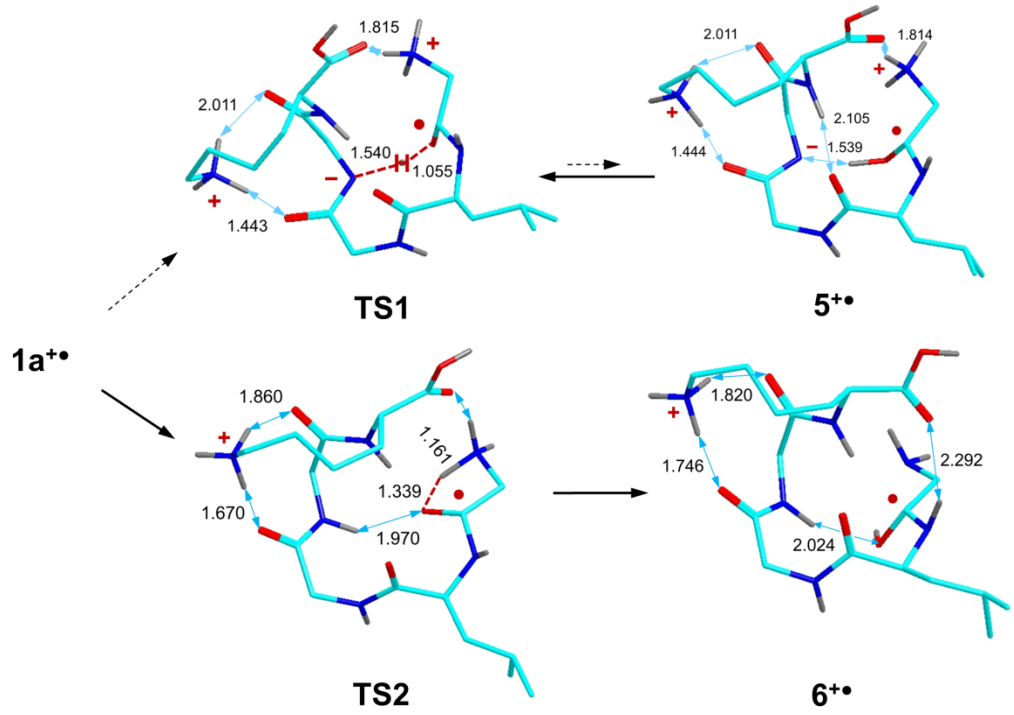

Scheme 4: Proton migrations from structure $1a^{+\bullet}$ leading through transition states to cation radical $5^{+\bullet}$ and $6^{+\bullet}$.

Migration of a proton from the charged N-terminal ammonium group onto the Gly_1 amide oxygen in $\mathbf{1a}^{+\bullet}$ (Scheme 2) formed cation-radical $\mathbf{6}^{+\bullet}$ (−38 kJ mol^{-1} relative to $\mathbf{1a}^{+\bullet}$). The exothermic $\mathbf{1a}^{+\bullet} \rightarrow \mathbf{6}^{+\bullet}$ proton migration required overcoming a very small potential energy barrier in the pertinent transition state (TS2) that vanished upon inclusion of zero-point vibrational energies to give E(TS2) = −2.4 kJ mol^{-1} relative to $\mathbf{1a}^{+\bullet}$. Hence, $\mathbf{1a}^{+\bullet}$ can be

considered to be dynamically unstable with respect to this exothermic isomerization. Dynamic instability has been reported for other zwitterionic peptide cation radicals.[14,51]

Ion/Reaction	Relative Energy(kJ/mol) B3LYP	M06-2X	PMP2
1a$^{+\bullet}$	0	0	0
2a$^{+\bullet}$	3	18	17
2b$^{+\bullet}$	−4	15	10
3$^{+\bullet}$	14	19	26
4$^{+\bullet}$	−18	−2	−2
5$^{+\bullet}$	29	18	23
6$^{+\bullet}$	−32	−38	−27
1a$^{+\bullet}$→ **TS1**	23	20	17
1a$^{+\bullet}$ → **TS2**	−2	−4	−3
7$^{+\bullet}$	11	22	23
8$^{+\bullet}$	12	-[a]	19
9$^{+\bullet}$	−19	−26	−34
Ala-**1a**$^{+\bullet}$→ Ala-**9**$^{+\bullet}$	-4	-7	-15
10$^{+\bullet}$	-[b]	−29	-[b]
1a$^{+\bullet}$ → **TS3**	0.2	11	7
6$^{+\bullet}$ → **TS3**	32	49	34
1a$^{+\bullet}$ → **TS4**	7	21	22
6$^{+\bullet}$ → **TS4**	39	59	49
11$^{+\bullet}$	−138	−115	−129
1a$^{+\bullet}$ →$\mathbf{z_5}^{+\bullet}$+ NH_3	−111	−74	−88
12$^{+\bullet}$	−91	−64	−60
1a$^{+\bullet}$ →$\mathbf{z_4}^{+\bullet}$+ $\boldsymbol{c}_1$(enolimine)	−25	40	46
1a$^{+\bullet}$ →$\mathbf{z_4}^{+\bullet}$+ $\boldsymbol{c}_1$(amide)	−95	−25	−23
1a$^{+\bullet}$ → **TS5**	22	46	40
9$^{+\bullet}$ → **TS5**	40	73	74
13$^{+\bullet}$	−149	−109	−108
1a$^{+\bullet}$ →$\mathbf{z_1}^{+\bullet}$+ $\boldsymbol{c}_4$	−33	41	50

1a$^{+\bullet}$ →$\boldsymbol{z_1}^{\bullet}$+ $\boldsymbol{c_4}^{+}$	−47	31	35
9$^{+\bullet}$ → **TS6**	18	37	41
14$^{+\bullet}$	13	38	28
1a$^{+\bullet}$ → $\boldsymbol{y_1}^{+}$+ $\boldsymbol{b_4}^{\bullet}$	74	152	148
9$^{+\bullet}$ → **11**$^{+\bullet}$	32	64	62
1a$^{+\bullet}$ → **TS7**	57	31	74
7$^{+\bullet}$ → **15**$^{+\bullet}$	−15	0.7	14
2a$^{+\bullet}$ → **TS8**	50	-[c]	59
2a$^{+\bullet}$ → **16**$^{+\bullet}$	45	-[c]	63
2b$^{+\bullet}$ → **TS9**	41	-[c]	62
2b$^{+\bullet}$ → **17**$^{+\bullet}$	−22	6	−2
4$^{+\bullet}$ → **TS10**	24	-[c]	42
4$^{+\bullet}$ → **18**$^{+\bullet}$	20	-[c]	46
4$^{+\bullet}$ → **19**$^{+\bullet}$	0.5	-[c]	17
12$^{+\bullet}$ → **TS11**	37	32	40
20$^{+\bullet}$	−95	−60	−60
21$^{+\bullet}$	−118	−64	−60
21$^{+\bullet}$ → **TS12**	4	6	13
21$^{+\bullet}$ → **22**$^{+\bullet}$	−54	−43	−45
1a$^{+\bullet}$ → **22**$^{+\bullet}$	−179	−105	−113
12$^{+\bullet}$ → **22**$^{+\bullet}$	−82	−42	−47
12$^{+\bullet}$ → **TS13**	76	69	58
12$^{+\bullet}$ → **23**$^{+\bullet}$	−47	−42	−45
1a$^{+\bullet}$ → **24**$^{+\bullet}$	−179	−105	−113
12$^{+\bullet}$ → **24**$^{+\bullet}$	−53	−50	−45
24$^{+\bullet}$ → **TS14**	54	67	49
14$^{+\bullet}$ → **TS16**	58	105	88
14$^{+\bullet}$ → **25**$^{+\bullet}$	−102	−61	−64

Table 4: Relative Energies of Cation Radical Structures and Processes. a) Gradient optimizations collapsed to structure $\mathbf{10}^{+\bullet}$. b) Gradient optimization collapsed to structure $\mathbf{9}^{+\bullet}$. c) calculations did not lead to a transition state.

Electron attachment to the Gly_3 amide in $\mathbf{1a}^{2+}$ did not form an amide anion-radical as a local energy minimum but triggered a spontaneous migration of a Lys ammonium proton, forming aminoketyl radical $\mathbf{7}^{+\bullet}$ (Figure 3) which was another conformer of $\mathbf{2a}^{+\bullet}$. This spontaneous proton migration indicated that the intermediate Gly_3 amide anion radical was a

stronger base than lysine, consistent with the previously proposed concept of superbasicity of amide π* states.[11] Radical **7**$^{+\bullet}$ was 22 kJ mol^{-1} less stable than zwitterion **1a**$^{+\bullet}$ (Table 4).

An interesting result was obtained by attaching an electron to the Gly_4 amide group in **1a**$^{+\bullet}$. The intermediate anion-radical can undergo spontaneous isomerization by Lys proton migration, forming an aminoketyl radical (**8**$^{+\bullet}$, 15 kJ mol^{-1} relative to **1a**$^{+\bullet}$ according to B3-PMP2), which is a conformer of **4**$^{+\bullet}$ (Figure 3). However, a competing exothermic isomerization by migration of an N-terminal ammonium proton to the Gly_4 amide nitrogen in the anion-radical proceeded to form the amide-N-protonated cation-radical **9+•** (−26 kJ mol^{-1} relative to **1a**$^{+\bullet}$). Structure **9**$^{+\bullet}$ (Scheme 3) was unprecedented in both its electronic properties and as a potential intermediate for competitive dissociations of the amide C−N and N−Cα bonds. The Gly_4 amide C•O^{-} and protonated NH2 groups in **9**$^{+\bullet}$ respectively carried a −0.4 and +0.22 charge, attesting to the dipolar character of the CO−NH2 moiety. Cation-radical **9**$^{+\bullet}$ can undergo a further isomerization by migration of a Lys ammonium proton forming ion **10**$^{+\bullet}$ (−29kJ mol^{-1} relative to **1a**$^{+\bullet}$), which is an N-protonated Gly_4 aminoketyl radical. The very similar energies of **9**$^{+\bullet}$ and **10**$^{+\bullet}$ indicated that these structures could readily interconvert by proton migration.

Finally, attempts to attach an electron to the Leu_2 amide group resulted in a collapse to structure 1a+•.

2.3.6. Backbone Dissociations Cation-radicals **1a**$^{+\bullet}$−**10**$^{+\bullet}$ were used as initial structures for studying backbone dissociations and loss of ammonia. These are the main dissociations experimentally observed in ETD of $(GLGGK + 2H)^{2+}$ ions (Table 1). The loss of ammonia was considered to involve the N-terminal ammonium group,[49] and therefore the dissociation was started from structure **1a**$^{+\bullet}$. Upon stretching the N-terminal H3N−C bond and rotating the NH3 group about the CH2-CO bond, the system reached a low-energy transition state (TS3) at 4 kJ

mol^{-1} above **1a**$^{+\bullet}$ (Scheme 4). A complete dissociation to separated $\boldsymbol{z_5}^{\bullet}$ and NH_3 fragments was also substantially exothermic (−74 kJ mol^{-1} relative to **1a**$^{+\bullet}$).

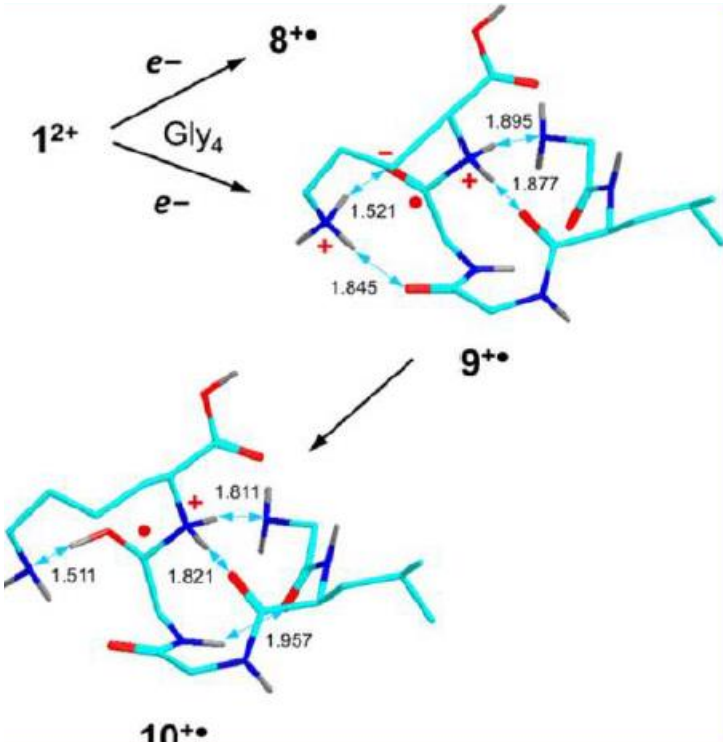

Scheme 5: Charge reduced cation radical 9$^{+\bullet}$ can very readily interconvert to 10$^{+\bullet}$ through a Lys ammonium proton migration.

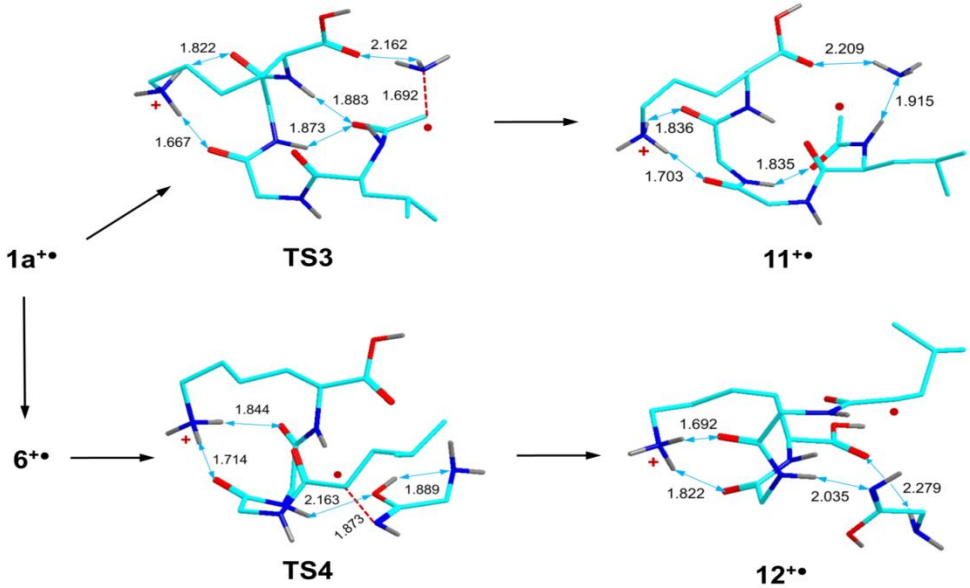

Scheme 6

The loss of ammonia competed with the isomerization of $\mathbf{1a}^{+\bullet}$ to aminoketyl radical $\mathbf{6}^{+\bullet}$ (Scheme 2). The TS energy for the cleavage of the Gly1-Leu amide N−Cα bond in $\mathbf{6}^{+\bullet}$ (TS4) was calculated to be 21 kJ mol^{-1} relative to $\mathbf{1a}^{+\bullet}$, which was slightly higher than the TS3 energy. The dissociation exothermically proceeded to an ion−molecule complex ($\mathbf{12}^{+\bullet}$) consisting of an anti−anti enolimine conformer of the neutral $\boldsymbol{c_1}$ fragment and the $\boldsymbol{z_4}^{\bullet}$ ion. Complex $\mathbf{12}^{+\bullet}$ had a potential energy that was −64 kJ mol^{-1} relative to $\mathbf{1a}^{+\bullet}$. A complete dissociation of $\mathbf{1a}^{+\bullet}$ to the $\boldsymbol{z_4}^{\bullet}$ ion and neutral $\boldsymbol{c_1}$ fragments was 40 kJ mol^{-1} endothermic when forming $\boldsymbol{c_1}$ as an enolimine tautomer, or 25 kJ mol^{-1} exothermic when forming $\boldsymbol{c_1}$ as the more stable glycine amide molecule.

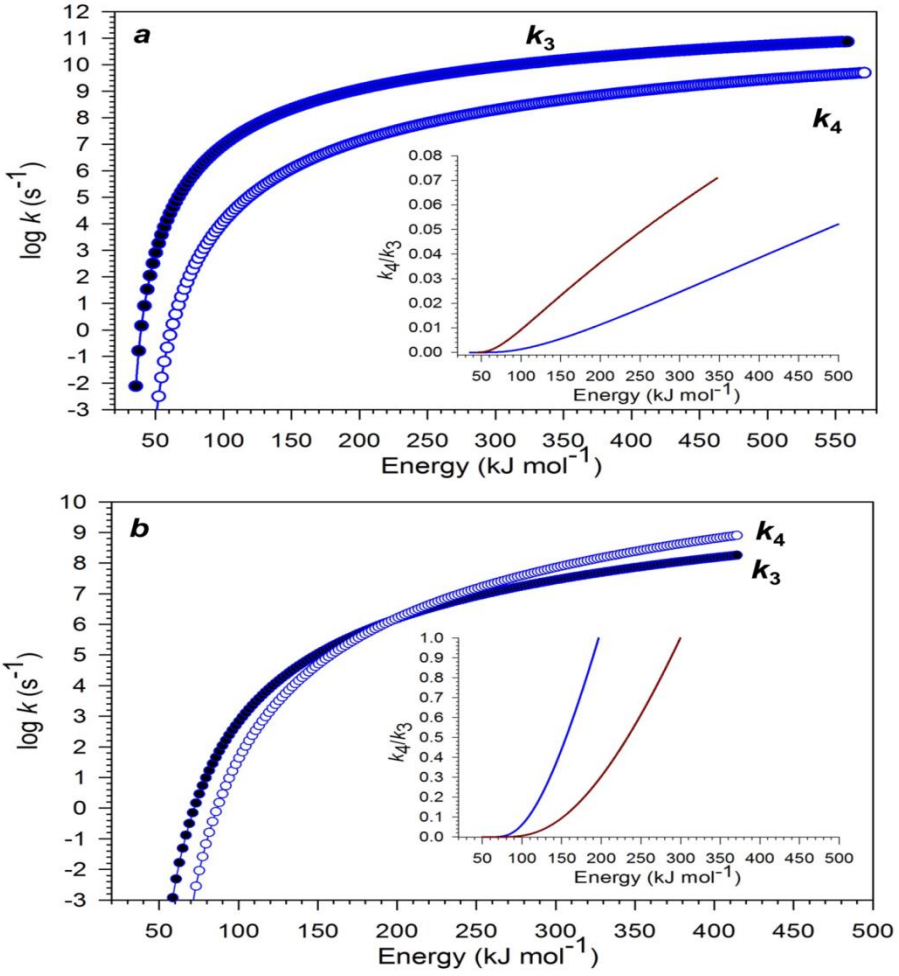

Figure 15: RRKM rate constants for the competing loss of ammonia (k_3, full circles) and N—C_a bond cleavage (k_4, open circles) obtained at (a) combined B3LYP and PMP2 and (b) M06-2X potential energy surfaces. Insets show the k_4/k_3 ratios at calculated TS energies (blue curves) and those that were adjusted by 2 kJ mol^{-1} (brown curves).

The question of the dynamic versus statistical control of $\mathbf{1a}^{+\bullet}$ dissociations was addressed by obtaining the pertinent RRKM unimolecular rate constants for $\mathbf{6}^{+\bullet}$ competitively dissociating via TS3 (k_3) and TS4 (k_4). The rate constants were calculated on the M06-2X and B3-PMP2 potential energy surfaces for a 50−410 kJ mol^{-1} range of internal energies (Figure 5). The rate constants showed a rapid increase with the ion internal energy (E) to reach $k > 100$ s^{-1} at E > 100 kJ mol^{-1}, which was consistent with >99% dissociation of the charge-reduced ions on the experimental time scale (50−300 ms). The experimental branching ratio for these reactions was expressed as a ratio of the pertinent fragment ion relative intensities, $[\boldsymbol{z_4}^{\bullet}]/[M + 2H - NH_3] = 0.18$. These relative intensities were compounded to include the secondary fragments by loss of C_3H_7 and C_4H_8. To compare the RRKM branching ratios with the experimental value, the calculated rate constants have to be convoluted with an internal energy distribution function, P(E), according to the below equation, where $(k_3 + k_4)t \gg 1$.

$$\frac{k_4}{k_3} = \frac{\int_{E_{04}}^{E} P(E)\frac{k_4(E)}{k_3(E)+k_4(E)}\left(1-e^{-(k_3+k_4)t}\right)dE}{\int_{E_{03}}^{E} P(E)\frac{k_3(E)}{k_3(E)+k_4(E)}\left(1-e^{-(k_3+k_4)t}\right)dE}$$

$$\cong \frac{\int_{E_{04}}^{E} P(E)\frac{k_4(E)}{k_3(E)+k_4(E)}dE}{\int_{E_{03}}^{E} P(E)\frac{k_3(E)}{k_3(E)+k_4(E)}dE}$$

Factoring out the time dependence in the above equation was justified by the fact that the experimental $[\boldsymbol{z_4}^{\bullet}]/[M + 2H - NH_3]$ ratio stayed flat over the range of experimental reaction times, indicating $(k_3 + k_4)t \gg 1$. The data indicated that the RRKM rate constants were in qualitative agreement with experiment. The branching ratios for the Gly-Leu N−Cα bond cleavage and loss of ammonia were $k_4/k_3 < 1$ and increased with internal energy when based on

both the M06-2X and B3-PMP2 transition-state energies. However, the B3-PMP2 calculations underestimated the k_4/k_3 ratio by a factor of 3 over the entire range of internal energies (Figure 5a). The M06-2X calculations showed a crossover of the k_4 and k_3 curves at ~190 kJ mol^{-1} (Figure 5b) whereas the experimental branching ratio was matched at a low internal energy of 125 kJ mol^{-1}. The Figure 5a,b data and further analysis indicated that the theoretical branching ratios were very sensitive to the quality of the calculated potential energy surface, in particular the TS energies. For example, adjusting the relative TS energies by 2 kJ mol^{-1} resulted in k_4/k_3 ratios that matched the experimental value over a range of internal energies. One can conclude that the loss of ammonia and Gly-Leu N−Cα bond cleavage can proceed as competitive reactions from populations of reactants with randomized internal energy. However, in spite of this qualitative agreement, the calculated TS energies were not accurate enough to extract the pertinent P(E) function from the equation and address the question of internal energy distribution upon ETD.

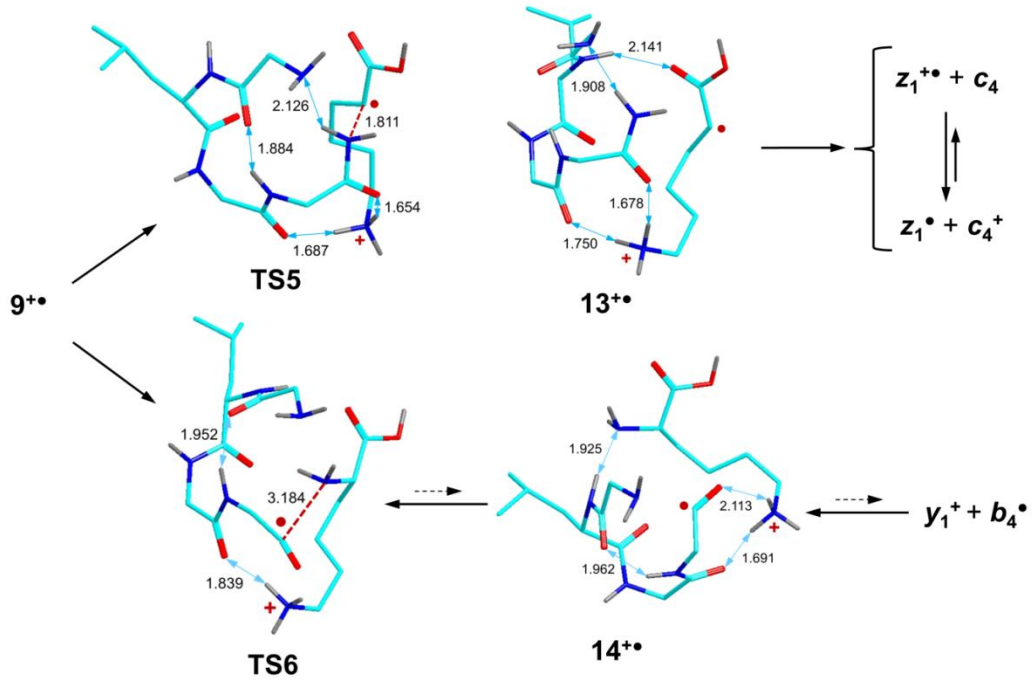

Scheme 7

Structures 9+• and 10+• represented potential reactants for the cleavages of the N−Cα bond between the Gly_4 and Lys residues forming the $\boldsymbol{z_1}^{\cdot}$ and $\boldsymbol{c_4}$ fragments (Scheme 5). The pertinent TS was found (TS5) that connected cation-radical $\mathbf{9}^{+\bullet}$ with complex $\mathbf{13}^{+\bullet}$ consisting of $\boldsymbol{z_1}^{\cdot}$ ion and neutral $\boldsymbol{c_4}$ fragments. The continuing dissociation of complex $\mathbf{13}^{+\bullet}$ depended on the formation of the complementary ($\boldsymbol{z_1}^{\cdot}$ + $\boldsymbol{c_4}$ neutral) or ($\boldsymbol{z_1}^{\cdot}$neutral + $\boldsymbol{c_4}^{+}$) fragments differing in the position of the charging proton. The $\mathbf{1a}^{+\bullet} \rightarrow \boldsymbol{z_5}^{+\bullet}$ + $\boldsymbol{c_4}$ neutral pathway was 41 kJ mol^{-1} endothermic for the formation of the $\boldsymbol{c_4}$ amide tautomer. The complementary $\mathbf{1a}^{+\bullet} \rightarrow \boldsymbol{z_1}^{\cdot}$ + $\boldsymbol{c_4}^{+}$ pathway was 31 kJ mol^{-1} endothermic for the formation of $\boldsymbol{c_4}^{+}$ as an N-terminus protonated GLGG amide. This energy difference reflects the higher proton affinity of GLGG amide (PA = 979 kJ mol−1 at 0 K) than the Lys $\boldsymbol{z_1}^{\cdot}$ (PA = 968 kJ mol^{-1} at 0 K).

A competing pathway was found to involve cleavage of the amide C−N bond in $\mathbf{9}^{+\bullet}$ (Scheme 5). This pathway proceeded through TS6 whose energy was 37 kJ mol^{-1} relative to $\mathbf{9}^{+\bullet}$ to reach another complex ($\mathbf{14}^{+\bullet}$) of the incipient $\boldsymbol{y_1}^{+}$ ion and $\boldsymbol{b_4}$• radical fragments. The lower energy of TS6 relative to TS5 indicated a faster dissociation to $\boldsymbol{y_1}$ and $\boldsymbol{b_4}$ radical fragments. However, complex $\mathbf{14}^{+\bullet}$ was at a 64 kJ mol^{-1} higher energy than $\mathbf{9}^{+\bullet}$, indicating that the $\mathbf{9}^{+\bullet} \rightarrow$ TS6 $\rightarrow \mathbf{14}^{+\bullet}$ reaction was reversible. A further dissociation of $\mathbf{14}^{+\bullet}$ to the $\boldsymbol{y_1}^{+}$ ion and $\boldsymbol{b_4}^{\cdot}$ radical fragments was 106 kJ mol^{-1} endothermic. Nevertheless, the data indicated that the flux through the $\mathbf{9}^{+\bullet} \rightarrow$ TS6 $\rightarrow \mathbf{14}^{+\bullet} \rightarrow \boldsymbol{y_1}^{+}$ + $\boldsymbol{b_4}^{\cdot}$ pathway was hampered by the high energies of the intermediates and products. Note that in the ETD mass spectrum the combined ($\boldsymbol{z_1}^{\cdot}$ + $\boldsymbol{c_4}$)$^{+}$ fragments appear at 3.5-fold greater relative abundance than ($\boldsymbol{y_1}$ + $\boldsymbol{b_4}$)$^{+}$, which is in qualitative agreement with the calculated energetics.

Cation-radical $\mathbf{7}^{+\bullet}$, which is a Gly_3 aminoketyl intermediate, was considered as a reactant for cleavage of the Gly3--Gly4 N−Cα bond, leading to ($\boldsymbol{z_2}^{\cdot}$ + $\boldsymbol{c_3}$)$^{+}$ fragments (Scheme 6). A TS

for this dissociation (TS7) was found at an energy that was 31 kJmol^{-}1 above **1a**$^{+\bullet}$. This dissociation led to complex **15**$^{+\bullet}$ of incipient ($\boldsymbol{z_2}^{\bullet}$ + $\boldsymbol{c_3}$)$^{+}$ fragments that was nearly isoenergetic with **7**$^{+\bullet}$. The intricate proton migrations accompanying the cleavage of the Gly3--Gly4 N−Cα bond were illustrated in a stepwise fashion by intrinsic reaction coordinate analysis in the forward and reverse direction starting from TS7.

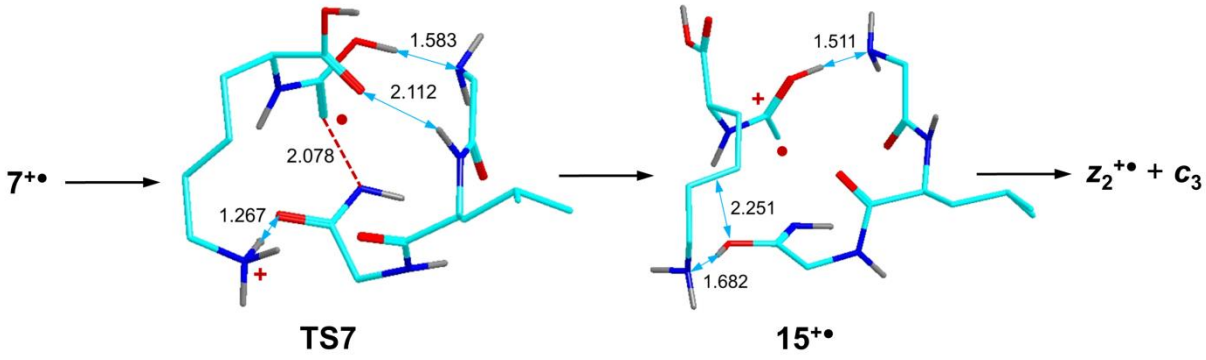

Scheme 8

2.3.7. Enol Dissociation Pathways Aminoketyl radical intermediates can undergo N−Cα bond cleavages on the C- or N-terminal sides of the aminoketyl group.[52,53] Cleavage on the C-terminal side forms the enolimine c and radical z fragments, as described above. Cleavage on the N-terminal side forms a ($\boldsymbol{c}$ −H)$^{\bullet}$ amidyl radical and an enol tautomer of the ($\boldsymbol{z}$ + H)$^{+}$ ion that must exchange a proton or a hydrogen atom to give rise to the $\boldsymbol{c}$ and $\boldsymbol{z}$ fragments.[14,52]

Dissociation of the Gly3-Gly4 enol N−Cα bond in **4**$^{+\bullet}$ proceeded through a low energy TS (TS10, 24−42 kJ mol^{-1} relative to **4**$^{+\bullet}$, Table 4) leading to another complex (**18**$^{+\bullet}$). The latter developed a very tight hydrogen bond between the amidyl oxygen and the Lys ammonium. Complex 18 can undergo a very facile and exothermic reverse formation of the N−Cα bond leading back to **4**$^{+\bullet}$, which occurred spontaneously in geometry optimization with M06-2X. Alternatively, complex **18**$^{+\bullet}$ can be stabilized by a double proton transfer forming a new complex (**19**) of the incipient enolimine $\boldsymbol{c_3}$ ion and a neutral $\boldsymbol{z_2}^{\bullet}$ radical. Note that complex **19**$^{+\bullet}$ is slightly

less stable than $\mathbf{4}^{+\bullet}$ and can revert to it through TS10 rather than continuing along the pathway for the highly endothermic separation of the $\boldsymbol{c_3}$ and $\boldsymbol{z_2}^{\bullet}$ fragments. This is consistent with the inefficient formation of $\boldsymbol{c_3}$ ions in the ETD spectrum (Table 1). Overall, the N−Cα bond dissociations on the enol side of the aminoketyl radicals showed comparable TS energies as did the conventional dissociations on the amide side.[53] However, the intermediate $(\boldsymbol{c} - \mathrm{H})\bullet + (\boldsymbol{z} + \mathrm{H})^{+}$ complexes $\mathbf{16}^{+\bullet}$ and $\mathbf{18}^{+\bullet}$ in the enol pathways containing ***c***-fragment amide enol groups were substantially less stable than the $(\boldsymbol{c} + \boldsymbol{z})^{+\bullet}$ complexes in the standard dissociation pathways.

2.3.8. Proton and Hydrogen Atom Transfer in Fragment Ion−Molecule Complexes The ETD spectra of $(\mathrm{GLGGK} + 2\mathrm{H})^{2+}$ showed that backbone cleavages of the Gly-Gly and Gly-Lys N−Cα bonds involved hydrogen atom transfers forming the corresponding $(\boldsymbol{z_2} + \mathrm{H})^{+}$ and $(\boldsymbol{z_1} + \mathrm{H})^{+}$ fragment ions (Table1). In contrast, cleavage between Leu-Gly residues did not result in a hydrogen transfer forming $(\boldsymbol{z_4} + \mathrm{H})^{+}$ ions. Furthermore, the energy analysis indicated that the complementary ***c*** fragments, both neutrals and ions, were substantially more stable in the form of amide tautomers rather than enolimines. This raised the possibility of hidden exothermic rearrangements occurring in the course of the dissociations and resulting in lower-energy products. Proton and hydrogen atom transfers were investigated with complex $\mathbf{12}^{+\bullet}$, which is the first intermediate on the pathway leading to the observed $[\boldsymbol{z_4}^{\bullet} + \boldsymbol{c_1}$ neutral] and putative $[(\boldsymbol{z_4} + \mathrm{H})^{+} + (\boldsymbol{c_1} - \mathrm{H})\bullet]$ dissociation products. This can readily proceed by Lys proton migration through TS12 (at 6 kJ mol^{-1} relative to $\mathbf{21}^{+\bullet}$) followed by OH proton migration back to the Lys amine, forming the very stable $\boldsymbol{c_1}$ amide complex $\mathbf{22}^{+\bullet}$ at −42 kJ mol^{-1} relative to $\mathbf{12}^{+\bullet}$ and −105 kJ mol^{-1} relative to $\mathbf{1a}^{+\bullet}$. Dissociation of complex $\mathbf{22}^{+\bullet}$ to the $\boldsymbol{c_1}$ neutral amide and $\boldsymbol{z_4}^{\bullet}$ ion was 80 kJ mol^{-1} endothermic.

Isomerizations proceeding by H atom migration and leading to both the putative [($\boldsymbol{z_4}$ + H)$^+$ + ($\boldsymbol{c_1}$ − H)•] and observed [($\boldsymbol{y_1}$+ H)$^+$ + ($\boldsymbol{b_4}$ − H)•] dissociation products were investigated following several pathways that were combined with proton migrations to form the ($\boldsymbol{c_1}$ − H)• radical as the more stable amide tautomer. The radical transfer was presumed to involve one of the Cα-hydrogens in the $\boldsymbol{c_1}$ and $\boldsymbol{b_4}$ fragments. The H atom transfer reactions showed TS energies of 69−105 kJ mol^{-1}, which was in the same range as reported by Bythell for glycine cation-radical oligomers.[54]

2.4. Discussion

The computational analysis of peptide cation-radical structures and reactions revealed some interesting features. Electron attachment to the most stable dication structure **1a**$^{2+}$ proceeded to the zwitterionic cation radical **1a**$^{+\bullet}$ as a local energy minimum on the potential energy surface of the ground electronic state. In contrast, electron attachment that was steered to the other amide groups in **1a**$^{2+}$, **1c**$^{2+}$, and **1i**$^{2+}$ resulted in proton migrations forming aminoketyl radicals **2a**$^{+\bullet}$−**4**$^{+\bullet}$.

Cation radical **1a**$^{+\bullet}$ was only marginally stable with respect to an exothermic proton migration, quenching the amide anion radical and forming the aminoketyl radical **6**$^{+\bullet}$. These results indicate that amide anion-radicals, which have the electronic structure of amide π* states, have intrinsic basicities that exceed those of the Lys and N-terminal amino groups. The present results are consistent with the Utah-Washington model of ExD which posits that amide π* states produced by electron attachment are superbases that undergo exothermic proton migrations that convert them to aminoketyl radical intermediates.[11,14]

A novel feature revealed by the present study is the facile formation of structures **9**$^{+\bullet}$ and **10**$^{+\bullet}$ that are protonated at the amide nitrogen. These indicate that the amide π* states produced by electron attachment can isomerize by N-protonation in addition to the previously considered O-protonation. Intermediates of the **9**$^{+\bullet}$ and **10**$^{+\bullet}$ type represent the missing link to backbone

cleavages forming ***y*** type fragment ions via energetically plausible pathways. In the particular case of the GLGGK peptide, the formation of the $\boldsymbol{y_1}^+$ and $\boldsymbol{b_4}^{\bullet}$ fragments was disfavored by the high energy of the neutral radical.

Attempts to isomerize $\mathbf{1a}^{+\bullet}$ by proton migration from a proximate neutral Gly_3 amide group led to a dynamically unstable intermediate ($\mathbf{5}^{+\bullet}$) that was expected to isomerize back to $\mathbf{1a}^{+\bullet}$. This result is consistent with the previous analysis of a similar isomerization in $(AAVAR + 2H)^{+\bullet}$,[51] indicating that intermediates like $\mathbf{5}^{+\bullet}$ are unlikely to play a role in backbone dissociations. This casts further doubt on the "nonlocal" mechanism of ECD[5] (for a more detailed discussion see ref 14).

The backbone N−Cα cleavages can be considered to originate from radical intermediates such as amide zwitterions or aminoketyl radicals. The aminoketyl intermediates are unlikely to interconvert by hydrogen atom transfers in competition with N−Cα bond cleavages. This stems from the calculated relative energies that place $\mathbf{6}^{+\bullet}$ as the global aminoketyl radical minimum that should dominate at equilibrium. However, dissociations starting from $\mathbf{6}^{+\bullet}$ prefer loss of ammonia, which would competitively suppress backbone cleavages, in contradiction with the experimental data.

Structures $\mathbf{1a}^{+\bullet}$ and $\mathbf{6}^{+\bullet}$ are reactive intermediates for the competitive loss of ammonia and cleavage of the Gly1-Leu N−Cα bond that collectively account for 33% of fragmentations. Cleavage of the Leu-Gly3 N−Cα bond can proceed from $\mathbf{3}^{+\bullet}$ by a standard aminoketyl mechanism or from $\mathbf{2a}^{+\bullet}$ by an enol-type cleavage through TS8. These dissociations are collectively abundant, leading to $\boldsymbol{z_3}^{\bullet}$ fragment ions that account for 10% of ETD fragments. Interestingly, the enol cleavage in $\mathbf{2a}^{+\bullet}$ is reversible and therefore kinetically disfavored due to

the high energy of the incipient $(\boldsymbol{z_3} + \boldsymbol{c_2})^{+\bullet}$ complex. Hence, most of $\boldsymbol{z_3}^{\bullet}$ fragment ions is presumed to arise from $\mathbf{3}^{+\bullet}$ by a standard aminoketyl mechanism.

Cleavage of the Gly_3-Gly_4 N−Cα bond can proceed from the Gly_3 aminoketyl radicals $\mathbf{2a}^{+\bullet}$, $\mathbf{2b}^{+\bullet}$, and $\mathbf{7}^{+\bullet}$, which are readily accessible by electron attachment followed by a collapse to the ground electronic states of the pertinent aminoketyl radicals. In contrast, the Gly_3-Gly_4 bond cleavage is less abundant upon ETD, leading to the formation of the minor $\boldsymbol{z_3}^{\bullet}$ fragment ions at only 3%. We note that structures $\mathbf{2a}^{+\bullet}$ and $\mathbf{2b}^{+\bullet}$ are chiefly accessible from very minor precursor ion conformers and thus may not appreciably contribute to the formation of $\boldsymbol{z_3}^{\bullet}$ fragment ions. Finally, cleavage of the Gly_4-Lys N−Cα bond can proceed from the Gly_4 aminoketyl radical $\mathbf{4}^{+\bullet}$ via a standard mechanism, or from $\mathbf{8}^{+\bullet}$−$\mathbf{10}^{+\bullet}$ via the novel mechanism depicted by TS5. This dissociation must be accompanied by a proton transfer in the very stable $(\boldsymbol{z_1} + \boldsymbol{c_4})^{+\bullet}$ complex $13^{+\bullet}$ to proceed to the formation of the abundant $\boldsymbol{c_4}^{+}$ fragment ion (11%) rather than the $\boldsymbol{z_1}^{\bullet}$, which is barely detectable upon ETD.

2.5. Conclusion

On the basis of the analysis of the dissociation pathways and TS energies in GLGGK cation-radicals, we arrive at the conclusion that the formation of the backbone and other fragments is not completely governed by kinetically competitive reactions. Rather, the reaction course is set by the structure of the reactive intermediate, a zwitterion or an aminoketyl radical, accessed by electron transfer. From this point of view, the individual TS energies affect the kinetics of only those dissociations that originate from a common reactant. In contrast, a large part of the dissociation branching occur at the stage where the reactive intermediates are formed by vibronic transitions from the electronic states developing in the course of electron transfer. These conclusions are in line with previous studies of peptide cation-radical dissociations where

fragment branching ratios calculated on the basis of competitive kinetic models did not reflect experimental values from ETD mass spectra.[8,15]

2.6. References

(1) Zubarev, R. A.; Kelleher, N. L.; McLafferty, F. W. *J. Am. Chem. Soc.* **1998**, *120* (13), 3265–3266.

(2) Syka, J. E. P.; Coon, J. J.; Schroeder, M. J.; Shabanowitz, J.; Hunt, D. F. *Proc. Natl. Acad. Sci. U. S. A.* **2004**, *101* (26), 9528–9533.

(3) Coon, J. J. *Anal. Chem.* **2009**, *81* (9), 3208–3215.

(4) Mihalca, R.; Kleinnijenhuis, A. J.; McDonnell, L. A.; Heck, A. J. R.; Heeren, R. M. A. *J. Am. Soc. Mass Spectrom.* **2004**, *15* (12), 1869–1873.

(5) Patriksson, A.; Adams, C.; Kjeldsen, F.; Raber, J.; van der Spoel, D.; Zubarev, R. A. *Int. J. Mass Spectrom.* **2006**, *248* (3), 124–135.

(6) František Tureček; Chen, X.; Hao, C. *J. Am. Chem. Soc.* **2008**, *130* (27), 8818–8833.

(7) Hamidane, H. B.; He, H.; Tsybin, O. Y.; Emmett, M. R.; Hendrickson, C. L.; Marshall, A. G.; Tsybin, Y. O. *J. Am. Soc. Mass Spectrom.* **2011**, *20* (6), 1182–1192.

(8) Moss, C. L.; Chung, T. W.; Cerovský, V.; Turecek, F. *Collect. Czechoslov. Chem. Commun.* **2011**, *76* (4), 295–309.

(9) Prell, J. S.; O'Brien, J. T.; Holm, A. I. S.; Leib, R. D.; Donald, W. A.; Williams, E. R. *J. Am. Chem. Soc.* **2008**, *130* (38), 12680–12689.

(10) Chung, T. W.; Tureček, F. *Int. J. Mass Spectrom.* **2011**, *301* (1–3), 55–61.

(11) Syrstad, E. A.; Tureček, F. *J. Am. Soc. Mass Spectrom.* **2005**, *16* (2), 208–224.

(12) Skurski, P.; Sobczyk, M.; Jakowski, J.; Simons, J. *Int. J. Mass Spectrom.* **2007**, *265* (2–3), 197–212.

(13) Neff, D.; Sobczyk, M.; Simons, J. *Int. J. Mass Spectrom.* **2008**, *276* (2–3), 91–101.

(14) Tureček, F.; Julian, R. R. *Chem. Rev.* **2013**.

(15) Tureček, F.; Chung, T. W.; Moss, C. L.; Wyer, J. A.; Ehlerding, A.; Holm, A. I. S.; Zettergren, H.; Nielsen, S. B.; Hvelplund, P.; Chamot-Rooke, J.; Bythell, B.; Paizs, B. *J. Am. Chem. Soc.* **2010**, *132* (31), 10728–10740.

(16) Moss, C. L.; Chung, T. W.; Wyer, J. A.; Nielsen, S. B.; Hvelplund, P.; Tureček, F. *J. Am. Soc. Mass Spectrom.* **2011**, *22* (4), 731–751.

(17) Świerszcz, I.; Skurski, P.; Simons, J. *J. Phys. Chem. A* **2012**, *116* (7), 1828–1837.

(18) Kjeldsen, F.; Haselmann, K. F.; Budnik, B. A.; Jensen, F.; Zubarev, R. A. *Chem. Phys. Lett.* **2002**, *356* (3–4), 201–206.

(19) Fung, Y. M. E.; Chan, T.-W. D. *J. Am. Soc. Mass Spectrom.* **2005**, *16* (9), 1523–1535.

(20) Fälth, M.; Savitski, M. M.; Nielsen, M. L.; Kjeldsen, F.; Andren, P. E.; Zubarev, R. A. *Anal. Chem.* **2008**, *80* (21), 8089–8094.

(21) Liu, J.; Liang, X.; McLuckey, S. A. *J. Proteome Res.* **2008**, *7* (1), 130–137.

(22) Han, H.; Xia, Y.; McLuckey, S. A. *J. Proteome Res.* **2007**, *6* (8), 3062–3069.

(23) Chung, T. W.; Tureček, F. *J. Am. Soc. Mass Spectrom.* **2010**, *21* (8), 1279–1295.

(24) Xia, Q.; Lee, M. V.; Rose, C. M.; Marsh, A. J.; Hubler, S. L.; Wenger, C. D.; Coon, J. J. *J. Am. Soc. Mass Spectrom.* **2011**, *22* (2), 255–264.

(25) Moss, C. L.; Liang, W.; Li, X.; Tureček, F. *J. Am. Soc. Mass Spectrom.* **2012**, *23*, 446–459.

(26) Carpino, L. A.; Han, G. Y. *J. Am. Chem. Soc.* **1970**, *92* (19), 5748–5749.

(27) Coste, J.; Le-Nguyen, D.; Castro, B. *Tetrahedron Lett.* **1990**, *31* (2), 205–208.

(28) Marek, A.; Pepin, R.; Peng, B.; Laszlo, K. J.; Bush, M. F.; Tureček, F. *J. Am. Soc. Mass Spectrom.* **2013**, *24* (11), 1641–1653.

(29) Pringle, S. D.; Giles, K.; Wildgoose, J. L.; Williams, J. P.; Slade, S. E.; Thalassinos, K.; Bateman, R. H.; Bowers, M. T.; Scrivens, J. H. *Int. J. Mass Spectrom.* **2007**, *261* (1), 1–12.

(30) Giles, K.; Williams, J. P.; Campuzano, I. *Rapid Commun. Mass Spectrom.* **2011**, *25* (11), 1559–1566.

(31) Williams, J. P.; Brown, J. M.; Campuzano, I.; Sadler, P. J. *Chem. Commun.* **2010**, *46* (30), 5458–5460.

(32) Bush, M. F.; Hall, Z.; Giles, K.; Hoyes, J.; Robinson, C. V.; Ruotolo, B. T. *Anal. Chem.* **2010**, *82* (22), 9557–9565.

(33) Mason, E. A.; McDaniel, E. W. *Transport Properties of Ions in Gases*; Wiley: New York, 1998.

(34) Moss, C. L.; Chamot-Rooke, J.; Nicol, E.; Brown, J.; Campuzano, I.; Richardson, K.; Williams, J. P.; Bush, M. F.; Bythell, B.; Paizs, B.; Turecek, F. *J. Phys. Chem. B* **2012**, *116* (10), 3445–3456.

(35) Tureček, F. *J. Phys. Chem. A* **1998**, *102* (24), 4703–4713.

(36) Rablen, P. R. *J. Am. Chem. Soc.* **2000**, *122* (2), 357–368.

(37) Furche, F.; Ahlrichs, R. *J. Chem. Phys.* **2002**, *117* (16), 7433.

(38) Reed, A. E.; Weinstock, R. B.; Weinhold, F. *J. Chem. Phys.* **1985**, *83* (2), 735.

(39) Gilbert, R. G.; Smith, S. C. *Theory of Unimolecular and Recombination Reactions*; Blackwell Scientific Publications: Oxford, 1990.

(40) Frank, A. J.; Sadílek, M.; Ferrier, J. G.; Tureček, F. *J. Am. Chem. Soc.* **1997**, *119* (50), 12343–12353.

(41) Mesleh, M. F.; Hunter, J. M.; Shvartsburg, A. A.; Schatz, G. C.; Jarrold, M. F. *J. Phys. Chem.* **1996**, *100* (40), 16082–16086.

(42) Shvartsburg, A. A.; Jarrold, M. F. *Chem. Phys. Lett.* **1996**, 86–91.

(43) Campuzano, I.; Bush, M. F.; Robinson, C. V.; Beaumont, C.; Richardson, K.; Kim, H.; Kim, H. I. *Anal. Chem.* **2012**, *84* (2), 1026–1033.

(44) Gellene, G. I.; Cleary, D. A.; Porter, R. F. *J. Chem. Phys.* **1982**, *77* (7), 3471–3477.

(45) Gellene, G. I.; Porter, R. F. *Acc. Chem. Res.* **1983**, *16*, 200–207.

(46) Shaffer, S. A.; Tureček, F. *J. Am. Chem. Soc.* **1994**, *116*, 8647–8653.

(47) Nguyen, V. Q.; Sadilek, M.; Ferrier, J.; Frank, A. J.; Tureček, F. *J. Phys. Chem. A* **1997**, *101* (20), 3789–3799.

(48) Yao, C.; Tureček, F. *Phys. Chem. Chem. Phys.* **2005**, *7* (5), 912–920.

(49) Holm, A. I. S.; Hvelplund, P.; Kadhane, U.; Larsen, M. K.; Liu, B.; Nielsen, S. B.; Panja, S.; Pedersen, J. M.; Skrydstrup, T.; Støchkel, K.; Williams, E. R.; Worm, E. S. *J. Phys. Chem. A* **2007**, *111* (39), 9641–9643.

(50) von Helden, G.; Hsu, M.-T.; Gotts, N.; Bowers, M. T. *J. Phys. Chem.* **1993**, *97*, 8182.

(51) Tureček, F.; Moss, C. L.; Chung, T. W. *Int. J. Mass Spectrom.* **2012**, *330–332*, 207–219.

(52) Tureček, F.; Panja, S.; Wyer, J. A.; Ehlerding, A.; Zettergren, H.; Nielsen, S. B.; Hvelplund, P.; Bythell, B.; Paizs, B. *J. Am. Chem. Soc.* **2009**, *131* (45), 16472–16487.

(53) Wodrich, M. D.; Zhurov, K. O.; Vorobyev, A.; Ben Hamidane, H.; Corminboeuf, C.; Tsybin, Y. O. *J. Phys. Chem. B* **2012**, *116* (35), 10807–10815.

(54) Bythell, B. J. *J. Phys. Chem. A* **2013**, *117* (6), 1189–1196.

(55) Frisch, M. J.; Trucks, G. W.; Schlegel, H. B.; Scuseria, G. E.; Robb, M. A.; Cheeseman, J. R.; Scalmani, G.; Barone, V.; Mennucci, B.; Petersson, G. A.; Nakatsuji, H.; Caricato, M.; Li, X.; Hratchian, H. P.; Izmaylov, A. F.; Bloino, J.; Zheng, G.; Sonnenberg, J. L.; Hada, M.; Ehara, M.; Toyota, K.; Fukuda, R.; Hasegawa, J.; Ishida, M.; Nakajima, T.; Honda, Y.; Kitao, O.; Nakai, H.; Vreven, T.; Montgomery, J. A., Jr.; Peralta, J. E.; Ogliaro, F.; Bearpark, M.; Heyd, J. J.; Brothers, E.; Kudin, K. N.; Staroverov, V. N.; Kobayashi, R.; Normand, J.; Raghavachari, K.;Rendell, A.; Burant, J. C.; Iyengar, S. S.; Tomasi, J.; Cossi, M.; Rega, N.; Millam, J. M.; Klene, M.; Knox, J. E.; Cross, J. B.; Bakken, V.; Adamo, C.; Jaramillo, J.; Gomperts, R.; Stratmann, R. E.; Yazyev, O.; Austin, A. J.; Cammi, R.; Pomelli, C.; Ochterski, J. W.; Martin, R. L.; Morokuma, K.; Zakrzewski, V. G.; Voth, G. A.; Salvador, P.; Dannenberg, J. J.; Dapprich, S.; Daniels, A. D.; Farkas, O.; Foresman, J. B.; Ortiz, J. V.; Cioslowski, J.; Fox, D. J. et al. Gaussian09, revision A.02; Gaussian, Inc: Wallingford, CT, 2009.

(56) Zhu, L.; Hase, W. L. Quantum Chemistry Program Exchange: Program No. QCPE 644.; Indiana University: Bloomington, Indiana, 1994

Chapter 3.

Rationally Designed Heptapeptides for Electron Based Fragmentation Methods. Precursor Ion Structural Studies and Electron Transfer Dissociation Fragment Behaviors.

Abstract The experimental collisional cross sections for a series of rationally designed heptapeptide ions, differing only in the order in which the amino acids are assembled, derived from ion mobility measurements are compared to the results of low energy calculated conformer searching by an exhaustive routine and are examined for agreement and the ability of computations to predict the correct gas phase experimental structures. Electron transfer dissociation (ETD) of these ions show that amino acid sequential order does matter as differing types of charge reduced cation radicals are revealed by MS^3 collisional activation simply from changing the order in which these residues are arranged. A substantial presence of reduced, but not fragmented, ions are present in some sequences raising the question of what causes this previously noted phenomenon in the absence of histidine residues. Photo activation of cation radicals produced from ETD of these ions show fragmentations unique to this activation method indicating the possibility of dissociative excited electronic states.

3.1. Introduction

Peptide conformation in the gas phase is believed to play a role in the fragmentation mechanism for electron based fragmentation methods.[1] There have been many studies of the structures and folding patterns of condensed phase peptides and proteins.[2,3] These NMR and crystal structure[4] based methods have been of great use in learning the functions and folding patterns of proteins. But ionization and introduction into the gas phase does not necessarily preserve the solution phase conformations of peptide and protein ions, though so called "native electrospray"

conditions are believed to preserve protein quaternary structures.[5] A peptide fragment of the protein melectin was studied with circular dichroism and found to have a helical[6] structure in solution but a globular gas phase structure.[7] Also, experimental evidence shows that in solution amino acids have a zwitterionic structure, but ionization tends to create positively charged canonical structures in the gas phase.[8] In the interest of discerning the fragmentation mechanism for electron based methods it is desirable to study the conformation of candidate ions in the gas phase directly.

Fragmentation of multiply charged peptide ions via electron based methods has been shown to produce a rich spectrum of fragment ions, often providing more complete sequence information in a manner complementary to information provided via collisional activation. (See the introduction chapter of this work for an example of improved sequence information from ETD versus CID based fragmentations.) There have been cases where the electron is absorbed but no fragmentations or reduced fragmentations are observed[9–11] dubbed ETnoD. In the cases of histidine containing peptides, it was believed that the radical is stabilized in the imidazole side chain of the histidine.[12] When subjected to electron transfer dissociation, the heptapeptides studied in this work showed a pronounced tendency to form intact, charge-reduced, ions without containing histidine residues.

In this work, extensive computational modeling is used to generate candidate gas phase structures for a small library of related, highly basic peptides which differ only in the sequence order in which their amino acids are arranged. The peptides were designed so that they would hopefully form tightly folded, globular shapes in the gas phase. Ion mobility measurements of the gas phase collision cross sections of the peptide ions are measured and used to validate the candidate structures. ETD of these peptide ions is shown to generate substantial amounts of

charge-reduced metastable, intact peptide ions. Radical cation fragments of these heptapeptides, generated by ETD, show different fragmentations when subjected to different MS^3 activations. Photon based activation of $z^{\bullet}$ ion radicals via 355nm laser light produce different fragments than CID of the same $z^{\bullet}$ ions.

3.2. Experimental

3.2.1. Materials Heptapeptides LKGPADR, LRGPADK, KLGPADR, RLGPADK were purchased from United Biosystems (Cabin John, MD) at 95% purity or better and used without further purification. Heptapeptides LKGLADR, LRGLADK, KLGLADR, RLGLADK were purchased from Genscript (Piscatawny, NJ) at 95% purity or better and were used without further purification. Solvents were purchased from Fisher and used as received. Heptapeptides were dissolved in electrospray solvent (MeOH:water:acetic acid, 50:50:1) to a concentration of approximately10μM.

3.2.2. Ion Mobility Methods Relative ion mobility drift times were acquired on a Waters Synapt G2 using the traveling wave ion mobility (TWIM) methodology with nitrogen as the mobility gas. Absolute ion mobilities were measured on a Synapt G2 with a custom designed drift tube[13] in place of the standard TWIM mobility cell also in helium. Individual measurements concerned singly, doubly and triply charged ions generated from individual parent peptides. The reported data are averages of 3-4 replicate measurements, each based on 6-10 field-dependent arrival times with a linearity coefficient of $r^2 \geq 0.999$.

3.2.3. ETD Methods Heptapeptides were dissolved at 5-10μM in methanol/water/acetic acid (50/50/1) and electrosprayed to form precursor cations for ETD. Electrospray ionization of the heptapeptides led to triply protonated $(M+3H)^{3+}$, doubly protonated $(M+2H)^{2+}$ and singly protonated $(M+H)^{+}$ ions typically in an (50:35:1) ratio respectively. Electron transfer

dissociation (ETD) mass spectra were measured on a Thermo Fisher Scientific LTQ XL linear ion trap instrument equipped with an auxilary negative ion chemical ionization source for the production of the fluoranthene anion radical electron transfer reagent. Precursor ions were mass isolated with a typical width of 2 *m/z* and allowed to reacted with fluoranthene anions for a typical reaction time of 200ms. Higher order CID MS^n experiments were measured with a 30ms activation time at normalized collision energies sufficient to afford 75-90% depletion of the precursor ions. High resolution ETD spectra were also acquired on an Orbitrap LTQ Velos instrument with similar MS/MS settings. Resolving power was set at 100,000 to ensure resolution of nominally identical masses. ETD and MS^3 and MS^4 were also measured on a Bruker amaZon 3D ion trap equipped with a fluoranthene anion radical source for production of ETD reagent. MS^3 and MS^4 CID activation times were 30ms.

3.2.4. Laser System The Ekspla laser system consists of a 20Hz pulsed Nd:YAG pump laser outputting up to 226mJ per pulse of 1064nm infrared photons. The infrared photons are frequency doubled through a non-linear BBO crystal to generate the 532nm product beam. The 532nm product beam is then passed through a second non-linear BBO crystal and the resulting frequency tripled output at 355nm is passed through a dichroic mirror to remove surviving 532 and 1064nm photons and then directed towards the mass spectrometer. The maximum output power of the third harmonic beam is limited to 55mJ per pulse. The pulse length is 3-6ns. In these experiments the laser power was kept to 18mJ per pulse.

3.2.5. Calculation Methods Peptide ion structures were generated using the ConformSearch engine described previously.[14] Briefly, this consists of (1) selection of starting structures for protonated ion tautomers; (2) molecular dynamics trajectory calculations run at eight temperatures (300, 345, 397, 457, 525, 604, 695, and 800 K) using the CHARMM force field

and a replica exchange protocol to generate 800,000 conformer structures for each peptide ion tautomer; (3) sampling 8000 structures for full geometry optimization with the semiempirical PM6 method; (4) sorting out conformer families according to their hydrogen bonding patterns, and compacting duplicates; (5) density-functional theory (DFT) single-point energy calculations with the hybrid B3LYP functional and the 6-31+G(d,p) basis set on ca. 120-200 lowest energy conformers in each family; (6) resorting the conformers according to B3LYP single-point energies; (7) full gradient geometry optimization with B3LYP and M06-2X/6-31+G(d,p) of 30-40 lowest-energy conformers; (8) harmonic frequency calculations of 10-20 lowest energy conformers, and (9) single-point-energy calculations with B3LYP, M06-2X and Møller-Plesset perturbational theory truncated at second order with valence-electron only excitations (MP2(frozen core)), all with the 6-311++G(2d,p) basis set. Select ion structures were reoptimized with ωB97XD DFT calculations employing the 6-31+G(d,p) basis set, and used for ωB97XD/6-311++G(2d,p) single-point energy calculations. All electronic structure calculations were performed with the Gaussian 09 suite of programs.[26]

Collisional cross sections pertinent to fully optimized ion conformer structures and B3LYP/6-311++G(2d,p) atomic charges were calculated using the Mobcal program[15,16] with the parameters set by Campuzano et al.[17] Comparisons between the parameters optimized for drug-like molecules in Campuzano et al's work with the default parameters were made and found to produce no significant differences for our results.

3.3. Results

3.3.1. Ion Mobility Measurements Ion mobility measurements of the heptapeptide library and their ETD fragments were carried out on a Waters Synapt G2 using the traveling wave ion mobility (TWIMS) technology.[18] TWIMS provides relative drift times which imply the *relative*

gas phase sizes of various analyte ions but do not give absolute cross sections. In order to obtain absolute collisional cross sections (CCS) for the peptide library, a subset of the library was selected and measured on a modified Synapt G2 with a custom designed and built drift tube.[13] The procedure of Ruotolo et al[19] was then followed to calibrate the TWIMS derived drift times into absolute collisional cross sections. Briefly, the drift time t_D was corrected for mass-dependent flight times via equation (1):

$$t'_D = t_D - \left[\frac{c\sqrt{\frac{m}{z}}}{1000}\right] - \left(\frac{10}{V_{Tr}}\right) \quad \textbf{(1)}$$

Here c represents the Enhanced Duty Cycle delay coefficient from the TWIM Synapt G2 which was 1.5800 and V_{Tr} represents the wave velocity in the transfer region. The ions experience a constant time in the transfer region which is accounted for by the $10/V_{Tr}$ term (10 cm transfer tube). The absolute cross sections of ions were measured on the Synapt G2 with a drift tube and then corrected for charge state z and reduced mass μ via equation (2):

$$\Omega' = \frac{\Omega}{z * \frac{1}{\sqrt{\mu}}} \quad \textbf{(2)}$$

A plot of ln t'_D vs ln Ω' was made and a linear fit to the data was found. The slope from this plot was taken as the "exponential factor" X and used to generate a re-corrected drift time t''_D via equation (3)

$$t''_D = t'_D \wedge X * z * \frac{1}{\sqrt{\mu}} \quad \textbf{(3)}$$

A new plot of Ω vs t''_D yields the readily used calibration plot. TWIM drift times can be corrected and then absolute cross sections found from this calibrated relationship. The data for calibrants used are given in Table 2.

Peptide	Charge	Ω_{abs} (Å^2)[a]	Ω_{cal} (Å^2)[b]
KLG**P**ADR	1+	185.0 ± 0.55[c]	187
	2+	195.4 ± 0.93	199
	3+	239.2 ± 4.4	244
KLG**L**ADR	2+		205
	3+		247
LKG**P**ADR	1+	192.6 ± 1.3	192
	2+	200.5 ± 1.1	202
	3+	226.6 ± 4.8	239
LKG**L**ADR	2+		204
	3+		241
LRG**P**ADK	1+	189.6 ± 0.9	
	2+	192.0 ± 1.5	200
	3+	221.4 ± 1.3	239
LRG**L**ADK	2+		204
	3+		245
RLG**P**ADK	1+	188.0 ± 1.3	184
	2+	190.1 ± 1.3	189
	3+	238.3 ± 1.4	230
RLG**L**ADK	2+		195
	3+		232

Table 5: Experimental Collision Cross Sections of Peptide Ions. [a]From 3-4 replicate measurements on the drift-tube instrument, each based on 6-10 field-dependent arrival times with a linearity coefficient r2 = 0.99971. [b]From calibrated TWIM measurements. [c]Standard deviations.

The absolute (Ω_{abs}) and calibrated TWIM collision cross section values (Ω_{cal}) for singly, doubly, and triply charged peptide ions are summarized in Table 1. The two data sets showed a linear correlation, $\Omega_{cal} = 1.0167\Omega_{abs}$, with a correlation coefficient $r^2 = 0.999$.

	$(M+2H)^{2+}$		$(M+3H)^{3+}$	
	Drift Tube	TWIMS	TWIMS	Drift Tube
KLGPADR	195.43721	199.07311	245.1939	239.16976
LKGPADR	200.53799	201.3925	238.28444	226.55205
RLGPADK	190.05347	189.71162	230.1102	238.29448
LRGPADK	192.00698	199.25914	238.05937	221.44133

Table 6: Calibrant Data and resulting cross sections from traveling wave measurements. Units are Å^2.

The root-mean-square deviation of Ω_{cal} relative to Ω_{abs} was 8 Å^2 or 3.5%, which provided an estimate of the accuracy of Ω_{cal} for ions for which Ω_{abs} were not available. The Ω_{abs} and Ω_{cal} showed relatively minor increases (1-5%) between the singly and doubly charged ions whereas

substantially greater increases (13-25%) were observed upon adding the third charge. The arrival time peaks for the parent doubly and triply charged ions showed single Gaussian-like intensity profiles (Figure 1).

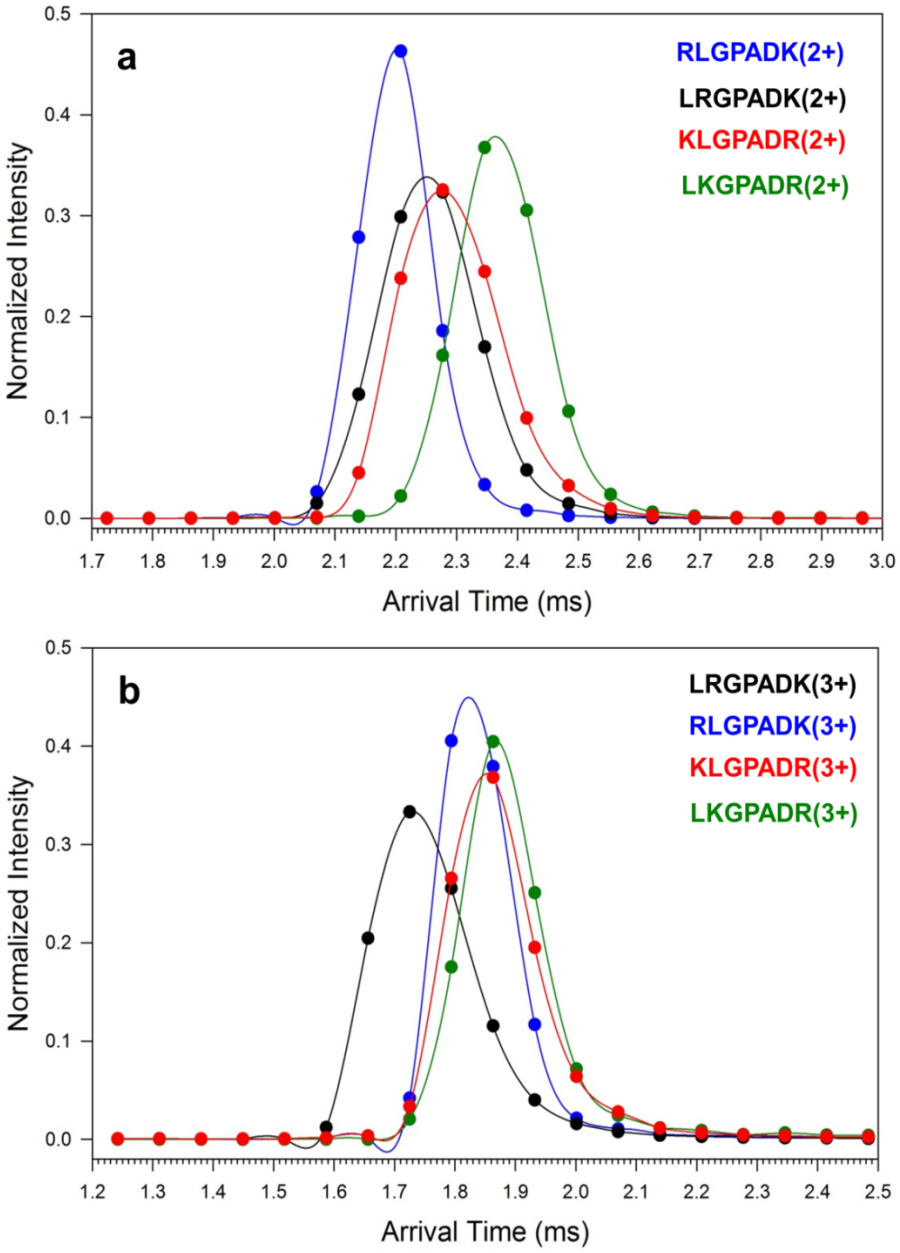

Figure 16: Arrival time profiles for (a) doubly charged proline containing heptapeptides and (b) triply charged proline containing heptapeptides.

The doubly charged parent peptide ions showed similar Ω_{abs} values which followed a slightly upward trend in the series RLGPADK < LRGPADK < KLGPADR < LKGPADR that

spanned the range of 190-200 $Å^2$. This trend was not preserved for triply charged ions where the Ω_{abs} values followed the series LRGPADK < LKGPADR < RLGPADK ≈ KLGPADR within the range of 221-239 $Å^2$. This indicated that the position of the charged residues affected the Ω_{abs} to within 5-10%.

Replacing proline with leucine in all doubly and triply charged ions resulted in a very minor increase of the Ω_{cal}, ranging from 0.8 to 3.2%. This may indicate that the proline β-turn affects the shape of these peptide ions to only a small extent. Accordingly, the charge dependent increase of the Ω_{cal} upon adding a third charge to the leucine-containing ions (18-20%) was similar to that observed for the proline peptide ion series. The differences between the Pro and Leu containing ions are substantially smaller than what would be expected on the basis of the estimated amino acid size parameters for singly charged ions with 5-10 residues that predict 15-19% larger cross sections for Leu peptides.[20,21]

3.3.2. Calculated Ion Structures To relate the experimental Ω to ion structures, we calculated the theoretical cross sections for families of lowest free-energy conformers of the peptide ions whose structures were produced by multi-step DFT and ab initio calculations. In general terms, the triply charged ions carry the protons on the three basic groups which are the *N*-terminal and Lys ε-amines and the Arg guanidine group. Hence, there is only one tautomer for each triply charged ion. The optimized structures of triply charged LKGPADR, KLGPADR, and RLGPADK ions pointed to specific conformations for the lowest free-energy ions. The relative free energies for the most stable conformers are summarized in Table 2. The lowest free-energy $LKGPADR^{3+}$ conformer **1** (Figure 2) displayed four hydrogen bonds to the charged groups, out of which three were for Lys and one for Arg, and one neutral H bond for the Asp carboxyl. The charged *N*-terminal amino group was extended out and internally solvated by a single hydrogen

bond to the Leu amide. A similar H-bonding pattern was found for conformer **2** which had 12-14 kJ mol^{-1} higher free energy than **1** at 298 K. The chief difference between these low-energy conformers was in the ψ_6 dihedral angle at the Asp residue as a result of rotation of the C-terminal Arg residue (Figure 2). A notable feature of these low-energy structures is the wide-open hinge at the Pro residue which is enforced by the strong hydrogen bond of the Lys ε-ammonium to the Ala amide carbonyl (Figure 2).

	Relative Free Energy[a]				ΔΩ[b]	
Ion	**B3LYP[c]**	**M06-2X[d]**	**ωB97XD[e]**	**MP2**	**B3LYP[f]**	**M06-2X[g]**
LKGPADR^{3+}						
1	0	0	0	0	0.1 (0.5)[h]	−2.0 (−1.3)[h]
2	14	11.7	13.8	12.7	−0.2 (0.3)	−2.0 (−1.2)
KLGPADR^{3+}						
3	0	0	0	0	−0.7 (−2.7)	−3.2 (−5.2)
4	−7.6	−2.5	−7.5	−10.2	−0.4 (−2.3)	−2.7 (−4.6)
5	−20	6.6	−11.2	−15.1	−4.1 (−6.0)	−7.3 (−9.1)
RLGPADK^{3+}						
6	15.8	15.4	-	-	−8.1 (−4.8)	−9.8 (−6.5)
7	8.6	12.9	-	-	−5.3 (−1.9)	−7.2 (−3.9)
8	0	0	0	0	−6.7 (−3.3)	−9.4 (−6.1)
9	−0.9	18.9	14.4	-	−6.3 (−2.9)	−8.7 (−5.4)
10	1.4	24.1	14.1	-	−5.8 (−2.4)	−7.5 (−4.2)
11	−7.0	23.1	13.9	9.9	−5.8 (−2.4)	−7.5 (−4.2)

Table 7: Calculated Relative Energies and Cross Section Fits of Triply Charged Ion Conformers. [a]In kJ mol-1 including zero-point energy corrections and 298 K enthalpies and entropies. [b]Per cent differences between the calculated and experimental collision cross sections. [c]From B3LYP/6-311++G(2d,p) single-point energies on B3LYP/6-31+G(d,p) optimized geometries. [d]From M06-2X/6-311++G(2d,p) single-point energies on M06-2X/6-31+G(d,p) optimized geometries. [e]From ωB97XD/6-311++G(2d,p) single-point energies on ωB97XD/6-31+G(d,p) optimized geometries. [f]Smallest differences (%) between the calculated collision cross sections based on B3LYP/6-31+G(d,p) optimized geometries and Ωabs. [g]Smallest differences (%) between the calculated collision cross sections based on M06-2X/6-31+G(d,p) optimized geometries and Ωabs. [h]Values in parentheses are the smallest differences (%) between the calculated Ωth and Ωcal.

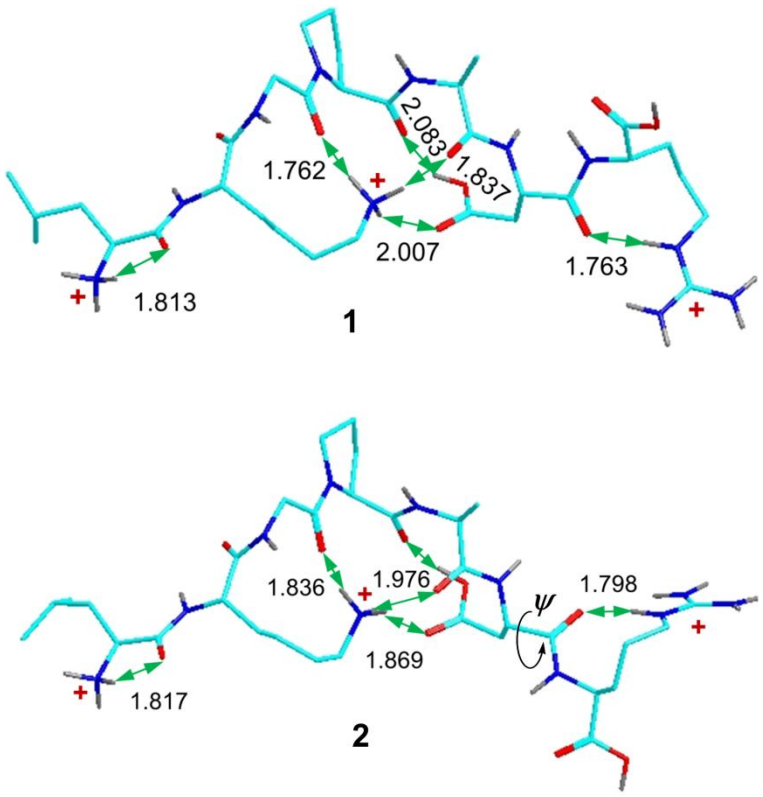

Figure 17: B3LYP/6-31+G(d,p) optimized structures of lowest-free energy LKGPADR3+ conformers. Atom color coding is as follows: Turquoise = C, blue = N, red = O, gray = H. Only exchangeable hydrogens in polar groups are shown. Green arrows indicate hydrogen bonds

The lowest free-energy KLGPADR^{3+} conformers **3**-**5** showed different H-bonding patterns (Figure 3). In the KLGPADR^{3+} conformer **3**, each of the charged *N*-terminal and Lys ammonium groups was internally solvated by two hydrogen bonds, whereas the Arg charged group had only one H-bond to the Asp amide. The hydrogen bonding of the *N*-terminal ammonium group forced the backbone to make a loop with hinges at the Leu and Pro residues. A similar pattern was found for the lower-energy conformer **4** where the backbone loop was strengthened by another H-bond of the *N*-terminal ammonium to the Asp carboxyl group. Structures **3** and **4** mainly differ in the orientation of the Arg residue which is caused by different ψ_5 torsional angles at Asp. In contrast, the *N*-terminal ammonium group in another conformer **5** was extended out and internally solvated by a single H-bond to the Lys amide. This weaker solvation of the *N*-terminal ammonium was compensated by tri-coordination of the Lys

ε-ammonium to the Gly and Ala amides and the C-terminal carboxyl that formed a side-chain loop affecting the peptide ion structure. The ion conformation was further shaped by a neutral H-bond of the C-terminal carboxyl to the Leu amide that formed a macrocyclic ring structure with hinges at Ala and Asp that was capped by the Lys ε-ammonium group. Another energetically favorable feature of **5** was the double H-bond solvation of the Arg charged group by the Asp amide and carboxyl groups.

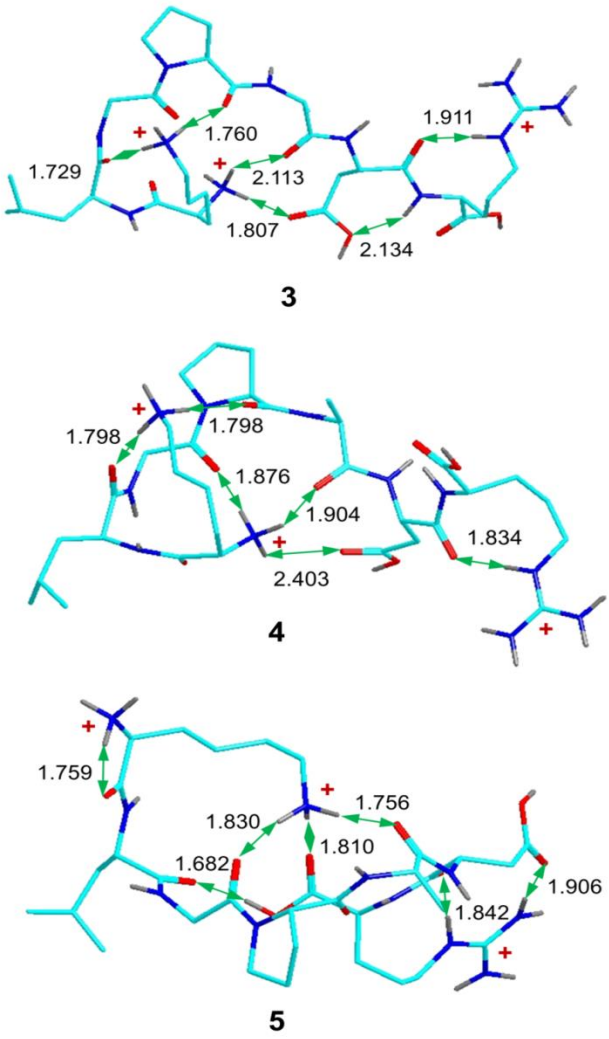

Figure 18: B3LYP/6-31+G(d,p) optimized structures of lowest-free energy KLGPADR3+ conformers. Structure description as in Figure 2.

The RLGPADK^{3+} ions also showed different folding patterns in low-free-energy conformers that differed in side-chain conformations and internal solvation of the charged groups

(Figure 4). In one group of conformers, represented by structure **6**, the Arg charged side chain group was internally solvated by a single H bond to the Arg amide, the *N*-terminal ammonium formed H-bonds to the Asp amide and carboxyl and Gly amide, and the Lys ammonium was solvated by the Leu, Pro, and Ala amides. Interestingly, another low-energy conformer (**7**) had an unfolded Arg side chain so the charged guanidinium group lacked internal solvation (not shown). In another major group (**8** and **9**), the Arg charged side chain group was internally solvated by the Asp side-chain carboxyl, the *N*-terminal ammonium formed H-bonds to the Asp amide and the C-terminal carboxyl, and the Lys ammonium was solvated by the Gly, Pro and Ala amide carbonyls. In **10** and **11**, the Arg side chain was H bonded to the Leu amide, the *N*-terminal ammonium formed H-bonds to the Asp amide and the C-terminal carboxyl, and the Lys charged group was hydrogen bonded to the Pro and Gly or Ala amide carbonyls.

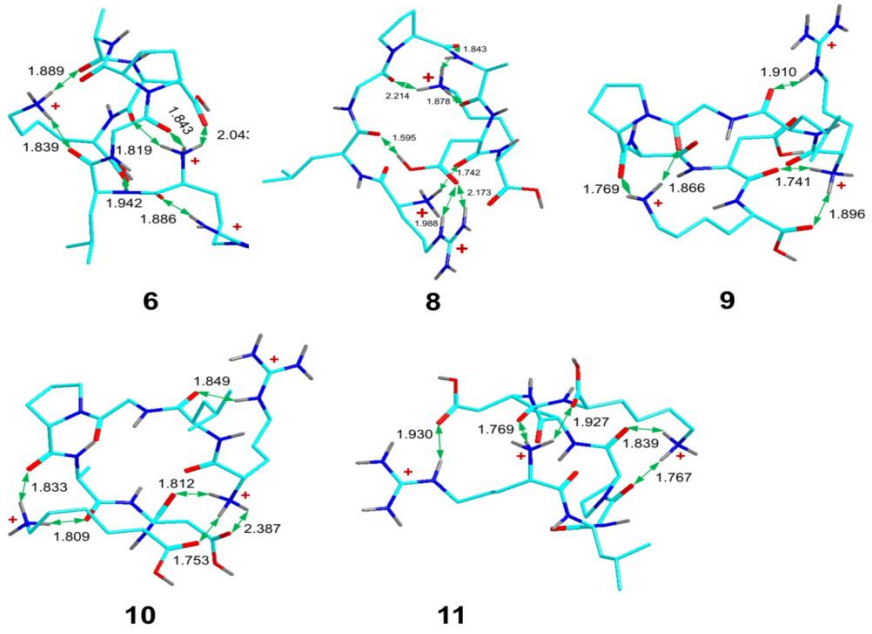

Figure 19: B3LYP/6-31+G(d,p) optimized structures of lowest-free energy RLGPADK3+ conformers. Structure description as in Figure 2.

3.3.2.1. Doubly Charged Ions

In contrast to the triply charged ions, the doubly charged ions allowed for the formation of three canonical and two zwitterionic tautomers from each peptide sequence, leading to 20 groups of conformers. Considering the substantial computational demands of the multi-step conformational analysis at the ConformSearch level of theory, addressing all 20 ion tautomers would be a daunting task. Therefore, we selected a limited number of doubly charged tautomers for each peptide sequence for exhaustive structure analysis. The relative free energies for the most stable conformers are shown in Table 4.

	Relative Free Energy[a]				ΔΩ(%)[b]	
Ion	**B3LYP**	**M06-2X[c]**	**ωB97XD[d]**	**MP2[e]**	**B3LYP[f]**	**M06-2X[g]**
LRGPADK^{2+}						
12	0	0	-	0	1.1 (2.2)[h]	2.3 (0.7)[h]
13	20.3	4.5	-	11.1	−1.1 (−0.2)	−0.5 (1.7)
14	12	2.4	-	28.5	0.2 (1.0)	1.4 (0.1)
15	27	30.5	-	27.2	−2.2 (−0.5)	0.2 (2.0)
16	1.6	3.8	-	-	1.9 (-2.2)	−1.3 (-0.8)
LKGPADR^{2+}						
17	−0.4	2.8	2.5	5.4	0.2 (−0.6)	1.2 (0.5)
19	0	0	0	0	−1.2 (−2.0)	0.4 (−0.4)
18	−10.1	3.3	1.7	3.5	0.9 (0.1)	−1.3 (1.4)
20	−9.2	2.7	2	3.4	0.1 (−0.7)	1.8 (1.0)
KLGPADR^{2+}						
21	0	0	0	0	5.0 (3.5)	2.5 (0.6)
22	12	4.1	-	12.3	−3.6 (−5.5)	−7.5 (−9.3)
23	8.1	4.3	7.5	6.8	5.0 (3.5)	2.7 (0.8)
24	−2.3	−5.2	1.2	3.1	5.6 (3.7)	3.0 (1.1)
RLGPADK^{2+}						
25	4	−4.8	2.8	2.5	−1.7 (−1.1)	0.3 (0.9)
26	0	0	0	0	1.1 (1.7)	−0.4 (0.2)
27	3.2	−7.5	−0.1	−2.0	−1.8 (−1.2)	0.3 (0.9)

Table 8: Calculated Relative Energies and Cross Section Fits of Doubly Charged Ion Conformers. [a]In kJ mol^{-1} including zero-point energy corrections and 298 K enthalpies and entropies. [b]Per cent differences between the calculated and experimental collision cross sections. [c]From M06-2X/6-311++G(2d,p) single-point energies on M06-2X/6-31+G(d,p) optimized geometries. [d]From ωB97XD/6-311++G(2d,p) single-point energies on ωB97XD/6-31+G(d,p) optimized geometries. [e]From MP2/6-311++G(2,p) single-point energies on B3LYP/6-31+G(d,p) optimized geometries. [f]Smallest differences (%) between the calculated collision cross sections based on B3LYP/6-31+G(d,p) optimized geometries and Ωabs. [g]Smallest differences (%) between the calculated collision cross sections based on M06-2X/6-31+G(d,p) optimized geometries and Ωabs. [h]Values in parentheses are the smallest differences (%) between the calculated Ωth and Ωcal..

Starting with $LRGPADK^{2+}$, exhaustive conformational search was performed for Asp and C-terminal carboxylate zwitterionic tautomers with an initial *trans* Gly-Pro amide configuration. A separate search starting from a *cis* Gly-Pro amide configuration resulted in *cis*-*trans* amide rotation to chiefly yield *trans* Gly-Pro conformers. The *cis* isomers that reached full geometry optimization were in general less stable than the low-energy *trans* isomers. The two lowest free-energy Asp-zwitterions (**12**, Figure 5**,** and **13,** not shown) showed multiple H-bonds, providing internal solvation to the charged groups. In both ions, the Asp carboxylate was internally solvated by the Arg and Lys charged groups whereas the *N*-terminal ammonium was remote and received internal solvation through H-bonding to the Pro and Ala amides. In the lowest free energy C-terminal zwitterion (**14**, Figure 5), the carboxylate participated in H-bonding to the Arg and *N*-terminal charged groups, whereas the Lys ammonium developed three H-bonds to the Gly, Pro, and Asp amides. It is worth noting that the C-terminal zwitterion **14** was thermochemically less stable than **12** and **13** but had a higher entropy which contributed to its low free energy. The different folding patterns in **12**, **13**, **14** , and related conformers **15** and **16** (not shown) had only very minor effects on the collision cross sections in these ions, as discussed in detail below.

Swapping the Lys and Arg residues in LRGPADK resulted in $LKGPADR^{2+}$ ions that were generated as Asp carboxylate zwitterions. The lowest free energy structures for these tautomers **17**-**20** showed a conserved folding pattern which is represented by structure **17** (Figure 5). In conformer **17**, the Asp carboxylate was positioned on the top of a highly folded structure where it was internally solvated by H-bonds from the Lys and N-terminal ammonium groups and a strong H-bond from the Leu amide. The Arg charged group was internally solvated by the Pro,

Gly, and Lys amide carbonyls. The ion conformation was further locked in by a H-bond between the Lys ammonium and the C-terminal carboxyl group.

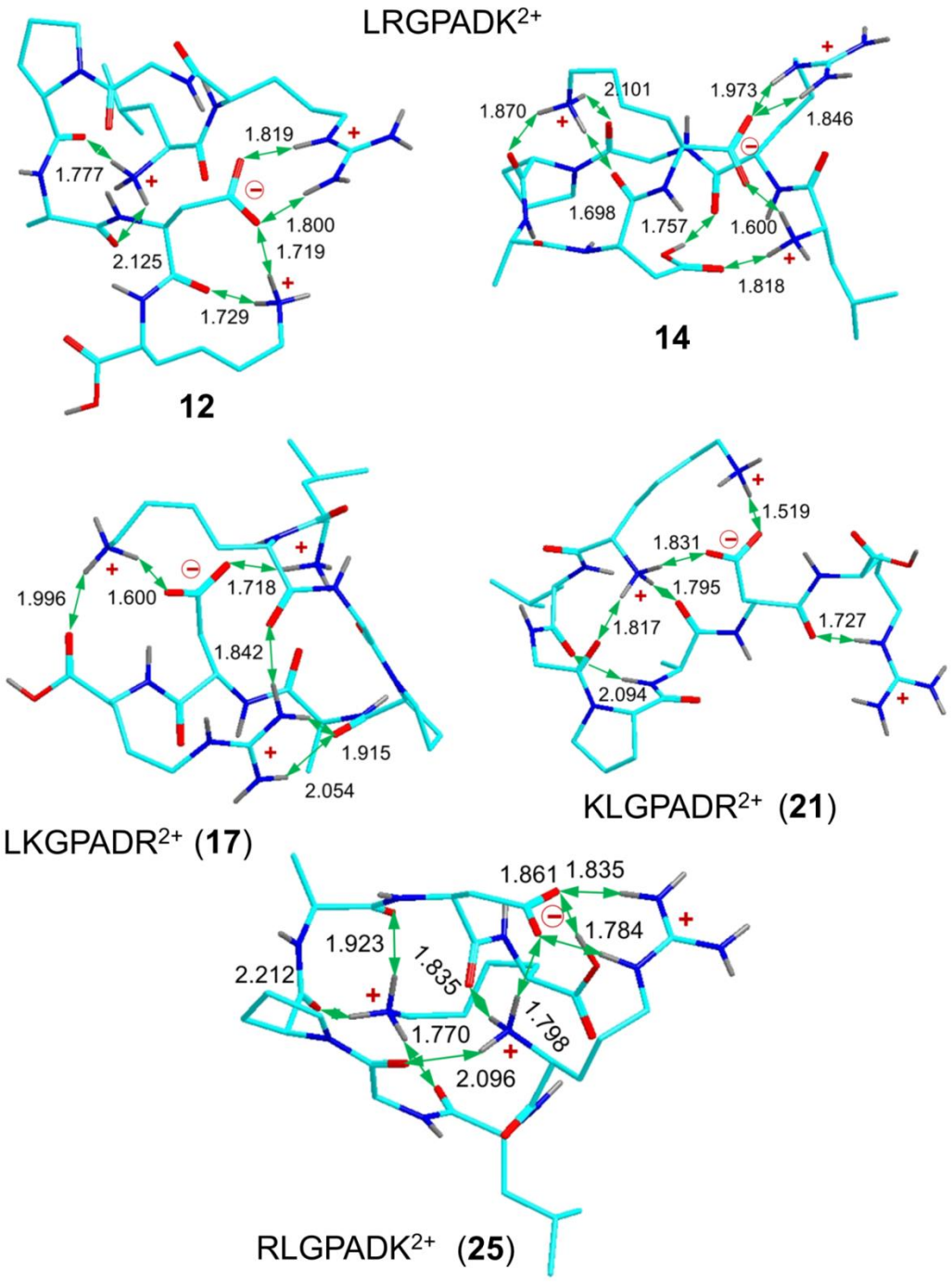

Figure 20: B3LYP/6-31+G(d,p) optimized structures of lowest-free energy conformers of representative doubly charged ions. Structure description as in Figure 2.

Swapping the Leu and Lys residues in LKGPADR formed $KLGPADR^{2+}$ ions. Upon molecular dynamics and full geometry optimization, a number of Asp-zwitterionic structures converged to a family of lowest free-energy conformers **21**-**24** whose folding pattern is represented by **21** (Figure 5). Conformer **21** had the Asp carboxylate internally solvated by H-bonds to the Lys and *N*-terminal ammonium groups. The charged Arg group was remote from the carboxylate, but cooperatively interacted by forming a strong H-bond to the Asp carbonyl. This interaction polarized the Asp amide N-H bond to strengthen the H-bond to the Asp carboxylate. A salient feature of these ions was that the Lys charged group formed only a single H-bond whereas the protons of the *N*-terminal ammonium were fully internally solvated by the Lys and Gly amides in addition to the Asp carboxylate

The lowest free-energy conformers of the last sequence, $RLGPADK^{2+}$, were found to prefer a folding pattern which is represented by conformer **25** (Figure 5). This Asp-zwitterion had the carboxylate internally solvated by the charged Arg and *N*-terminal ammonium groups and the neutral C-terminal carboxyl. All three protons of the Lys ε-ammonium were internally solvated by forming H bonds to the Pro, Gly, and Leu amide carbonyls.

3.3.3. Fragmentations

3.3.3.1. ETD-MS^2 Spectra Owing to the presence of two highly basic residues in all peptide sequences considered, it is not surprising that in all cases the nearly complete **c** and $\mathbf{z}^{\cdot}$ ion sequences were observed for all peptide ions with relative fragment ion abundances varying based on the sequences of the ions in question. Figure 6(a) shows the ETD spectrum resulting from triply protonated LKGPADR reacting with the fluoranthene reagent.

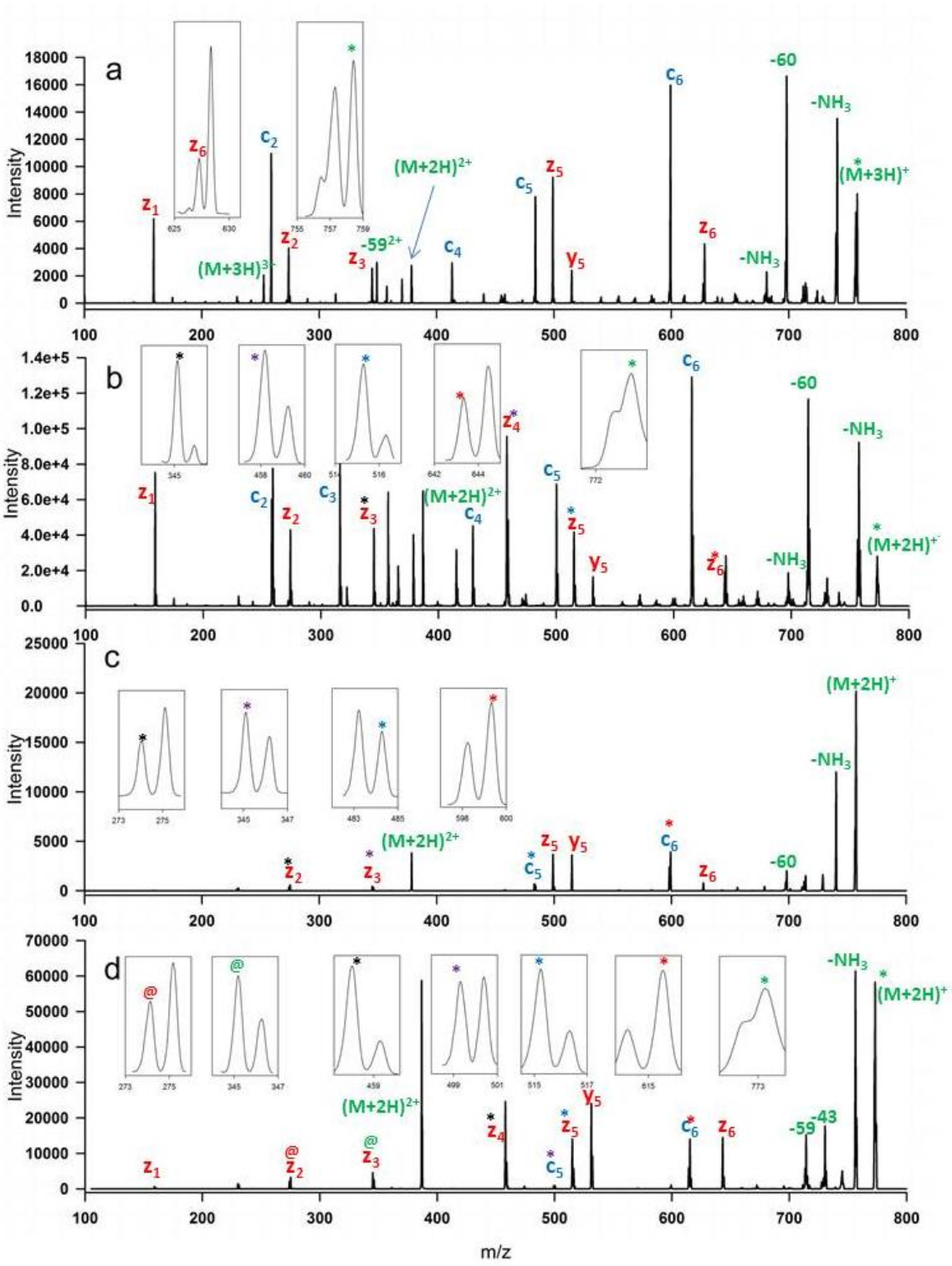

Figure 21: (a) ETD of triply charge LKGPADR 300ms; (b) ETD of triply charged LKGLADR 200ms; (c) ETD of doubly charged LKGPADR 300ms; (d) ETD of doubly charged LKGLADR 200ms. All precursor ions were mass isolated to exclude isotopologues. Symbols above sequence ion annotations indicate the insets to which they correspond.

The ETD behavior of LKGPADR is a typical example of how the proline centered peptides behaved. Reduction upon electron addition results in an array of doubly and singly charged fragment ions. The full C-terminal ***z***-ion sequence is observed, with the exception of $\boldsymbol{z_4}^{\bullet}$ as expected due to the presence of the proline residue. The N-terminal c-ions are lacking the $\boldsymbol{c_3}$ ion as expected, again due to the proline effect, and $\boldsymbol{c_1}$: a species that is not likely to out compete the highly basic complementary $\boldsymbol{z_6}^{\bullet}$ fragment for a charge. The spectrum also shows various common radical initiated neutral losses[22] loss of ammonia (*m/z* 741.4 and *m/z* 681.4), loss of 60 from the arginine guanidinium group or the aspartic acid side chain (*m/z* 698.4), loss of 43, C_3H_7, from the leucine side chain (*m/z* 715.4, *m/z* 655.3, and doubly charged *m/z* 357.7), and loss of 59 from the arginine guanidinium group (*m/z* 100.1 and doubly charged *m/z* 349.3). Noteworthy is the content displayed in the two insets. The $\boldsymbol{z_6}^{\bullet}$ ion shows a strong tendency to abstract an additional proton from the complementary fragment resulting in a $\boldsymbol{z_6}^{\bullet}$ +1 peak that far exceeds what would be expected from isotopic contributions. The inset around the doubly charge reduced ion cluster shows the presence of an interesting phenomenon. The $(M+H)^+$ and $(M+2H)^{+\bullet}$ show an overlap and an apparent mass shift that indicates the possible presence of metastable fragments.

Figure 6(b) shows the ETD spectrum from triply charged LKGLADR which is also a good prototype for the leucine centered sequences. It shows many similarities to the spectrum for LKGPADR in Figure 6(a). There is a full ***z***-ion sequence present. From the ***c***-ion sequence only a $\boldsymbol{c_1}$ fragment is missing. A similar array of common radical initiated neutral losses is evident: loss of ammonia (*m/z* 757.5, 697.4, and doubly charged 378.7), loss of 60 (*m/z* 714.5 and doubly charged 357.3), and loss of 43 (*m/z* 730.5, 415 and doubly charged 365.8). The $(M+H)^+$ and $(M+2H)^{+\bullet}$ again show an overlap in the ion peaks as well as a mass shift indicating that the

metastability observed in Figure 6(a) is not an isolated occurrence. Noteworthy differences between Figure 6(a) and 6(b)b include the proportion of backbone fragments which show the hydrogen transfer reaction occurring. The leucine centered sequence in Figure 6(b) shows more sequence ions exhibiting this hydrogen atom transfer (7 versus 3) and a greater amount of the total sequence ion signal (13% versus 6%) is due to hydrogen shifted fragments. The other noteworthy point of difference between the two spectra is the complete lack of a $(M+3H)^{+}$ product ion in the leucine centered peptide shown in Figure 6(b).

When considering the ETD spectra of doubly charged ions created from the electrospray, as shown in Figures 6(c) and 6(d), one notices differences and similarities. As expected there are fewer sequence fragments present and fewer radical induced neutral losses. However, there is still a noticeable trend of hydrogen transfer reactions between sequence ions. The metastable ions are still present in the charge-reduced cluster of ions as well. The ETD spectrum of doubly charged LKGPADR shows an increase in the amount of hydrogen transfer products contributing to the total sequence ion signal (25% in the doubly charged from 6% in the triply charged) while the ETD spectrum of doubly charged LKGLADR shows a decrease in the amount of hydrogen transfer products contributing to the sequence ion signal (6.5% in the doubly charged from 13% in the triply charged).

3.3.3.2 ETD-CID-MS^3 Spectra In order to more fully understand the chemistries involved in the ETD charge reduction of these peptide ions, the charge reduced cation radicals $(M+2H)^{+\bullet}$ were subjected to collisional activation in an MS^3 step. Figure 7 shows some sample result spectra from these experiments. Figure 7(a) shows CID of the $(M+2H)^{+\bullet}$ from LKGLADR. This shows a behavior unique amongst the peptides in this study's library. The charge-reduced $(M+2H)^{+\bullet}$ either loses a hydrogen atom to form $(M+H)^{+}$ or breaks apart into hydrogen shifted ***c***

and $\boldsymbol{z}^{\cdot}$ ions. This spectrum is extraordinarily clean, no fragments other than the loss of hydrogen and the sequence ions are present. This indicates that the $(M+2H)^{+\cdot}$ peak in the ETD spectrum likely represents non-dissociated ion-molecule complexes rather than intact charge reduced peptides. Figure 7(b) shows the CID of $(M+2H)^{+\cdot}$ from ETD of KLGPADR. The two most abundant product ions present represent radical type losses and are accompanied by minor amounts of ***b*** and ***y*** sequence ions. Losses of neutral radical $C_3H_7^{\cdot}$ and neutral $C_3H_8N^{\cdot}$ radical show a largely radical-driven dissociation with some competition from charge-driven dissociations.

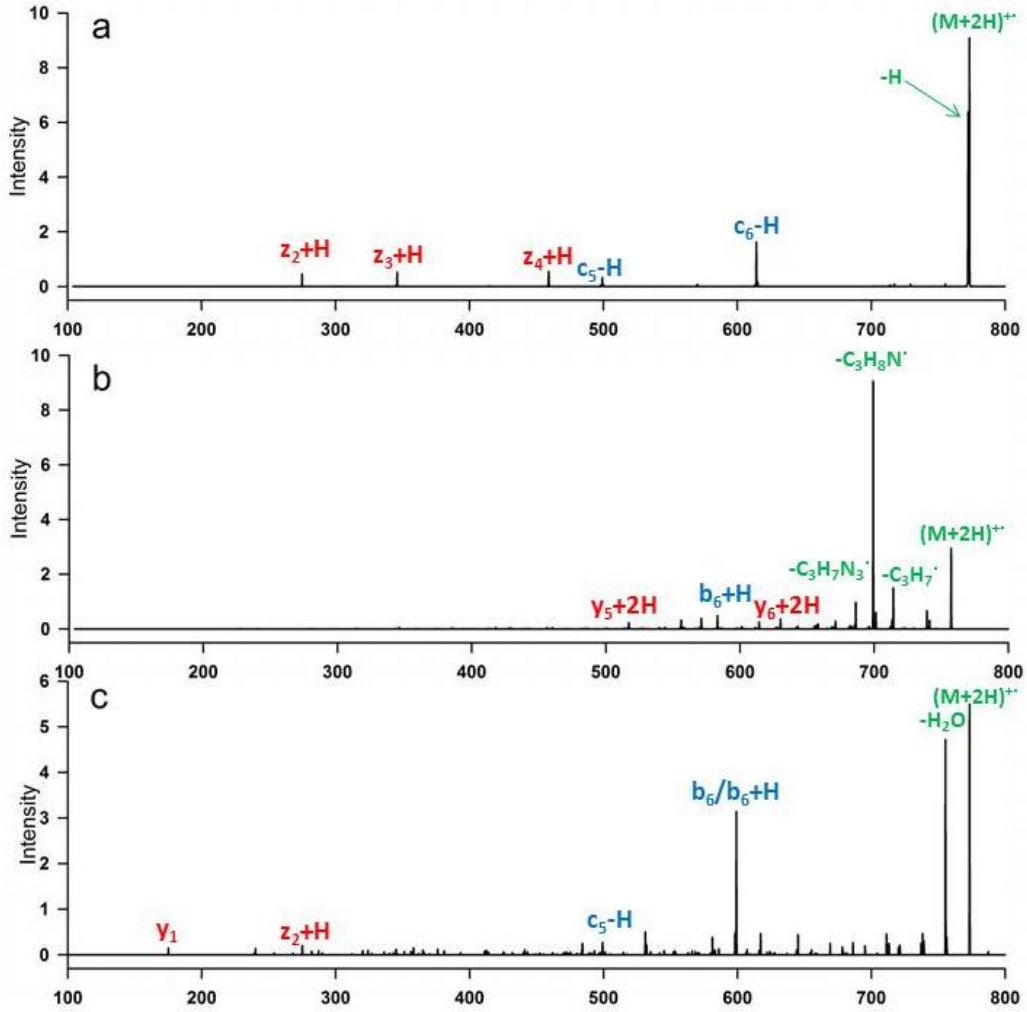

Figure 22: MS3 Spectra, ETD of the doubly charged ion followed by CID of the (M+2H)+ product ion. (a) LKGLADR; (b) KLGPADR; (c) KLGLADR.

Figure 7(c) shows CID of $(M+2H)^{+\bullet}$ from KLGLADR. Other than a peak representing the loss of water from the precursor, the most prominent product peak is the $\boldsymbol{b_6}$ sequence ion. There are no peaks identifiable as being due to radical losses indicating that this $(M+2H)^{+\bullet}$ fragments in a primarily charge driven manner. Figure 7 contains examples of all three types of $(M+2H)^{+\bullet}$ fragmentations observed in the CID MS^3 spectra. The breakup of ion complexes shown in 7(a) is unique to that particular species and is not seen in any other peptide in this study. The breakdown of each particular peptide's behavior is shown in Table 5.

	Radical Driven	Charge Driven	Complex Dissociation
LKGPADR	√		
KLGPADR	√		
RLGPADK	√		
LRGPADK	√		
LKGLADR			√
KLGLADR		√	
RLGLADK		√	
LRGLADK		√	

Table 9: Summary of types of fragmentation observed upon CID activation of $(M+2H)^{+\bullet}$

3.3.3.3 ETD-UVPD-MS^3 fragmentations Radical cations generated via ETD experiments have been shown to be chromophores for 355nm photons.[23] As a comparison to the fragmentations observed from ETD-CID MS^3 experiments, ETD-UVPD MS^3 experiments were run as well on selected peptide ions. The $\boldsymbol{z_3^{\bullet}}$, $\boldsymbol{z_5^{\bullet}}$, $\boldsymbol{z_6^{\bullet}}$, $\boldsymbol{z_7^{\bullet}}$ and $(M+2H)^{+\bullet}$ from RLGPADK and the $\boldsymbol{z_3^{\bullet}}$, $\boldsymbol{z_5^{\bullet}}$, $\boldsymbol{z_7^{\bullet}}$, $(\boldsymbol{z_7^{\bullet}})^{2+}$, $(M+2H)^{+\bullet}$ and $(M+3H)^{+}$ from LRGPADK were selected for UVPD activation. Examples of these UVPD spectra are shown in Figure 8 in a side-by-side comparison with CID activation of the same ions. It should be noted here that $\boldsymbol{z_6^{\bullet}}$ from LRGPADK is isobaric with $\boldsymbol{c_6}$ and that under high resolution ETD was shown to be approximately 10:1 relative abundance $\boldsymbol{c_6}$ to $\boldsymbol{z_6^{\bullet}}$ and wasn't able to be isolated for MS^3 activation. As indicated by asterisks in Figure 8, UVPD

generated several unique fragments not seen at all in CID activation.

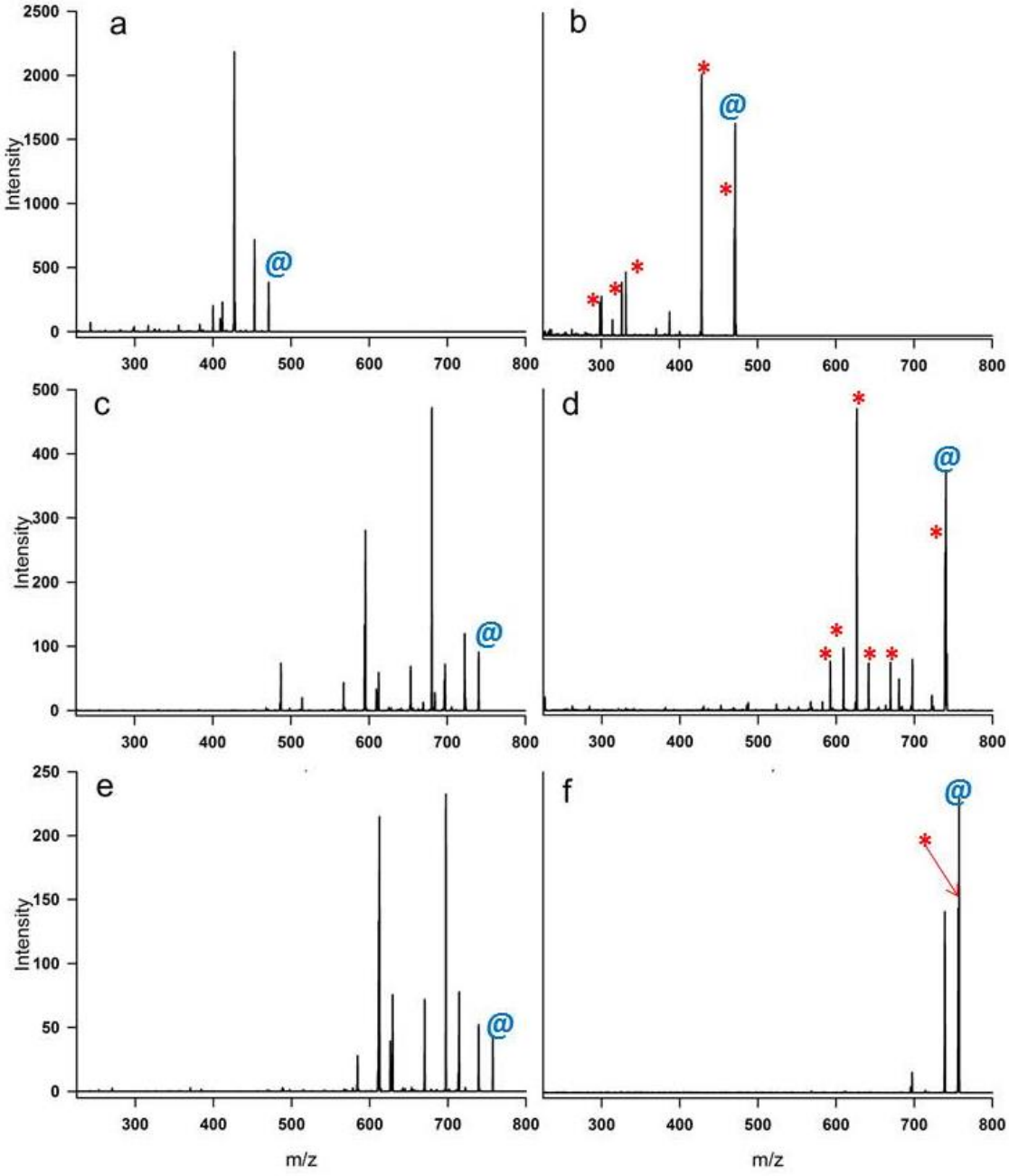

Figure 23: MS^3 Activation of some cation radical ETD fragment ions. (a) CID of z_5, (b) UVPD of z_5 with 6 laser pulses, (c) CID of z_7, (d) UVPD z_7 with 4 laser pulses, (e) CID of (M+2H)+, (f) UVPD of (M+2H)+ with 9 laser pulses. Red asterisks indicate fragments unique to UVPD activation and blue @ represent the surviving parent ion.

As shown in Table 6, the most commonly observed unique photolysis fragment was loss of hydrogen, but there were several other unique fragments as well, depending on the particular ion.

The implications for the differences in behavior between UVPD and CID activations of these ions are discussed below.

	RLGPADK	LRGPADK
z3	-COOH	none
z5	-84, y_3-2H, -145, -157, -171, -173	-H, -43, -140, -145, -171, -173
z6	-H, -99, -116, y3-2H	
z7	-H, -35, -88	-H, -71, -99, z6-H, -131, -148
(z7)2+		-72, -190, -228, -313, $(y_6\text{-}2H)^{2+}$, -114/2, -158/2
(M+2H)+	-H, -62	-H
(M+3H)+		-H

Table 10: List of unique photo induced fragments from photolysis at 355nm of heptapeptide ETD fragments.

3.4. Discussion

3.4.1. Relative Energies of Sequence Isomers The conformer relative energies can be related to the combination of major non-covalent electrostatic interactions in the ions that can be expressed as a sum of attractive ion-dipole ($E_{id} < 0$) and repulsive pair-wise Coulomb ($E_c > 0$) interactions of the charged groups. The calculated DFT relative energies include contributions from all these interactions and thus allow one to gauge the relative ion-dipole interactions in a semiquantitative manner and relate them to the major structure features in the optimized structures. The pairwise Coulomb energies were estimated from the standard formula, $E_c(\text{kJ mol}^{-1}) = \Sigma 1389.38/R_{ij}$, where the distance between the charged groups *i* and *j* was measured from the central atoms (N for ammonium and C for guanidinium). For example, the thus estimated Coulomb energy in **1** (362 kJ mol^{-1}) was 15 kJ mol^{-1} higher than that in **2** (347 kJ mol^{-1}), yet the former conformer was 10-14 kJ mol^{-1} more stable. This implied that the attractive ion-dipole interactions contributed to ca. 25-30 kJ mol^{-1} greater stabilization in **1** compared to those in **2**. The optimized ion structures (Figure 2) indeed showed slightly tighter H-bonds of the charged groups in **1** compared to those in **2**.

With KLGPADR^{3+} ions, the charged groups in conformers **3** and **4** had relatively high Coulomb energy (480 and 498 kJ mol^{-1}, respectively) compared to that in **5** (469 kJ mol^{-1}). This is in part reflected by the B3LYP and ωB97XD relative energies that placed **5** as the lowest energy conformer, whereas M06-2X placed it above **3** and **4** (Table 2). Note that conformers **3** and **4** had quite different hydrogen bonding patterns than **5** so that their different ion-dipole interactions could not be readily assigned to the strength of particular hydrogen bonds.

Amongst the RLGPADK^{3+} conformers, the lowest energy structure **8** showed the highest Coulomb repulsion energy (565 kJ mol^{-1}), underscoring the dominant effect of ion-dipole stabilization of the ion. Structures **6** and **10** which had notably lower Coulomb energies (498 and 488 kJ mol^{-1}, respectively) were less stable than **8**. Hence, the DFT energy data indicate that considering the Coulomb energy alone may be unreliable for assessing ion conformer relative stabilities, and a careful analysis of all interactions, preferably through electron structure calculations, is recommended.

3.4.2. Correlation between the calculated and ion mobility collision cross sections The energy calculations identified the lowest free-energy conformers for the gas-phase peptide ions. We now compare the collision cross sections that were calculated for the lowest free-energy conformers (Ω_{th}) to the experimental data (Ω_{abs}). The calculations were based on both B3LYP and M06-2X fully optimized structures that showed minor variations in bond lengths, angles and dihedral angles for each ion conformer. Collision cross section calculations were run with three different models which were (a) the projection average approximation (PA), elastic -hard-sphere scattering (EHSS), and ion trajectory model (ITM) which is also available with a modified set of parameters.[15–17] In general, these models give different Ω_{th} for the same geometry and charge distribution in the peptide ion. Hence, the conversion into Ω_{th} of the ab initio or DFT-

calculated molecular parameters is somewhat ambiguous, which is further underscored by small differences in the optimized ion geometries generated by different density functionals. On the basis of our previous studies of peptide ion conformers,[14] we considered all combinations of B3LYP and M06-2X structures with PA, EHSS and ITM methods. To evaluate the overall accuracy of the calculated data, we show in Tables 2 and 3 the smallest deviations of the calculated Ω_{th} from the Ω_{abs} and Ω_{cal}.

Regarding the doubly charged ions, the LRGPADK^{2+} conformers showed very good agreement between the experimental Ω_{abs} and Ω_{cal}, and the Ω_{th} for the lowest-energy conformers **12** and **16** (Table 3). Both the B3LYP and M06-2X optimized structures gave closely matching Ω_{th} that were selected from the PA, EHSS and ITM calculated values. However, close match with the Ω_{th} was also obtained for higher-energy conformers **13**-**15** which would not be expected to be significantly populated in a conformer mixture at thermal equilibrium. Hence, the closest match between the Ω_{abs} and Ω_{th} is insufficient to provide the basis for unambiguous structure assignment. A very good match was also obtained for LKGPADR^{2+} and RLGPADK^{2+} where the Ω_{abs} and Ω_{th} were within 1% for the low-energy conformers and the best-matching PA, EHSS and ITM calculated values. The calculated relative free energies for the thermodynamically most stable LKGPADR^{2+} and RLGPADK^{2+} conformers are very similar, indicating that peptide ions with these sequences may exist in equilibrium mixtures that are not resolved by ion mobility measurements. The Ω_{th} for KLGPADR^{2+} showed less satisfactory agreement with Ω_{abs} and Ω_{cal} (3.5%) when based on B3LYP optimized structures, although still within the expected combined accuracy of the computational methods.

The triply charged ions showed different degrees of agreement between the Ω_{th}, Ω_{abs}

and Ω_{cal} (Table 2). The Ω_{th} for the low free-energy LKGPADR^{3+} conformers showed an excellent match with the Ω_{abs}, in particular for the B3LYP optimized structures (<1%). In contrast, the Ω_{th} for all low free-energy KLGPADR^{3+} and RLGPADK^{3+} conformers showed <3% agreement with pertinent Ω_{abs} only when based on EHSS model calculations whereas the other models gave substantially lower values. Since in our experience EHSS often overestimates the Ω_{th}, the match between the calculated and experimental data can be judged unsatisfactory. The reason for this discrepancy is not obvious because the structures, energies, and Ω_{th} for all these peptide ions were treated at the same level of theory. It is possible that the KLGPADR^{3+} and RLGPADK^{3+} ions produced by electrospray assume higher free-energy, more expanded, conformations as a result of being frozen in non-equilibrium populations upon transition to the gas phase.

Replacing the Pro residue with Leu had only a very small effect on the collision cross sections of all doubly and triply charged ions (Table 1). We addressed this topic with the RLGPADK^{3+} system for which we obtained optimized ion structures **8** and its Leu homologue **8**-Leu (not shown). The structures illustrated that there were only minor changes in the backbone and charged-group conformation upon replacing Pro with Leu, as evidenced by the nearly identical H-bonds of the Lys side chain and *N*-terminal ammonium groups, and the Arg guanidinium group. These charge-solvating interactions together with the strong H-bonding of the Asp carboxyl to the Leu-2 amide were the major factors defining the ion overall conformation and collision cross section. The calculated Ω_{th} for **8** and **8**-Leu showed 4.4-5.5% increase upon replacing Pro with Leu to be compared with a 2.5% increase when based on the Ω_{cal}. Given the combined uncertainties in both types of values, this represents an acceptable agreement.

3.4.3. Fragmentations

3.4.3.1. Metastability fractions The presence of metastable fractions in the charge reduced ion clusters in each heptapeptide sequence were investigated in detail. It was assumed that $(M+H)^+$ and $(M+2H)^{+\cdot}$ were both present at correct *m/z* values. A fitting routine which fit Gaussian shaped distributions to the spectra was then applied in the following manner. A Gaussian distribution has three parameters which are necessary to describe it completely: location of the center of the distribution, the width of the distribution about that center and the height of the distribution at the peak. The width of the distributions were set to be the same width as that of the $(M+3H)^+$ peak above the overlapping peaks or the width of the loss of ammonia peaks in the case of the leucine centered peptides which did not form $(M+3H)^+$. The locations of the centers were chosen to be consistent with the other fragments present; a choice which was further supported by the fact that mass isolation at that location yielded products with the correct mass defect. This left only the heights of the distribution as fitting parameters. Upon fitting by a least squares method, the residual counts that were not part of the two fitted Gaussians were taken to be the fraction of metastable ions measured. This was accomplished for each peptide sequence in the study and examined for trends.

The scan rate of the LTQ XL ion trap was slowed down,[24] using the ZoomScan mode, to increase the resolution in an attempt to better resolve the $(M+H)^+$ and $(M+2H)^+$ ions. These ions were not resolved in this manner and it was found that the scanning speed of the trap did have an effect on the observed metastable contribution.

A comparison between analogous peptides (those sequences which differed only in the identity of the fourth residue, proline vs leucine), as shown in Table 7, revealed that in nearly all cases,

the leucine centered peptides gave rise to a higher metastable contribution than did the proline centered peptides.

P vs L Species	P % Meta	L % Meta	P Meta Shift	L Meta Shift
LKG(P,L)ADR3+	69	86	0.25	0.33
LKG(P,L)ADR3+z	74	96	0.18	0.25
LKG(P,L)ADR2+	57	62	0.33	0.56
LKG(P,L)ADR2+z	65	56	0.16	0.26
KLG(P,L)ADR3+	67	95	0.25	0.50
KLG(P,L)ADR3+z	77	98	0.18	0.36
KLG(P,L)ADR2+	72	93	0.36	0.41
KLG(P,L)ADR2+z	62	98	0.24	0.30
RLG(P,L)ADK3+	60	80	0.23	0.46
RLG(P,L)ADK3+ Z	74	86	0.10	0.30
RLG(P,L)ADK2+	64	79	0.15	0.36
RLG(P,L)ADK2+ Z	69	86	0.10	0.38
LRG(P,L)ADK 3+	69	95	0.26	0.46
LRG(P,L)ADK 3+z	83	69	0.10	0.39
LRG(P,L)ADK 2+	61	64	0.25	0.50
LRG(P,L)ADK 2+z	71	99	0.10	0.35

Table 11: Percentages of combined (M+H)+ and (M+2H)+ signal which were due to metastable ion counts. Right hand column shows the amount of the shift of the apparent center of (M+H)+ by the metastable contribution (units are Da). The two highlighted entries show the two examples where Proline containing peptides had higher metastable contributions. "z" indicates percentages derived from ZoomScan mode.

The presence of the metastable fraction overlapping the masses of the stable charge reduced product ions resulted in an apparent mass shift of the distribution from the expected *m/z* values. In all cases the apparent mass shift in the leucine centered peptides due to the presence of the metastable fraction was greater than or equal to the mass shift observed in the proline centered peptides. The LTQ instrument uses a mass selective instability with resonant ejection scheme to radially eject the ions from the trap into the detector at a q value of 0.88.[24] As the ions are resonantly excited prior to ejection, the metastable bond(s) gains enough energy from the excitation process to dissociate, and as shown in Chapter 1, the stability parameters are inversely proportional to the mass-to-charge ratio. At this point the now smaller ion's q value suddenly

changes to a larger value, comes into resonance, and is subsequently ejected from the trap early. Equations describing this event are shown below.

$$\frac{KE}{m} = \frac{1}{2}\omega^2 r^2 \quad \textbf{(4)}$$

$$\omega = \frac{1}{2}\beta\Omega \quad \textbf{(5)}$$

$$E_{cm} = \frac{m_{He}}{m_{ion} + m_{He}} E_{lab} \quad \textbf{(6)}$$

Equation (1) describes the lab frame kinetic energy per mass unit of the ions in the trap as a function of the characteristic frequency of the ions and the radius of motion r = 4mm. Equation (2) describes the characteristic frequency of the ions in the trap as a function of the trapping RF (Ω = 1.2MHz) and the ion's β value (~0.7 at a q of 0.88). Equation (3) converts the lab frame kinetic energy into the center of mass frame. The given parameters lead to a KE/mass of 0.015 eV/Da and therefore an E_{lab} of 11.4 eV at 757 Da (proline centered) and a E_{lab} of 11.6 eV at 773 Da(leucine centered). This leads to E_{cm} values of 0.0599 eV and 0.0597 eV respectively. The ions are stored at q value of 0.3 giving rise to a β value of 0.1. By the same analysis as shown at the point of ejection, E_{cm} values during storage are 0.034 eV and 0.032 eV respectively. This increase of 0.0259 eV and 0.0277 eV shows the fragility of the metastable bond. Using the normal LTQ scan rate of 16,666 u/sec, ions making up the metastable fraction then are ejected anywhere from 6 µs to 42 µs early. The propensity for this to happen shows a clear division between the peptides with proline in the fourth position and those peptides with leucine in the fourth position. The leucine centered peptides are ejected earlier from the trap than the proline centered set and to a greater extent. It is our belief that the proline ring provides a stabilizing effect to the radical in the $(M+2H)^{+\cdot}$ in a manner similar to histidine[11,12] containing species leading to a decrease in the observed metastable behavior.

3.4.3.2. Presence/lack of charge reduced ions Upon examination of all of the ETD spectra of triply charged ions produced in this study it becomes quickly apparent that the peptides which contain leucine in the fourth position have a similar lack of $(M+3H)^+$ product ion as to that observed for the LKGLADR peptide shown in Figure 1(b) and mentioned above. There appears to be no pathway for the addition of two electrons to the triply charged precursor which will allow retention of all 3 charging protons. Examination of the ETD spectra from triply charged peptides which contained proline in the fourth position show the presence of an abundant $(M+3H)^+$ product ion. As in the case of the metastabilities of these ions discussed above we ascribe this difference to the presence of the proline ring structure. In the case of the metastability we believe that the ring structure allowed the radical ion to be more stable. We believe that an N-Cα bond cleavage does take place at the location of the proline residue, but owing to the ring structure, this does not result in the decomposition of the ion. Possible rearrangements of the charge reduced proline containing peptides can apparently lead to a stable $(M+3H)^+$ ions.

3.4.3.3. Hydrogen transfer reactions The hydrogen transfer reactions following ETD were evaluated as a function of each individual peptide sequence(Examples for one sequence shown in Figure 6). Reactions leading to the (***c***-H) and (***z***+H) likely occur following backbone cleavage of the peptide while the fragments are part of a complex and prior to the complex dissociation. The heptapeptides in this study were designed in such a way so that they would have a compact shape in the gas phase. Two basic residues should be attracted to the two acidic sites pulling the peptide in towards itself. It is likely that the actual shape in the gas phase would determine the extent to which H transfer reactions between ETD fragments is likely to occur. The more compact and tightly bound a peptide species is to itself the more energy is going to be needed to

dissociate the complex. The higher energy barrier to dissociation in the various peptide sequences will translate to longer times that the fragments in the complex will be able to interact with each other and potentially pass labile hydrogen atoms between themselves. The total amount of sequence ion signal which is due to hydrogen shifted fragments was evaluated and expressed as a percentage. A comparison between ETD of the triply charged peptide and doubly charged peptide showed that with the exception of the LKGLADR sequence all other sequences showed an increase in the amount of hydrogen shifted fragments present in the doubly charged ions (Table 8).

	$(M+3H)^{3+}$		$(M+2H)^{2+}$	
Peptide	L	P	L	P
KLGL(P)ADR	4.79	0.31	14.62	22.66
LKGL(P)ADR	12.99	5.98	6.47	25.16
LRGL(P)ADK	1.87	0.59	5.61	5.54
RLGL(P)ADK	0	0	1.35	0.96

Table 12: Percentage of combined sequence ion signal which is due to hydrogen shifted sequence ions

This is likely due to the doubly charged ions being zwitterionic. The highly basic lysine and arginine residues as well as the N-terminus gain a proton during the electrospray ionization process but then lose a proton from one of the acidic sites. This negative site attracts the positively charged sites so that upon electron transfer and subsequent backbone dissociations the complex is much more tightly bound than in the case of the triply charged ions thereby allowing more hydrogen transfer reactions to occur. The conformation of the LKGLADR sequence likely does not follow this general rule.

When comparisons are made between pairs of analogous peptide sequences in which the only difference between the sequences is the identity of the fourth residue the results are not as straightforward. For the triply charged peptides, the leucine centered sequences all show a greater amount of hydrogen transfer than their proline analogs. This could be explained by the increased rigidity of the peptide structure granted by the ring structure of the proline. The

leucine centered sequences have more freedom of motion and therefore can adopt conformations more amenable to hydrogen transfer. The doubly charged proline centered sequences show an increase, or an essentially even amount of hydrogen transfer activity over the leucine centered sequences.

3.4.3.4. ETD-UVPD-MS^3 Fragmentations The presence of fragments unique to UVPD activation of ETD product ions is quite interesting. A conceptual diagram of the energetics of peptide ion fragmentations is shown in Figure 10. Ions which are stored in the ion trap become thermalized after a short residence time and have a narrow energy distribution, shown as the black trace in Figure 10. Upon collisional activation, these ions receive additional energy in the form of vibrational energy which is distributed throughout the various vibrational modes of the ion. This will result in a much broader distribution of energies ranging from ions which are still at the thermal energies up to ions which are on the verge of dissociating into products, shown as the green trace. Collisional activation occurs on a ground electronic state as the energy is transferred into vibrational modes.

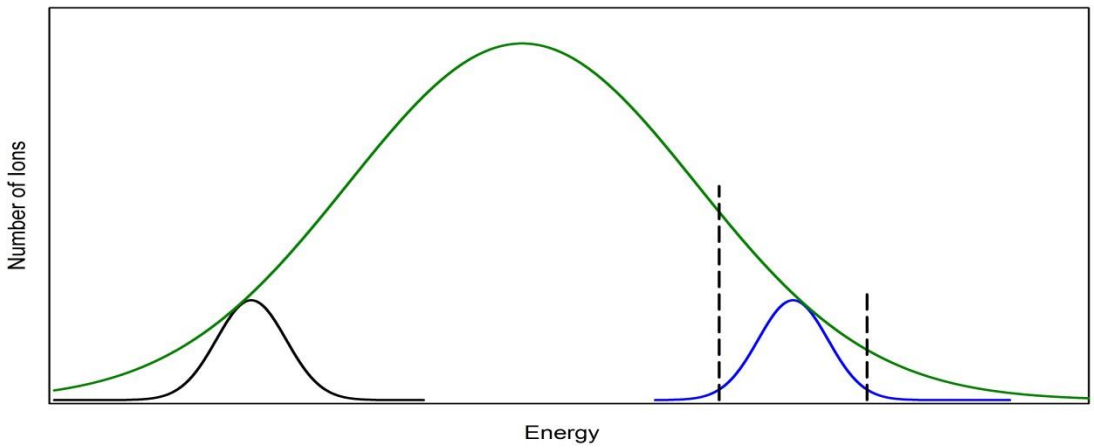

Figure 24: Conceptual energy distribution diagram

Upon photo activation, the energy of the thermalized ions stored in the trap will either jump up by exactly the amount of energy of the photon or not change at all due to no photons being

absorbed. This results in essentially no broadening of the energy distribution, just a movement of the center as shown in the blue trace. Assuming that ions with energies in the range shown by the vertical dashed lines are on the same energy surface they should have the same dissociation products whether they got there suddenly, via a photon(blue), or gradually, during collisional slow heating(green). It is expected that there would be a different distribution of the product ions since there is a difference in how the energies are distributed between the two different activation modes, but the identities should be the same. What is seen in Figure 8 and Table 6 is that there are dissociation channels which are completely unique to the photo activation mode. This means that the ions from the collisional slow heating activation and the ions from the fast photon absorption activation method must be on separate energy surfaces; that is, the ions fragmenting via photons must be coming from an excited electronic state. It is also worth noting that the fragmentation spectra generated via collisions also have some unique fragments not seen in the corresponding photo fragmentation spectrum. This would seem to indicate that some fragmentation channels are only accessible from the ground electronic state or that many of the collisional fragments are the result of activation of the unpaired electron as many of the photo fragments must have carried the radical away as part of a neutral loss.

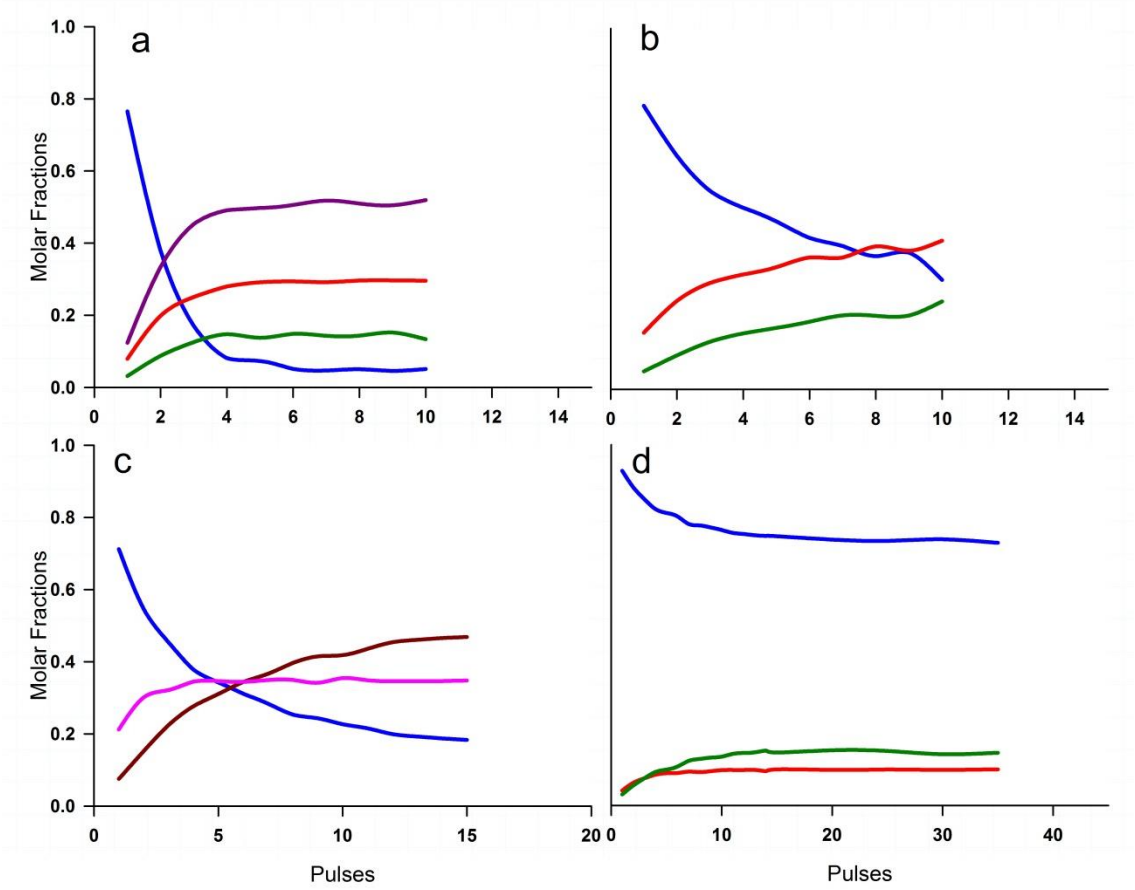

Figure 25: Pulse Dependent Photolysis of selected ETD product ions. (a) Photolysis of the z_5 ion from RLGPADK 3+. Blue: Surviving z_5 ion, Green: product ion *m/z* 326, Red: product ion *m/z* 331, Purple: z_5 - 43 product ion. (b) Photolysis of (M+2H)+ from ETD of RLGAPDK 3+ Blue: Surviving (M+2H)+ ion, Red: Loss of H, Green: Loss of water. (c) Photolysis of z_7 from ETD of LRGPADK 3+ Blue: Surviving z_7 ion, Brown: Loss of H, Pink: Product ion *m/z* 626. (d) Photolysis of (M+3H)+ from ETD of LRGPADK 3+ Blue: Surviving (M+3H)+, Red: Loss of H, Green Loss of H2O.

Monitoring the photo induced dissociation of ETD product ions as a function of the number of applied laser pulses provided some interesting information. Consider the examples presented in Figure 11 above. Part (a) shows the photolysis of $\boldsymbol{z_5}^{\cdot}$ from the ETD of triply charged RLGPADK. Major product ions were loss of 43 (possibly elimination of the remaining portion of the glycine residue) shown in purple, formation of the $\boldsymbol{y_3}$-2H sequence fragment shown in red and product ion *m/z* 326 (a neutral loss of 145 mass units possibly corresponding a cascade dissociation fragment) shown in green. This example is atypical in that it didn't show a loss of hydrogen atom. This data shows a flattening of the depletion curve after approximately 7 pulses

indicating that some proportion of the precursor ion was a non-absorbing isomer initially or it was photo isomerized to a non-dissociating structure.

Part (b) shows a more typical result where hydrogen atom loss is the most abundant photo induced product ion from $(RLGPADK+2H)^{+\bullet}$ and the surviving ions come to a level again indicating a nondissociating fraction. Part c shows the photo dissociation of $\boldsymbol{z_7}^{\bullet}$ ETD product ion from LRGPADK. Again, loss of hydrogen atom is the dominant photo induced product channel followed by formation of the $\boldsymbol{z_6}$ -H product ion. Part D shows an unexpected result. This is photolysis of the doubly charge reduced intact product ion (LRGPADK+3H)+ from ETD clearly showing about 25% depletion of the precursor. It is to be expected that with the addition of two electrons to the triply charged precursor that the resultant ion would have the added electrons paired in an orbital as a double radical species would like be unstable. This clearly wasn't the case for some of the ions in this example. Further testing of the photo product ions could possibly confirm the radical containing nature of these product ions. Unfortunately, there was insufficient MS^3 product ion intensity to be able to perform MS^4 analysis.

3.5. Conclusions

Heptapeptide structures in the gas phase are difficult to model computationally. Following an extensive computational routine for low energy conformer elucidation we can conclude that ion mobility measurements alone are insufficient for assigning which computational structures are correct. The computationally derived structures produce CCS values less than 3% apart and as such cannot be discriminated between in preference for one over the others.[25] An additional method such as infrared multi photon dissociation may add sufficient discriminatory power as to resolve the correct structures.[14] Although, due to collisions within the ion trap, it is likely that the thermal ions can adopt a number of conformations and there might not be one "correct"

answer. Fragmentations of heptapeptide ions studied in this chapter showed interesting results. Evidence of the successful design of the heptapeptide library is demonstrated by the extensive evidence of hydrogen shifted ETD sequence fragments; tightly bound ion-molecule complexes following backbone cleavage lead to more hydrogen transfer activity than in less tightly bound complexes. ETD of heptapeptide sequences which differed only in the amino acid order created different types of charge reduced ions upon electron transfer showing that sequence order can have a strong effect on the electronic structure of peptide ions. Proline has a unique effect when placed in the peptide ion's sequence. Activation of intact proline containing charge reduced peptide cation radicals showed radical driven cleavages while the heptapeptides which did not contain proline showed primarily charge driven fragmentations indicating proline's ability to stabilize radicals. It creates a structure which can hold on to all three charging protons after double reduction while the non -proline containing ions could not. It causes an increase in the stability of metastable charge reduced ions as shown by the decreased metastable fraction of ions present in the ETD relative to non -proline containing ions. Finally, photo activation of ETD produced radical peptide ions shows that dissociations can occur directly from excited electronic states as fragments unique to photo activation are shown to occur. Pulse dependent monitoring of UVPD shows that there are populations of ions which are either isomerized to non-dissociating structures or which are non-absorbing.

3.6. Acknowledgements

Thanks and gratitude are due to Carlos Afonso and Helene Lavanant of COBRA/IRCOF, Université de Rouen, Rouen, France. All of the TWIMS data and much of the ETD fragmentation data were acquired in their facilities and with their aid.

3.7. References

(1) Mihalca, R.; Kleinnijenhuis, A. J.; McDonnell, L. A.; Heck, A. J. R.; Heeren, R. M. A. *J. Am. Soc. Mass Spectrom.* **2004**, *15* (12), 1869–1873.

(2) Byrne, A.; Williams, D. V.; Barua, B.; Hagen, S. J.; Kier, B. L.; Andersen, N. H. *Biochemistry (Mosc.)* **2014**, *53* (38), 6011–6021.

(3) Kier, B. L.; Anderson, J. M.; Andersen, N. H. *J. Am. Chem. Soc.* **2015**, *137* (16), 5363–5371.

(4) Serduyk, I. N.; Zaccai, N. R.; Zaccai, J. In *Methods in Molecular Biophysics*; Cambridge University Press: Cambridge, 2007.

(5) Heck, A. J. R. *Nat. Methods* **2008**, *5* (11), 927–933.

(6) Čeřovský, V.; Hovorka, O.; Cvačka, J.; Voburka, Z.; Bednárová, L.; Borovičková, L.; Slaninová, J.; Fučík, V. *ChemBioChem* **2008**, *9* (17), 2815–2821.

(7) Moss, C. L.; Chung, T. W.; Cerovský, V.; Turecek, F. *Collect. Czechoslov. Chem. Commun.* **2011**, *76* (4), 295–309.

(8) Locke, M. J.; McIver, R. T. *Fourier Transforms Spectrosc.* **1983**, *105*, 4226–4232.

(9) Ledvina, A. R.; Beauchene, N. A.; McAlister, G. C.; Syka, J. E. P.; Schwartz, J. C.; Griep-Raming, J.; Westphall, M. S.; Coon, J. J. *Anal. Chem.* **2010**, *82* (24), 10068–10074.

(10) Swaney, D. L.; McAlister, G. C.; Wirtala, M.; Schwartz, J. C.; Syka, J. E. P.; Coon, J. J. *Anal. Chem.* **2007**, *79* (2), 477–485.

(11) Xia, Y.; Gunawardena, H. P.; Erickson, D. E.; McLuckey, S. A. *J. Am. Chem. Soc.* **2007**, *129* (40), 12232–12243.

(12) Chung, T. W.; Tureček, F. *Int. J. Mass Spectrom.* **2011**, *306* (2–3), 99–107.

(13) Pepin, R.; Laszlo, K. J.; Peng, B.; Marek, A.; Bush, M. F.; Tureček, F. *J. Phys. Chem. A* **2014**, *118* (1), 308–324.

(14) Moss, C. L.; Chamot-Rooke, J.; Nicol, E.; Brown, J.; Campuzano, I.; Richardson, K.; Williams, J. P.; Bush, M. F.; Bythell, B.; Paizs, B.; Turecek, F. *J. Phys. Chem. B* **2012**, *116* (10), 3445–3456.

(15) Mesleh, M. F.; Hunter, J. M.; Shvartsburg, A. A.; Schatz, G. C.; Jarrold, M. F. *J. Phys. Chem.* **1996**, *100* (40), 16082–16086.

(16) Shvartsburg, A. A.; Jarrold, M. F. *Chem. Phys. Lett.* **1996**, *261* (1–2), 86–91.

(17) Campuzano, I.; Bush, M. F.; Robinson, C. V.; Beaumont, C.; Richardson, K.; Kim, H.; Kim, H. I. *Anal. Chem.* **2012**, *84* (2), 1026–1033.

(18) Giles, K.; Williams, J. P.; Campuzano, I. *Rapid Commun. Mass Spectrom.* **2011**, *25* (11), 1559–1566.

(19) Ruotolo, B. T.; Benesch, J. L. P.; Sandercock, A. M.; Hyung, S.-J.; Robinson, C. V. *Nat. Protoc.* **2008**, *3* (7), 1139–1152.

(20) Valentine, S. J.; Counterman, A. E.; Clemmer, D. E. *J. Am. Soc. Mass Spectrom.* **1999**, *10* (11), 1188–1211.

(21) Counterman, A. E.; Clemmer, D. E. *J. Am. Chem. Soc.* **1999**, *121* (16), 4031–4039.

(22) Tureček, F.; Julian, R. R. *Chem. Rev.* **2013**.

(23) Shaffer, C. J.; Marek, A.; Pepin, R.; Slovakova, K.; Turecek, F. *J. Mass Spectrom.* **2015**, *50* (3), 470–475.

(24) Schwartz, J. C.; Senko, M. W.; Syka, J. E. P. *J. Am. Soc. Mass Spectrom.* **2002**, *13* (6), 659–669.

(25) Bush, M. F.; Hall, Z.; Giles, K.; Hoyes, J.; Robinson, C. V.; Ruotolo, B. T. *Anal. Chem.* **2010**, *82* (22), 9557–9565.

(26) Frisch, M. J.; Trucks, G. W.; Schlegel, H. B.; Scuseria, G. E.; Robb, M. A.; Cheeseman, J. R.; Scalmani, G.; Barone, V.; Mennucci, B.; Petersson, G. A.; Nakatsuji, H.; Caricato, M.; Li, X.; Hratchian, H. P.; Izmaylov, A. F.; Bloino, J.; Zheng, G.; Sonnenberg, J. L.; Hada, M.; Ehara, M.; Toyota, K.; Fukuda, R.; Hasegawa, J.; Ishida, M.; Nakajima, T.; Honda, Y.; Kitao, O.; Nakai, H.; Vreven, T.; Montgomery, J. A., Jr.; Peralta, J. E.; Ogliaro, F.; Bearpark, M.; Heyd, J. J.; Brothers, E.; Kudin, K. N.; Staroverov, V. N.; Kobayashi, R.; Normand, J.; Raghavachari, K.;Rendell, A.; Burant, J. C.; Iyengar, S. S.; Tomasi, J.; Cossi, M.; Rega, N.; Millam, J. M.; Klene, M.; Knox, J. E.; Cross, J. B.; Bakken, V.; Adamo, C.; Jaramillo, J.; Gomperts, R.; Stratmann, R. E.; Yazyev, O.; Austin, A. J.; Cammi, R.; Pomelli, C.; Ochterski, J. W.; Martin, R. L.; Morokuma, K.; Zakrzewski, V. G.; Voth, G. A.; Salvador, P.; Dannenberg, J. J.; Dapprich, S.; Daniels, A. D.; Farkas, O.; Foresman, J. B.; Ortiz, J. V.; Cioslowski, J.; Fox, D. J. et al. Gaussian09, revision A.02; Gaussian, Inc: Wallingford, CT, 2009.

Chapter 4.

Kinetic Ion Thermometers for Electron Transfer Dissociation

Reproduced in part with permission from Pepin, Robert and Tureček, František, J. Phys. Chem. A Vol. 119, No. 7, Feb 19, 2015 pp 2818-2826.

Abstract

A new method for probing the energetics of the Electron Transfer Dissociation mass spectrometric fragmentation method is presented. Use of the consecutive dissociation of the leucine side chain following formation of a $\boldsymbol{z}^{\bullet}$ ion radical species and kinetic modeling of that process is shown to be an effective tool for the elucidation of unimolecular rate constants. In conjunction with RRKM theory these unimolecular rate constants are turned into energy values which provide insight into the energy processes of the ETD reaction. Results include the conclusion that ETD must be an ergodic process and that the fluoranthene neutral molecule is formed in the electronic ground state following electron transfer.

4.1. Introduction

Electron Transfer Dissociation (ETD) is a relatively new[1] fragmentation method available for mass spectrometric analyses of multiply protonated peptide ions in the gas phase. ETD involves the transfer of an electron from a radical anion donor to the multiply protonated peptide ion in the trap region of a mass spectrometer. The resulting charge reduced ion then fragments along the N-Cα bonds of the peptide ion backbone leading to the formation of N-terminal $\boldsymbol{c}$ fragments and C-terminal $z^{\bullet}$ radical type fragments. Electron Capture Dissociation (ECD), first reported by the McLafferty group at Cornell University[2] is a related method in that it also leads to characteristic N-Cα bond cleavage and the formation of N-terminal $\boldsymbol{c}$ fragments and C-terminal

$z^{\cdot}$ radical type fragments. ECD is performed in an FTICR type mass spectrometer where the orbiting peptide ions are reacted with nearly thermal free electrons. Electron Capture Induced Dissociation (ECID) is similar to ETD and ECD in that the process leads to similar fragmentation patterns. ECID involves the collision of the multiply protonated peptide cations with neutral alkali metal atoms such as potassium or cesium[3,4] and is carried out in sector type instruments. Alkali metal atoms have very low electron affinities for their first ionizable electron and as such readily transfer an electron to an analyte ion upon close approach. Collectively, these three electron based fragmentation processes have been referred to as ExD.[5]

The mechanisms of ExD fragmentation processes are not yet well understood. The leading candidate mechanisms, the Cornell model, initially proposed by the McLafferty research group at Cornell University[2] and the Utah-Washington (UW) model, initially independently proposed by the Simons research group at the University of Utah[6] and the Tureček research group at the University of Washington[7], differ in their statements on the energy of their candidate processes as well as other aspects. The Cornell model postulates that the ETD fragmentation process is a non-ergodic process and involves the creation of so-called "hot hydrogens" which drive the subsequent backbone fragmentations of the analyte peptide ions. The UW model postulates an ergodic model wherein the donated electron enters the π^* state of an amide orbital. The electronically excited charge reduced cation radical formed via electron transfer redistributes the energy via vibrational coupling, eventually reaching the electronic ground state of the charge reduced peptide cation radical. The UW model then postulates that the N-Cα bond is broken by the presence of the unpaired electron in the π^* state of an amide orbital leading to N-terminal $\boldsymbol{c}$ fragments and C-terminal $z^{\cdot}$ radical type fragments each carrying a portion of the electron recombination energy imparted by the electron transfer event.

A key difference between the Cornell and UW models then is their statements about the energetics of the ExD fragmentation process. A method of measuring the energy involved in the ExD fragmentation process then would be needed to help decide between these competing models. Much research has been done regarding energy involved in mass spectrometric processes. The energy imparted by electrospray ionization (ESI)[8] was probed using a method known as survival yield ion thermometry. This method uses ions of known, simple, fragmentation behaviors (such as benzyl pyridiniums)[9] and subjects them to the process under consideration. The resultant mass spectrum is then used in combination with computational results of bond dissociation energies to infer how much energy must have been present in the ions being fragmented. An energy distribution is then plotted based on the observed survival yields and the computed bond dissociation energies. Other methods for probing the energies involved in mass spectrometric processes, such as the kinetic method, have been explored. Briefly, the kinetic ion thermometer method is used to infer energetics between two competing processes, such as the competitive dissociation of a proton bound dimer of amines into one or the other protonated amine monomers. The relative free energies of the process can be inferred from equation 1 with a protonated dimer of methyl amine and isopropyl amine as an example.

$$\boldsymbol{ln}\left(\frac{\boldsymbol{k_1}}{\boldsymbol{k_2}}\right) = \boldsymbol{ln}\left(\frac{[\,\mathrm{CH3NH3+}]}{[\mathrm{+NH2(CH2CH3)CH3}]}\right) \approx \frac{\Delta(\Delta \boldsymbol{G})}{\boldsymbol{RT_{eff}}} \qquad \textbf{(1)}$$

It should be noted that this method is relative and only when a known calibrant is used can any absolute quantitation be attempted.[10]

The energetics of the electron transfer process can be considered as an energy balance. The change in energy during the ETD process is the result of the combination of the electron affinity of the donor, the electron-ion recombination energy of the analyte and the energy of electronic excitation of the donor as shown in equation 2.

$$\Delta E_{ETD} = EA_{Donor} - RE_{peptide} + E_{exc} \quad \textbf{(2)}$$

The electron affinity, EA, of fluoranthene is known in the literature. By exhaustive conformational searching, low energy ion conformer structures of peptides can be found and the electron-ion recombination energy can be calculated. An experimental measurement of the change in energy would then lead to information about the electronic state of the fluoranthene donor molecule.

There is an experimental difficulty with the use of any previously existing methods for probing the energy in ExD processes. It has been observed that the fragmentation process for ExD is very fast; occurring on the order of 5 - 10 μs[11]. The fastest that ion traps can trap ions and then release them for detection is on the order of 1 ms[12]. So, direct measurement of the energy in ETD isn't possible in the same way that it is possible in studying ESI. A new method has been devised that can work around these instrumental limitations and borrows some aspects from both the survival yield and kinetic methods.

It has been known for some time that ExD fragmentation processes can often lead to neutral mass losses in the spectrum which are not due to the breaking of a backbone N-Cα bond. These losses can include water loss, ammonia loss and partial side chain losses[13]. In particular there are side chain losses which are observed from the C-terminal $z^{\cdot}$ radical type fragments. In many cases these losses are explained as the result of the radical chemistry of the $z^{\cdot}$ ions. With sufficient energy present in the $z^{\cdot}$ ion radical driven hydrogen migrations can occur, leading to the radical site moving around[14], causing a shuffling of the bonding electrons, and sometimes leading to a bond breakage. This neutral loss could carry away the radical or leave it present in

the ion.

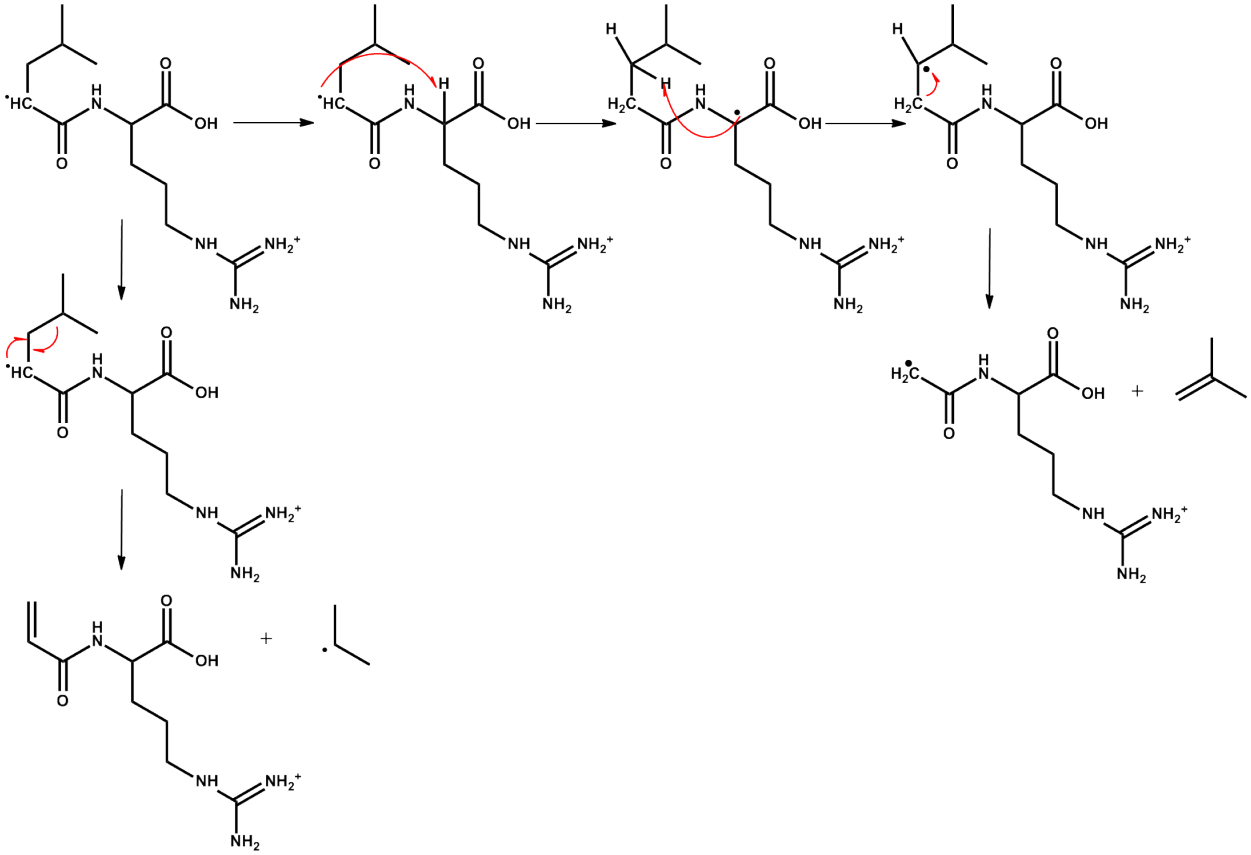

Figure 26: Two possible routes for radical based losses from $z_2^{\cdot}$ LR following N-Ca bond cleavage. Top left to bottom left: Alpha carbon promotes cleavage of beta gamma bond leading to loss of radical $^{\cdot}C_3H_7$. Top left to right: Radical migration leads to loss of neutral C_4H_8.

The extent to which these secondary radical induced losses occur would be dependent on the energy present in the $z^{\cdot}$ ion at the time of its creation via ETD. Measuring the survival yield of a $z^{\cdot}$ ion and the creation of a smaller fragment resulting from a neutral loss from that ion as a function of time could allow the inference of kinetic rate constants for the process and an estimate of the energy, via comparison to RRKM derived rate constants, that the parent $z^{\cdot}$ ion must have had at the time of dissociation.

In this work, secondary radical induced dissociation of the loss of neutral C_3H_7 from the side chain of leucine containing $z^{\cdot}$ ions is used as a kinetic ion thermometer for the energy deposited in the ETD fragmentation process. A series of A_nLK and A_nLR (n=2…6) peptides are

chosen to generate $z_2^{\bullet}$ ions as thermometers for probing the energy deposited upon electron transfer from anion radical fluoranthene. The proposed kinetic scheme is shown below.

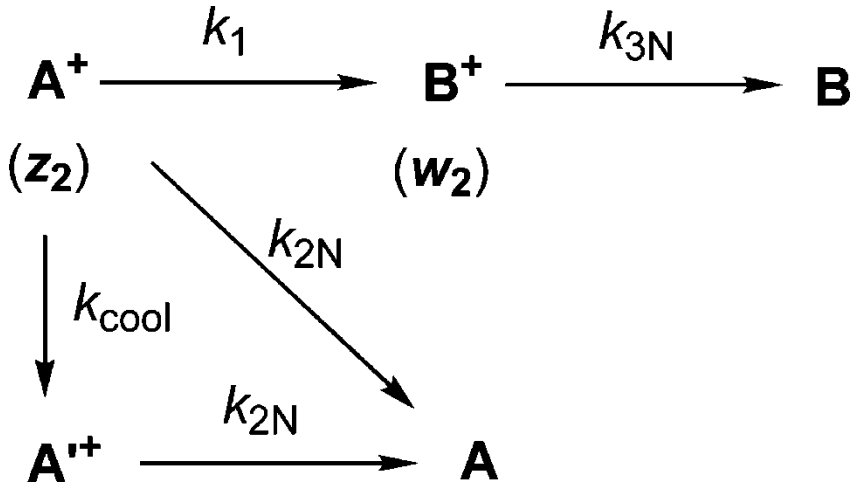

Figure 27: Proposed kinetic scheme for loss of $^{\bullet}C_3H_7$ from $z_2^{\bullet}$ LK or LR ions to form the w_2 product ion[12]

Rate constant k_1 defines the rate at which the spontaneous loss of neutral C_3H_7 radical from the $z_2^{\bullet}$ occurs leading to the formation of the w_2 ion. Rate constants k_{2N} and k_{3N} are defined as the rate of neutralization of the $z_2^{\bullet}$ and w_2 ions, respectively, due to over titration with fluroanthene reagent. Rate constant k_{cool} is the rate of collisional cooling experienced by the $z_2^{\bullet}$ ions which causes them to fall below the dissociation threshold. The differential rate laws describing this process and the resulting integrated rate laws are shown below.

$$\frac{dA}{dt} = -(k_1 + k_{2N} + k_{cool})A \qquad A = A_0 e^{-(k_1+k_{2N}+k_{cool})t} = A_0 e^{-Kt} \qquad K = k_1 + k_{2N} + k_{cool}$$

$$\frac{dA'}{dt} = k_{cool}A - k_{2N}A' \qquad A' = \frac{A_0 k_{cool}}{K - k_{2N}}\left[e^{-k_{2N}t} - e^{-Kt}\right]$$

$$\frac{dB}{dt} = k_1 A - k_{3N}B \qquad B = \frac{A_0 k_1}{K - k_{3N}}\left[e^{-k_{3N}t} - e^{-Kt}\right]$$

Figure 28: Derived kinetic rate laws from the kinetic scheme. Left: Differential rate laws. Center: Integrated rate laws.

It is proposed that through experimental measurement of rate constants K_{3N} and K_{2N} and then fitting of time resolved ETD data the rate constant K_1 for the formation of the w_2 ions can be

found. Comparison to RRKM calculation of energy dependent rate constants will give an energy value to this process. By measuring a series of peptides which generate the same z2 thermometer ion the ergodicity of the ETD process can be confirmed and by application of the energy balance expressed in equation (2) it can be observed if the fluoranthene molecule is formed in an excited state post-electron transfer.

4.2. Experimental

4.2.1. Materials All peptides used in this study were synthesized in house using the standard fmoc solid phase synthetic methodology[15,16] with fmoc protected amino acids purchased from Sigma-Aldrich and fmoc-Lys and fmoc-Arg preloaded Wang resins purchased from Bachem. Solvents were reagent grade or better from Fisher.

4.2.2. Mass Spectrometry All measurements in this work were carried out using a Thermo Fisher Scientific LTQ XL with ETD module equipped with an auxiliary negative chemical ionization source for the generation of fluoranthene anion radicals[17]. Samples were ionized using a custom micro electrospray source typically operating at 2.7kV. Samples were sprayed from a solution of methanol/water/acetic acid (50/50/1) at a concentration of ~10μM. ETD spectra were measured using an isolation width of 2 m/z and reaction times were varied from 1 - 1000 ms. Collision induced dissociation (CID) MS^3 spectra were also collected using an isolation width of 2 m/z for a reaction time of 30ms and normalized collision energies (NCE) were varied to give a range of survival yields up to and including full dissociation of the precursor ion into products.

4.2.3 Calculations Full conformational analysis was preformed using the ConformSearch engine previously developed in the Tureček research group[18]. $(AALR+2H)^{2+}$ precursor ions were subjected to this procedure to generate several low energy ion conformers. Low energy ion

conformers for the $(AAALR+2H)^{2+}$ ion were generated from the previously calculated low energy ion conformers of $(AAVAR+2H)^{2+}$ with appropriate modification to the side chains and then submitted for reoptimization[19]. This approach was justified by the lack of polar groups in either AAVAR's side chains or AAALR's side chains. Such nonpolar side chains should not disrupt the hydrogen bonding patterns experienced by the molecules in the gas phase.

All electronic structure calculations were carried out using the Gaussian09 suite of programs[25]. Conformational analysis of the $z_2^{\bullet}$ LR and LK ions were performed using full geometry optimization of starting structures with the B3LYP and M06-2X density functionals at the 6-31+G(d,p) level. Multiple torsional angles were then rotated 60, 90 or 180 (according to the symmetry of the particular bonds involved) and reoptimized. Some candidate structures coalesced to the same structure and the duplicates were ignored. The surviving candidate structures were then subjected to single point energy calculations at the 6-311++G(2d,p) and aug-cc-pVTZ basis set levels using both density functional methods as well Møller-Plesset 1st order perturbational theory (MP2). In some cases the M06-2X/aug-cc-pVTZ combination gave results that could only be explained as 1st excited state results so this functional/basis set combination was deemed unreliable and those results were excluded from consideration. Resulting structures were confirmed as local energy minima by harmonic frequency analysis showing 0 imaginary frequencies. Transition state search for the neutral loss of C_3H_7 radical was carried out with the lowest energy $z_2^{\bullet}$ ion candidate structures as starting points. The found transition state structures were confirmed by harmonic frequency analysis showing 1 imaginary frequency. The structures of the lowest energy conformers as well as the found transition state structures and frequencies were used as inputs for the Rice-Ramsperger-Kassel-Marcus theory rate constant calculations (RRKM)[26].

4.3. Results and Discussion

4.3.1. Selection of Ion Thermometers Initially, peptides LGGGK, GLGGK, GGLGK and GGGLK were considered as candidate thermometer ions. In order to have a reliable thermometer molecule, it is essential that the spontaneous radical induced dissociation post-ETD be simple and well understood. The LGGGK peptide was rejected because the candidate thermometer ion resulting from ETD of the 2+ charge state would be ambiguous. The loss of ammonia from the lysine side chain would be isobaric with the true $z_5^{\cdot}$ ion resulting from the loss of the peptide's N-terminus. GLGGK was rejected because the candidate $z_4^{\cdot}$ ion did not form in sufficient abundance upon ETD of the doubly charged precursor. GGGLK was rejected because the $z_2^{\cdot}$ candidate thermometer ion lost the C_3H_7 neutral radical from the leucine side chain too quickly for kinetic measurements. GGLGK was rejected as the $z_3^{\cdot}$ candidate thermometer ion lost both the C3H7 neutral radical as well as the C_4H_8 neutral closed-shell molecule. The peak representing loss of C_4H_8 was isobaric with c_3 and its formation could proceed through multiple pathways and was considered to be too complicated of a loss for the $z_3^{\cdot}$ to be an ideal thermometer ion.

An analogous set of peptides using alanine residues instead of glycine residues were considered next as thermometer candidates. The mass shift resulting from replacing glycine with alanine resolved the previously isobaric peaks in the spectra. ALAAK was rejected for a similar reason to the GLGGK; the candidate thermometer did not form in sufficient abundance. AAALK and AALAK peptides were considered to be excellent choices for generation of thermometer $z^{\cdot}$ ions. Upon measurement of time resolved ETD the $z^{\cdot}$ ions showed a noticeable time dependence which allowed for kinetic modeling of the dissociation processes. Elucidation of the complete breakdown curves for the $z^{\cdot}$ ions by CID showed minimal amount of loss of C_4H_8 neutral losses

indicating that the breakdown of these ions could be considered as having a single fragmentation channel. To keep computational demands as low as possible AAALK and the $z_2^{\bullet}$ LK ions generated upon ETD were chosen as the candidate thermometer. Eventually, it was found that the -LK $z_2^{\bullet}$ ions needed to be more basic and -LR terminated peptides were added to our consideration.

4.3.2. Degree of Freedom Effects It is of prime importance to this study to probe the effect of degrees of freedom on the complementary fragment to the thermometer ion of interest. To that end a series of -LK C-terminal peptides were studied ranging in size from tripeptides to octapeptides. A list of peptides screened are shown in the table below.

Peptide	Mass	Peptide	Mass
ALK	330.23	ALR	358.23
AALK	401.26	AALR	429.27
AAALK	472.30	AAALR	500.31
AAAALK	543.34	AAAALR	571.34
AAAAALK	614.38	AAAAALR	642.38
AAAAAALK	685.41	AAAAAALR	713.42
AAHAAALK	751.43		
YAAAAALK	777.44		
YAHAAALK	843.46		
LAAAAALK	727.46		
LAHAAALK	793.48		
hexa-AAALK	725.54		

Table 13: Peptides screened for useful thermometry information.

In some cases a single alanine was replaced with histidine, tyrosine or additional leucine residues. A special amino acid, 2-aminohexadecanoic acid, was added to the N-terminus of a AAALK pentapeptide to create a hexapeptide with high degrees of freedom, but only one additional backbone residue as a test to see if backbone length plays a role independent of purely degree of freedom effects.

Subjecting these peptides to time-resolved ETD and then studying the amounts of spontaneous C_3H_7 loss have shown a distinct degree of freedom effect. As the peptide increases

in size from a tetrapeptide to the heptapeptide, the proportion of $z_2^{\bullet}$ ion dissociating decreases very noticeably as can be seen in the figure below. Part (a) shows the molar fraction of $z_2^{\bullet}$ ion remaining following the ETD reaction at 200ms reaction time as a function of the total number of residues in the peptide. Part (b) shows the molar fractions of $z_2^{\bullet}$ ions as a function of ETD reaction time for each peptide. Inspection of this figure makes the degree of freedom effect quite obvious. This is very strong evidence for an ergodic process.

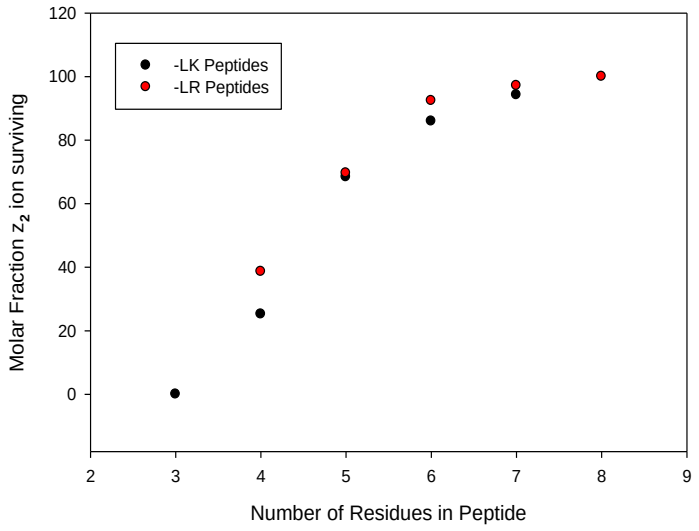

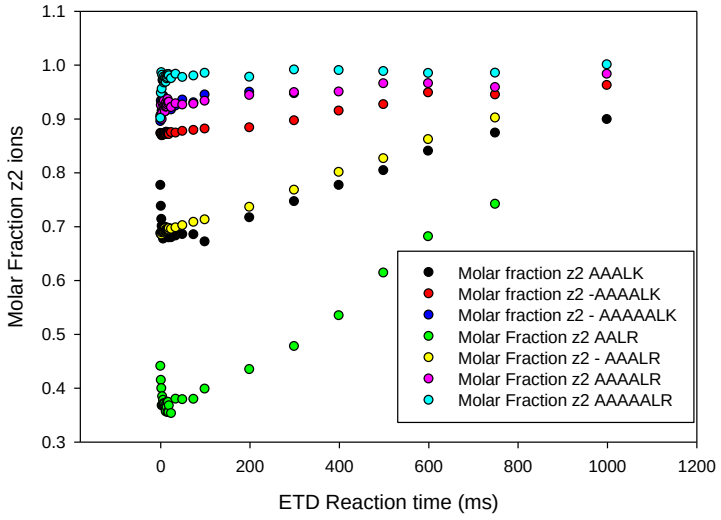

Figure 29: Degree of freedom effects on relative proportion of z2 ions. Top: Molar fraction of z2 ions formed at 200ms ETD reaction time. Bottom: Molar fractions of z2 ions formed from various peptides as a function of ETD reaction time.

Also, in the case of the -LK terminated thermometer candidates, a practical size limit regarding ion basicities was encountered. Peptides bigger than the hexapeptide AAAALK did not form the $\boldsymbol{z_2}^{\bullet}$ ion but instead formed the complementary ***c*** ion. This shows that the ***c*** ion was outcompeting the $\boldsymbol{z_2}^{\bullet}$ ion for the charge prior to the dissociation of the ion-molecule complex generated by cleavage of the N-Cα bond. This problem was overcome by changing the C-terminal residue from lysine to the more basic arginine. This ensured that the charge would remain with the C-terminal fragment. The more basic -LR peptides showed formation of the $\boldsymbol{z_2}^{\bullet}$ ion all the way to the octapeptide, but did not show dissociation of the z2 ion down to the corresponding -C_3H_7 product. This indicates that the method has a practical size limit regardless of ion basicity. The -LR $\boldsymbol{z_2}^{\bullet}$ ion does not have enough degrees of freedom in comparison to a complementary neutral $\boldsymbol{c_6}$ fragment. The energy provided by the electron transfer is distributed such that after N-Cα bond cleavage there is insufficient energy in the $\boldsymbol{z_2}^{\bullet}$ to further dissociate.

4.3.3. Measurement of k_{2N} and k_{3N} Rate constants of neutralization for the $\boldsymbol{z_2}^{\bullet}$ and $\boldsymbol{w_2}$ ions were measured directly in the LTQ-XL. Doubly charged precursor ions $(AAALK+2H)^{2+}$ and

$(AAALR+2H)^{2+}$ were mass selected and subjected to ETD. The resultant $\boldsymbol{z_2}^{\cdot}$ and $\boldsymbol{w_2}$ product ions were mass selected and subjected to a second ETD experiment of varying reaction times. The amount of $\boldsymbol{z_2}^{\cdot}$ or $\boldsymbol{w_2}$ ion present in the MS^2 spectra were taken as the initial concentration I_o and the amounts of $\boldsymbol{z_2}^{\cdot}$ or $\boldsymbol{w_2}$ surviving the MS^3 ETD step were taken as the final concentration I. A semilog plot of I/I_o vs time gave lines of slope equal to equal to k_{2N} and k_{3N}. A plot showing these values for $\boldsymbol{z_2}^{\cdot}$ LR thermometer is shown below[20].

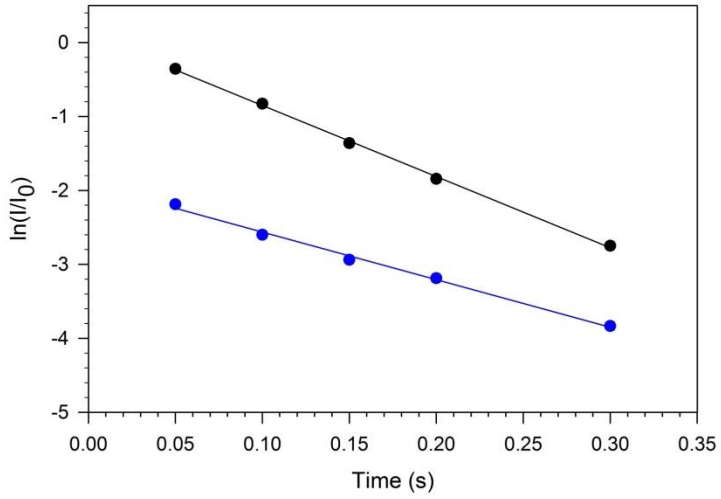

Figure 30: Semi-log plot of z2 ion depletion from electron transfer. Black dots: z2. Blue dots: w2.

4.3.4. Fitting of Time Dependent ETD to Kinetic Model The integrated rate laws shown above were fitted to the time resolved ETD data to elucidate the values of rate constant k_1. To provide an estimate for the rate of collisional cooling, the number of collisions a $\boldsymbol{z_2}^{\cdot}$ LR or LK ion would be expected to experience were first calculated using equations (3) and (4) below. The number density of Helium atoms (3) in the trap was calculated using the He pressure from literature descriptions of the LTQ instrument and the ideal gas law.

$$N_{He} = \frac{N_A n}{V} = \frac{N_A P}{RT} \quad \textbf{(3)}$$

$$k_{coll} = N_{He} \Omega v \quad \textbf{(4)}$$

The collisional cross sections Ω of the $z_2^{\bullet}$ LR or LK ions were calculated using the Mobcal program[21,22] and then multiplied by the velocity of the ions in the trap to describe a volume that the ions would traverse in a second and then multiplied by the number density of He atoms to describe the number of collisions that ion would have experienced in a given time; equation (4). Velocity of the ions were calculated from the standard formula for the root mean square velocity of gaseous particles.

The cooling constant k_{cool} is a number smaller than k_{coll}. Only a certain fraction of collisions will be cooling and this proportion is referred to as the accommodation coefficient β[23] and is a parameter that will be found through the fitting procedure.

$$k_{cool} = \beta k_{coll} \quad \textbf{(5)}$$

The data from time resolved ETD were fitted using a 2 variable least squares minimization technique. This led to β values for each peptide species shown in the table below.

	β values	k_{cool}	k_1
AAALK	4.50E-03	520	250
AAAALK	1.43E-02	551	87
AAAAALK	7.95E-03	650	55
AALR	6.41E-03	585	1028
AAALR	1.45E-02	649	304
AAAALR	1.47E-02	600	53
AAAAALR	5.03E-02	497	14

Table 14: Accomodation coefficients beta, the resulting k_{cool} and k_1 from fitting routine.

These values are all very much less than 1 indicating that the cooling process by the He bath gas of the trap is very inefficient.

The second fitting parameter for the above mentioned 2 variable fitting technique is the rate constant of interest k_1. This value is reported in the table above and is further suggestive of the ergodicity of the ETD process when one notes how the increase in size of the parent doubly charged ion results in a decrease in the rate of formation of the w_2 ion.

4.3.5. Rice-Ramsperger-Kassel-Marcus calculations Fully optimized low energy ion conformers were calculated using the procedure described in the Experimental section above. The resultant B3LYP and M06-2X derived structures were then submitted to transition state (TS) searching in the Gaussian09 program suite using the opt=modredundant command specifying stretching of the bond between the β and ɤ carbon atoms of the leucine side chain in 0.02 angstrom increments. The optimized starting structures and transition state structures along with calculated principle moments of inertia were used as inputs for the RRKM calculations. The resultant energy dependent rate constants k(E) were then compared to the fitted k_1 values from the experimental time resolved ETD spectra.

4.3.6 Energies of ETD reaction As can be seen in the table below, the internal energies for the $\boldsymbol{z_2}^{\bullet}$ ion show a pronounced trend that is inversely proportional to the number of degrees of freedom in the complementary neutral ***c*** fragment. As a confirmation of this empirical observation, standard thermodynamics were used to calculate the rotational-vibrational enthalpies of $\boldsymbol{z_2}^{\bullet}$ ions and for the neutral $\boldsymbol{c_2}$ fragments from the ETD reaction of $(AALR+2H)^{2+}$ at several temperatures. This gave results for the partitioning of energy following ETD which showed 63% of the energy was found in the $\boldsymbol{z_2}^{\bullet}$ ion. When compared to the partitioning of energy that would result from simply considering the degrees of freedom in each fragment a close agreement of 63% vs 64% was found. Seeing this close agreement between methods provides the justification for application of the degree of freedom method to the remaining, larger, peptides.

Internal Energy (kJ/mol)				
peptide	z2	cation-radical	ΔE_{ETD}	RE
AALR	257	400	307	420-424
AAALR	242	431	324	430-442
AAAALR	223	448	327	
AAAAALR	211	472	305	
AAALK	214	390	285	
AAAALK	204	421	302	

Table 15: Interal Energies found for the various z2 ions, the charge reduced cation radicals and the change in energy during the ETD reaction.

The resultant energies for the charge reduced cation-radical prior to dissociation are shown in the table. Also shown is the resulting ΔE_{ETD} from the degree of freedom partitioning method. The calculated vertical recombination energy from the exhaustive conformational analysis (as described in the Experimental Section) of doubly charged AALR and AAALR ions is also included. Returning to the energy balance describing the ETD reaction as shown in equation (2), the question of how much energy is available for excitation of the anion donor can be addressed.

$$\Delta E_{ETD} = EA_{Donor} - RE_{peptide} + E_{exc} \qquad \textbf{(2)}$$

Using AALR as an example, the value for the excitation energy of the flouranthene anion donor is found to be 155-215 kJ/mol (when considering the energetics for the formation of the neutral enolimine vs amide forms of the neutral $\boldsymbol{c_2}$ fragment). The known energy for the first excitation of the fluoranthene neutral molecule[24] is 333 kJ/mol. This shows that the neutral fluoranthene generated by the ETD reaction cannot leave in an excited electronic state. This energy may be carried away by photon emission, by collisional cooling of an intermediate or perhaps by collision of the ion-neutral complex with the He bath gas of the linear ion trap prior to dissociation of the complex.

4.4. Conclusions

The use of consecutive radical induced dissociation following an ETD reaction can be used to probe the energetics of the ETD reaction. The β-γ dissociation of the leucine side chain from $\boldsymbol{z}$

ion radicals proceeds on a timescale that is amenable to measurement on the timescale of a linear ion trap mass spectrometer. Use of such a kinetic ion thermometry (KIT) method has been shown to be effective in the case of peptides of the form (A_nLR) n=2..6 at extracting experimental values for unimolecular rate constants. Comparison with RRKM derived rate constants for the same $z_2^{\cdot} \rightarrow w_2$ decomposition provides scaling into energy units. The KIT-ETD method has shown that ETD is an ergodic process and that the neutral fluoranthene molecule formed by the reaction is not formed in an excited electronic state owing to the lack of sufficient available energy following reaction.

4.5. References

(1) Syka, J. E. P.; Coon, J. J.; Schroeder, M. J.; Shabanowitz, J.; Hunt, D. F. *Proc. Natl. Acad. Sci. U. S. A.* **2004**, *101* (26), 9528–9533.

(2) Zubarev, R. A.; Kelleher, N. L.; McLafferty, F. W. *J. Am. Chem. Soc.* **1998**, *120* (13), 3265–3266.

(3) Hayakawa, S.; Minami, K.; Iwamoto, K.; Toyoda, M.; Ichihara, T.; Nagao, H. *Int. J. Mass Spectrom.* **2007**, *266* (1–3), 122–128.

(4) Byskov, C. S.; Weber, J. M.; Nielsen, S. B. *Phys. Chem. Chem. Phys.* **2015**, *17* (8), 5561–5564.

(5) Tureček, F.; Julian, R. R. *Chem. Rev.* **2013**.

(6) Sobczyk, M.; Anusiewicz, I.; Berdys-Kochanska, J.; Sawicka, A.; Skurski, P.; Simons, J. *J. Phys. Chem. A* **2005**, *109* (1), 250–258.

(7) Syrstad, E. A.; Tureček, F. *J. Am. Soc. Mass Spectrom.* **2005**, *16* (2), 208–224.

(8) Gabelica, V.; Pauw, E. D. *Mass Spectrom. Rev.* **2005**, *24* (4), 566–587.

(9) Huang, Y.; Yoon, S. H.; Heron, S. R.; Masselon, C. D.; Edgar, J. S.; Tureček, F.; Goodlett, D. R. *J. Am. Soc. Mass Spectrom.* **2012**, *23* (6), 1062–1070.

(10) Cooks, R. G.; Kruger, T. L. *J. Am. Chem. Soc.* **1977**, *99* (4), 1279–1281.

(11) Ture?ek, F.; Syrstad, E. A.; Seymour, J. L.; Chen, X.; Yao, C. *J. Mass Spectrom.* **2003**, *38* (10), 1093–1104.

(12) Pepin, R.; Tureček, F. *J. Phys. Chem. B* **2015**, *119* (7), 2818–2826.

(13) Fung, Y. M. E.; Chan, T.-W. D. *J. Am. Soc. Mass Spectrom.* **2005**, *16* (9), 1523–1535.

(14) Shaffer, C. J.; Pepin, R.; Tureček, F. *J. Mass Spectrom.* **2015**.

(15) Merrifield, R. B. *J. Am. Chem. Soc.* **1963**, *85*, 2149–2154.

(16) Carpino, L. A.; Han, G. Y. *J. Am. Chem. Soc.* **1970**, *92* (19), 5748–5749.

(17) Alexander G. Harrison. *Chemical Ionization Mass Spectrometry*; CRC Press, 1989.

(18) Moss, C. L.; Chamot-Rooke, J.; Nicol, E.; Brown, J.; Campuzano, I.; Richardson, K.; Williams, J. P.; Bush, M. F.; Bythell, B.; Paizs, B.; Turecek, F. *J. Phys. Chem. B* **2012**, *116* (10), 3445–3456.

(19) Tureček, F.; Moss, C. L.; Chung, T. W. *Int. J. Mass Spectrom.* **2012**, *330–332*, 207–219.

(20) Pepin, R.; Tureček, F. *J. Phys. Chem. B* **2015**, *119* (7), 2818–2826.

(21) Mesleh, M. F.; Hunter, J. M.; Shvartsburg, A. A.; Schatz, G. C.; Jarrold, M. F. *J. Phys. Chem.* **1996**, *100* (40), 16082–16086.

(22) Shvartsburg, A. A.; Jarrold, M. F. *Chem. Phys. Lett.* **1996**, 86–91.

(23) Troe, J.; Viggiano, A. A.; Williams, S. *J. Phys. Chem. A* **2004**, *108* (9), 1574–1581.

(24) Maddams, W. F.; Schnurmann, R. *J. Chem. Phys.* **1951**, *19* (7), 973–974.

(25) Frisch, M. J.; Trucks, G. W.; Schlegel, H. B.; Scuseria, G. E.; Robb, M. A.; Cheeseman, J. R.; Scalmani, G.; Barone, V.; Mennucci, B.; Petersson, G. A.; Nakatsuji, H.; Caricato,

M.; Li, X.; Hratchian, H. P.; Izmaylov, A. F.; Bloino, J.; Zheng, G.; Sonnenberg, J. L.; Hada, M.; Ehara, M.; Toyota, K.; Fukuda, R.; Hasegawa, J.; Ishida, M.; Nakajima, T.; Honda, Y.; Kitao, O.; Nakai, H.; Vreven, T.; Montgomery, J. A., Jr.; Peralta, J. E.; Ogliaro, F.; Bearpark, M.; Heyd, J. J.; Brothers, E.; Kudin, K. N.; Staroverov, V. N.; Kobayashi, R.; Normand, J.; Raghavachari, K.;Rendell, A.; Burant, J. C.; Iyengar, S. S.; Tomasi, J.; Cossi, M.; Rega, N.; Millam, J. M.; Klene, M.; Knox, J. E.; Cross, J. B.; Bakken, V.; Adamo, C.; Jaramillo, J.; Gomperts, R.; Stratmann, R. E.; Yazyev, O.; Austin, A. J.; Cammi, R.; Pomelli, C.; Ochterski, J. W.; Martin, R. L.; Morokuma, K.; Zakrzewski, V. G.; Voth, G. A.; Salvador, P.; Dannenberg, J. J.; Dapprich, S.; Daniels, A. D.; Farkas, O.; Foresman, J. B.; Ortiz, J. V.; Cioslowski, J.; Fox, D. J. et al. Gaussian09, revision A.02; Gaussian, Inc: Wallingford, CT, 2009.

(26) Zhu, L.; Hase, W. L. Quantum Chemistry Program Exchange: Program No. QCPE 644.; Indiana University: Bloomington, Indiana, 1994

Chapter 5.

Gas Phase Covalent Bond Formation in Non-Covalent Proton Bound Peptide Dimer Complexes Utilizing Newly Synthesized Photo-Lysine Amino Acid.

Abstract Gas phase non-covalent peptide dimer complexes containing the newly developed photo lysine amino acid are generated by electrospray and are "stitched" together utilizing diazirine-carbene photochemistry. A detailed protocol for the synthesis of this photo-lysine is presented. An extensive number of combinations of photo peptide with various target peptides is studied leading to insight regarding the gas phase bond insertion reactions initiated by carbenes. A means to quantify stitching efficiencies is presented and a complementary statistical method to approximately map stitching locations is presented as well. A key result is the tendency for the insertion reaction to localize towards the C-terminal portion of the target peptide regardless of sequence or diazirine tag position when the charge is present on the photo peptide. The recognition that there is little specificity in insertion location along the target peptide is an important result as well because there are fragments present which are indicative of multiple stitching locations.

5.1. Introduction

Diazirine tagged proteins have been of interest in biochemical applications.[1–3] Incorporation of appropriately tagged amino acids into cell growth medium can lead to proteins with an added functionality for manipulation. Cells are grown with diazirine tagged amino acids as part of the growth medium and these are endogeneously incorporated into proteins. Cells are then irradiated with 355nm light and a carbene is generated[4] leading to new intermolecular covalent bond formation; attaching one protein to another thus leading to information regarding the interactions of the proteins within these cells.[1]

Inspired by this chemistry we have endeavored to perform analogous experiments with gas phase molecules in an effort to learn conformational information. As in solution, exposure to 355nm photons causes the N_2 of the diazirine ring to detach and leave as elemental diatomic nitrogen leaving a carbene in its place. This carbene is highly reactive and can insert into any bonds which are proximate to the site of the carbene. The goal of this endeavor was to accomplish an intramolecular bond insertion thereby finding out which bonds are proximate to the carbene. Fragmentation of this "stitched" ion should thus allow identification of the site of the insertion. Such experimental evidence would lead to information about the gas phase conformation of the ion under study. This information is needed as a probe towards elucidating the fragmentation mechanism behind electron based fragmentation methods. There is experimental evidence suggesting the conformation plays an important role in determining the location and frequency of N-Cα bond cleavage.[5]

Two diazirine tagged amino acids are already in commercial use (offered by Thermo Scientific) and can be used for *in vivo* studies: photo-leucine and photo-methionine. Both of these photo tagged amino acids have side chains which are completely nonpolar and as such, interatomic interactions between atoms in the side chain mimic the endogenous peptides and proteins. Extensive computational modeling of L* containing peptides has shown that the L* residue does not alter the gas phase conformation of peptides when substituted for L.[6] The net effect of this is that in the gas phase the side chains of these amino acids stick off in space away from the backbone of the peptides they are incorporated into much as native leucine or methionine would be observed to do (computational evidence to be published in a forthcoming article). The desired insertion reaction is in competition with a very fast 1,2 hydrogen shift reaction[7] which quenches

the reactivity of the carbene. If the carbene is not in close enough proximity to another covalent bond the stitching won't occur.

In an effort to make use of this diazirine chemistry, but overcome the problems inherent in the use of photo-leucine (abbreviated as L*) and photo-methionine (M*) a new photo labeled amino acid has been synthesized. This new amino acid, dubbed photo-lysine and abbreviated K*, has an amine group on the end of the side chain, which, under electrospray conditions, typically holds a charging proton. The increased polarity of the lysine due to the amine and the additional polarity due to the charging proton leads us to believe that through hydrogen bonding type interactions that the diazirine chromophore should now have an increased chance of being close enough in space to perform an intramolecular bond insertion reaction. To date, however, only one intramolecular bond insertion reaction has been observed and fragmentation of the self-stitched ion has yielded little information about the stitching location.

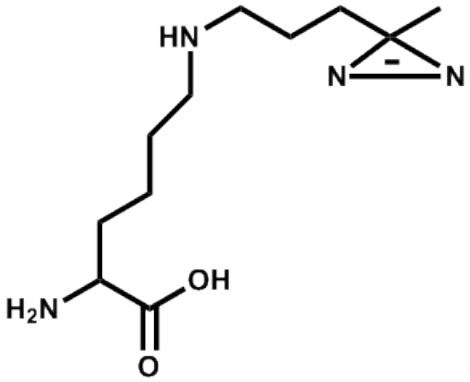

Scheme 9: The newly developed photo lysine amino acid.

To improve our understanding of the factors involved in a gas phase carbene insertion reaction we have made solutions of mixed peptides in an attempt to generate non-covalent peptide dimer heterocomplexes from electrospray. After generation of the gas phase dimers in an ion trap instrument, the dimers are mass isolated and exposed to 355nm photons. Fragmentation of the resulting peak representing loss of 28 mass units shows that gas phase insertion reactions do

happen quite easily given a group proximate to the exposed carbene. Reported in this chapter is the application of the new photo lysine amino acid to gas phase dimer photo stitching reactions.

5.2. Experimental

5.2.1. Materials Unless otherwise stated, most small molecule reagents used in this work were purchased from Sigma Aldrich and were used as received without additional purification. Photo-leucine and photo-methionine were purchased from Thermo Scientific and were fmoc protected in house. Wang resin preloaded with Fmoc-Lysine(MTT)-OH amino acid was purchased from Bachem. Solvents were purchased from Fisher and were reagent grade or better, unless otherwise noted.

5.2.2. Peptide Synthesis Peptides not containing a photo label were synthesized on a CEM Liberty Blue peptide synthesizer using standard Fmoc[8] solid phase peptide synthesis[9] methodology.

5.2.3. Laser System The Ekspla laser system consists of a 20Hz pulsed Nd:YAG pump laser outputting up to 226mJ per pulse of 1064nm infrared photons. The infrared photons are frequency doubled through a non-linear BBO to generate the 532nm product beam. The 532nm product beam is then passed through a second non-linear BBO crystal and the resulting frequency tripled output at 355nm is directed towards the mass spectrometer. The maximum output power of the third harmonic beam is limited to 55mJ per pulse. The pulse length is 3-6ns. In these experiments, the power was limited to 16-18mJ.

5.2.4. Mass Spectrometry Dimer stitching experiments were carried out on a Thermo Fisher LTQ-XL with ETD linear ion trap mass spectrometer which was modified to allow irradiation of trapped ions with light from a laser source. Some measurements of individual peptides were carried out on a Thermo Fisher Orbitrap Fusion with resolution set at 120,000 as well as on a

Thermo Fisher LTQ Orbitrap with resolution set at 60,000. Peptide solutions for individual peptide analysis were 10 μM in methanol:water:acetic acid (50:50:1). Peptide solutions for dimer measurements were 50 μL of each component peptide stock solution diluted to 1.5mL in methanol:water:acetic acid(50:50:1). In some cases 1% meta-nitro benzyl alcohol (mNBA) as a supercharging agent[10] was added to the solution to enhance charging and increase the amount of peptide dimer complexes observed.

Dimer stitching experiments were carried out in the following manner. The highly concentrated solutions containing the photo labeled peptide and the non-photo labeled "target" peptide were electrosprayed directly into the vacuum inlet of the LTQ spectrometer. Ions corresponding to the *m/z* of a proton bound dimer of the photo and target peptides were then mass isolated using a wide (6 *m/z*) window and stored in the ion trap for 1000ms and irradiated with 19 pulses of 355nm light at 16-18mJ/pulse. Photo product ions corresponding to a loss of N_2 from the proton bound dimer complex were then again mass isolated with a wide window and subjected to collision induced dissociation (CID).

5.2.5. Synthesis of 4-diazirine pentanol 4-diazirine pentanol was synthesized according to the procedure of Shigdel et al[11]. 25 grams of 5-hydroxy-2-pentanone were added to an oven dried 3 neck round bottom flask with a magnetic stir bar. One neck was sealed with a rubber septum, the second was fitted with a dewar type condenser (attached to a mineral oil bubbler) and the third was fitted with an alcohol thermometer capable of reading to -100° C in a ground glass thermometer adapter. A line from an anhydrous ammonia tank with needle at the end was introduced through the septum. The flask assembly was immersed in a bath of 2-propanol and dry ice and set over a stir plate. Dry ice and 2-proponol were added to the condenser as well. Anhydrous ammonia flow was initiated and flow rate adjusted so that a drip rate of condensing

liquid ammonia at approximately 4-5 drops per minute was achieved. Once 100mL liquid ammonia was condensed in the flask the reaction was left to sit for 3 hours at -78°C. 32.4 grams of hydroxylamine-o-sulfonic acid was suspended in methanol and added dropwise through the septum. The reaction mixture was left to react overnight under an N_2 atmosphere and the dry ice propanol bath was removed to allow evaporation of excess ammonia. The reaction mixture was then filtered through Whatman #5 filter paper in a sintered glass filter funnel and the liquid filtrate collected. This liquid was then cooled to ice water temperature and 1 equivalent triethylamine was added. Iodine was added slowly until dark orange-brown iodine color persisted while the ice water temperature was maintained. After an additional 2 hours, the methanol was evaporated. Crude product was extracted with diethyl ether and dried over magnesium sulfate. Following evaporation of ether, the crude product was vacuum distilled at aspirator pressures (a heat gun was needed to maintain flow of distillate) to yield 9.1 grams of pale yellow oil. The product was verified by ^{1}H NMR in $CDCl_3$ to be the desired 4-diazirine pentanol. ^{1}H NMR (300 MHz, $CDCl_3$, δ): 3.62 (br s, 2H, -CH_2-, #4), 1.69 (br, 2H, -CH_2-, #3), 1.46 (t, 2H, -CH_2-, #2), 1.03 (s, 3H, -CH_3, #1).

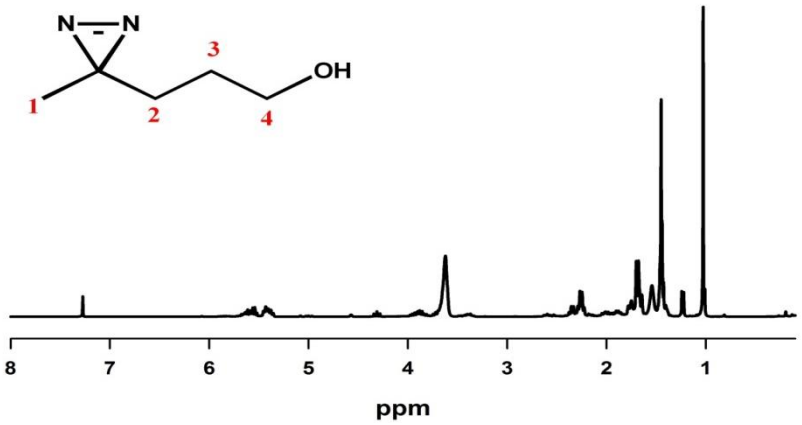

Figure 31: ^{1}H NMR spectrum of 4-diazirine pentanol product.

5.2.6. Synthesis of 1-iodo-4-diazirine pentane 1-iodo-4-diazirine pentane was synthesized also according to the procedure of Shigdel, et al.[11] An oven dried 100mL round bottom flask with magnetic stir bar and 1.1 equivalents triphenylphosphine was sealed with a rubber septum and flushed with N_2 gas. Flask was suspended in an ice water bath on a stir plate and 50mL distilled dicholoromethane was added slowly and stirred until all triphenylphosphine dissolved. 1.1 equivalents of iodine were added followed by an excess of imidazole. Once the color of iodine vanished, 3.48 grams of 4-diazirine pentanol were added via syringe and needle through the septum and left to mix overnight under a N_2 atmosphere. After reaction overnight, the dichloromethane was evaporated and deionized water was added and the crude material was then extracted with diethyl ether. The ether phase was then dried over magnesium sulfate. The crude liquid product was then purified by column chromatography on silica gel in pure hexanes using a dry loading method. Fractions were monitored by TLC visualized under a UV lamp. Product containing fractions were then combined and evaporated. Purified product (1.8 grams) was stored neat in the freezer. The product was then analyzed by 1H NMR and shown to be the desired 1-iodo-4-diazirine pentane product. (300 MHz, $CDCl_3$, δ): 3.16 (t, 2H, -CH_2-, #4), 1.7 (br s, 2H, -CH_2-, #3), 1.49 (t, 2H, -CH_2-, #2), 1.04 (s, 3H, -CH_3, #1).

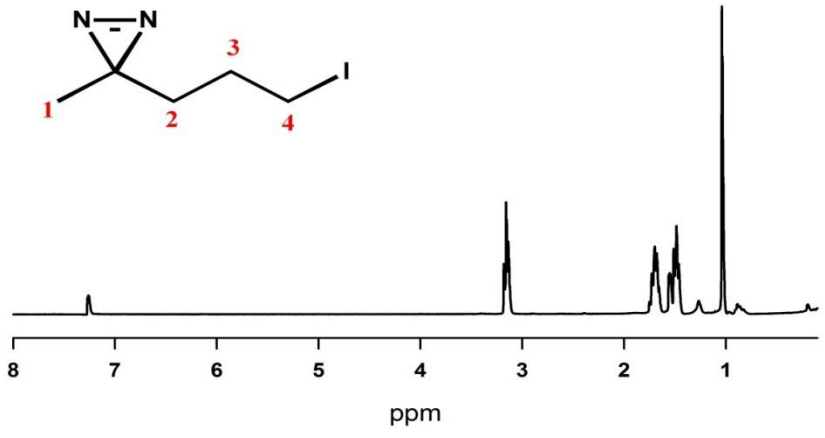

Figure 32: ^{1}H NMR spectrum of 1-iodo-4-diazirine pentane product.

5.2.7. Synthesis of Diazirine tagged peptides Peptides L*RGPADK and M*RGPADK were synthesized manually on Wang resin using standard Fmoc procedures.[8]

Pentapeptide GLGGK* was synthesized using the Liberty Blue peptide synthesizer as above, with the following changes. In place of Fmoc-Lys(Boc)-OH loaded Wang resin, Fmoc-Lys(Mtt)-OH loaded Wang resin was used and the N-terminal glycine residue was N protected by the BOC protecting group instead of Fmoc. While still attached to the Wang resin the methyl trityl protecting group was stripped from the lysine side chain by a 6 hour wash with 2mL acetic acid:trifluoroethanol:dichloromethane solution (1:2:7) with mixing. The exposed free lysine amine was then reacted with 6.7 µL of 1-iodo-4-diazirine and 6.7 µL of N,N-diisopropylethylamine in 200 µL of N,N-dimethylformamide at room temperature while mixing overnight. The photo labeled peptide was then cleaved from the resin via standard trifluoroacetic acid (TFA) procedures and separated from its dialkylated coproduct by HPLC on a CSH Xselect C18 (10 x 100 mm) semi-prep scale column(Waters Corporation). Solution A was HPLC grade water with 0.1 %TFA and solution B was HPLC grade acetonitrile with 0.075% TFA. A gradient elution profile was followed with 3 to 32% B over 26 minutes at 4.7 mL/min. Product was dissolved in acetonitrile:water (1:1) as a stock solution of approximately 1-2mg/mL.

Heptapeptide LRGPADK* was synthesized and purified in a similar manner with BOC protected Leucine used at the N-terminus.

N terminus alkylated pentapeptide *GLGGK and heptapeptide *LRGPADK were synthesized on the Liberty Blue peptide synthesizer using the standard fmoc protection scheme. After final fmoc deprotection, the solid phase tethered peptide with unprotected N terminus and fully protected side chains was reacted with the same diazirine containing cocktail as described above

and then cleaved from the resin and purified. These solutions were also stored at approximately 1-2mg/mL concentration in acetonitrile:water (1:1) solvent.

5.3. Results

Photopeptides GLGGK* and *GLGGK were combined with various neutral pentapeptides and basic heptapeptides. The stitching efficiencies for each combination are reported in Table 1. In the following section, an explanation for the metrics used to compare dimer stitching combinations is made and the particular case for the GLGGK* and GAMVG combination is used as an illustrative example.

Stitching Efficiency	GLGGK*			*GLGGK		
	MS2	MS3	Overall	MS2	MS3	Overall
GLLLG	5.50	31.5	1.74	13.0	12.1	1.57
GAMVG	10.5	38.4	4.03	12.9	16.8	2.18
PGLMG	7.16	33.8	2.42	23.7	16.2	3.85
GPLMG	6.23	49.3	3.07	18.9	23.5	4.44
GLPMG	5.46	39.4	2.15	11.9	20.6	2.45
GMLPG	8.39	57.1	4.79	13.0	30.6	4.00
KLGPADR	79.9	6.26	5.00	66.8	12.0	8.00
LKGPADR	85.1	8.22	7.00	74.2	9.33	6.92
LRGPADK	80.8	13.6	10.9	64.3	8.20	5.27
RLGPADK	70.0	8.53	6.00	58.7	15.8	9.10

Table 16: Stitching efficiencies for all GLGGK* and *GLGGK heterodimer combinations units are %.

In order to understand the results displayed in Table 1, the definition of each term are as follows. MS2 stitching efficiency refers to the proportion of product ions observed in the MS^2 photo reaction step which represent the loss of N_2 from the dimer complex. MS3 stitching efficiency refers to the proportion of product ions observed in the MS_3 CID step which were clearly representative of ions which had been stitched together by the carbene insertion reaction. The overall efficiency is the product of the MS2 and MS3 efficiencies and represents the proportion of proton bound ion dimers which performed gas phase covalent bond formation.

Consider, as an example, the case of the GLGGK* and GAMVG proton bound heterodimer, as is shown in the mass spectrum in Figure 3 below. The electrospray ionization mass spectrum is shown in part (a). This shows the very high ion signal from each of the components of the dimer (on the order of 10,000,000 counts) and the relatively small proportion of those components which aggregated into a dimer complex (shown in the inset) and survived the ionization process. This particular dimer was made without HPLC purification of the photopeptide and as such there is substantial presence in the ESI of the doubly alkylated coproduct photopeptide and some non-alkylated peptide substrate. Figure 3(b) shows the photo fragmentation spectrum of the dimer complex. A substantial amount of the complex absorbs photons and then falls apart without stitching as shown by the substantial presence of *m/z* 499.4 (GLGGK* - N_2 mass) in the spectrum. There is sufficient *m/z* 932.5 corresponding to loss of elemental nitrogen from the complex to show that some proportion of the proton bound dimer complex may have stitched.

The stitched peptides would be expected to fragment in a number of possible ways. A peptide backbone could break leaving the other peptide backbone intact, both backbones could break or nonspecific neutral losses could occur in any combination with backbone fragmentations. Capital letters are used to indicate fragmentation along the photopeptide backbone and lower case letters are used to indicate fragmentation along the backbone of the target peptide in order to distinguish between fragmentations which originated in one peptide backbone versus the other. In this particular case, y_2Y_2 would refer to a stitched dimer consisting of the VG residues from GAMVG and the GK* residues from GLGGK*. Intact peptides stitched to fragments would be indicated with an m or M*, i.e. mB_2 or b_4M^*.

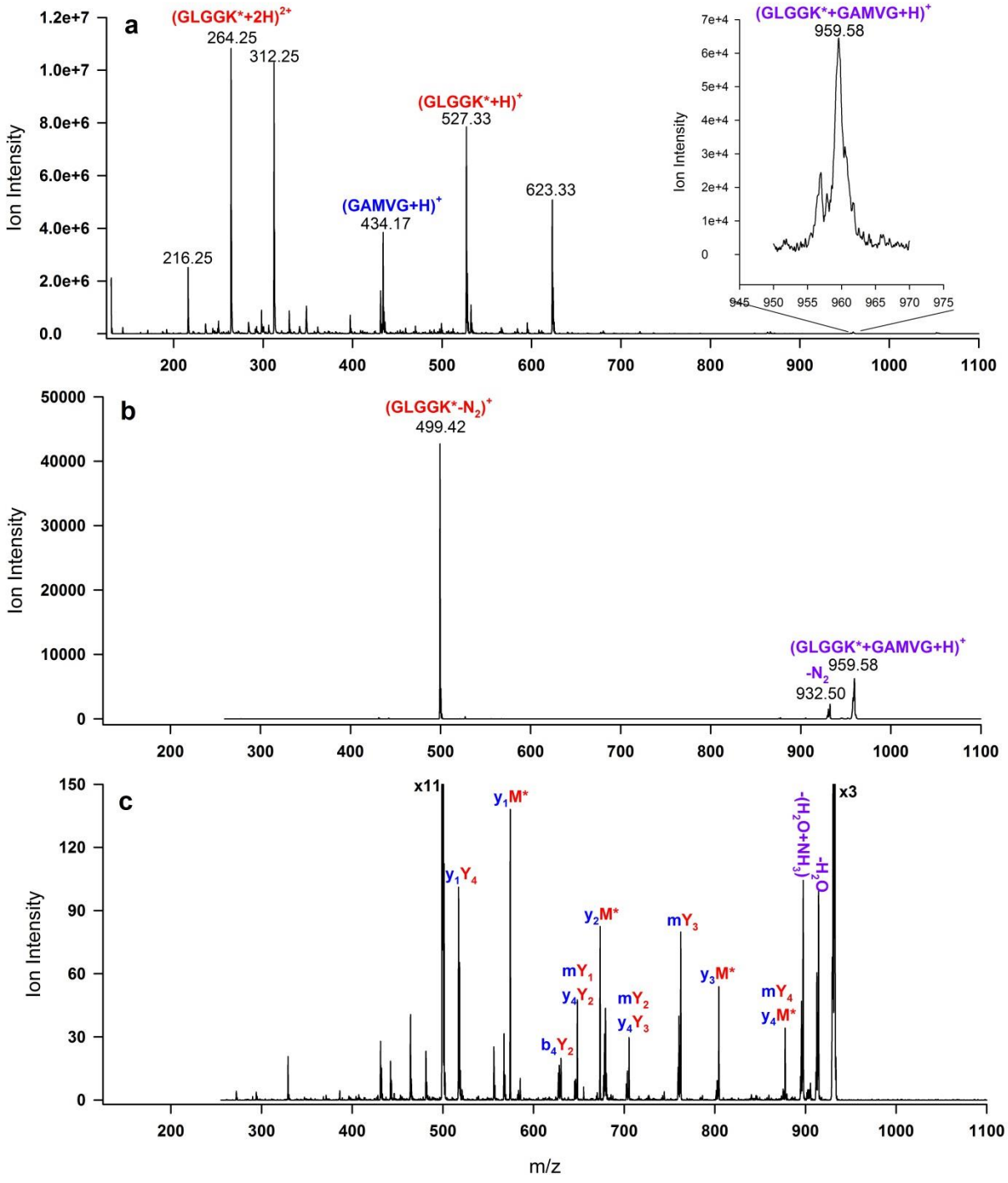

Figure 33: (a) MS[1] ESI Spectrum of GLGGK* and GAMVG mixed solution. (b) MS[2] UVPD mass spectrum of singly charged GLGGK*/GAMVG dimer. (c) MS[3] CID activation mass spectrum of photolyzed GLGGK*/GAMVG dimer complex at *m/z* 932.5.

Figure 3(c) is the CID product spectrum of the activation of the *m/z* 932.5 from the photo fragmentation spectrum. This shows definitive evidence that new bonds were formed through

photoactivation of the diazirine. Fragment *m/z* values between the mass of the monomer at *m/z* 499.4 and the dimer at *m/z* 932.5 only make sense as a product of a stitched complex. There is again a substantial presence of *m/z* 499.4 in the spectrum showing that not all of the parent ion consisted of stitched dimers, rather some substantial portion was still a non-covalent complex. However, this combination is an excellent demonstration of the types of stitched products that can be observed. There are combinations of backbone fragments (y_1Y_4, b_4Y_2), intact peptides with backbone fragments (y_1M^*, y_2M^*, mY_3, y_3M^*) and there are peaks which are nominally isobaric combinations (the mY_1 and y_4Y_2 have the same *m/z* at 648.4 as do the mY_2 and y_4Y_3 pair at *m/z* 705.4). These isobaric overlaps could likely be resolved with judicious application of isotopic labelling, if desired. There also are nonspecific water and ammonia losses which could have originated on either peptide.

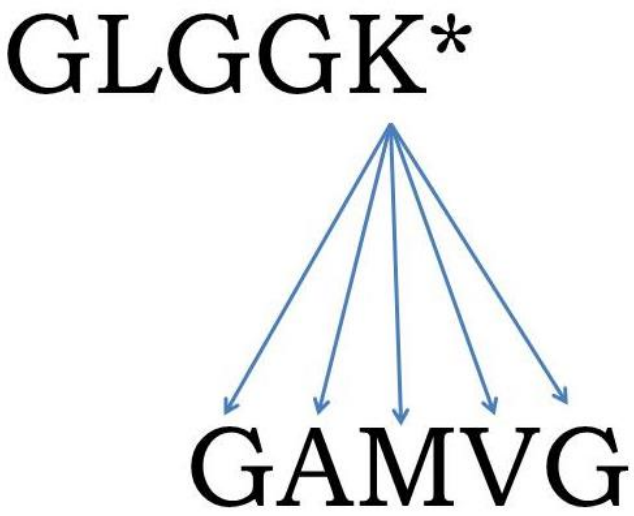

Figure 34: Cartoon showing possible sites at which photo lysine carbene insertion could take place.

To date, none of the combinations of photo and target peptides tried have yielded products which unequivocally localize the site of the bond insertion on the target peptide. Most combinations in fact show insertion at multiple sites; implying that the bond insertion is non-specific. The best approximation that we can support is to eliminate the locations where the

bond did not attach. Again using the case of GLGGK* with GAMVG, consider the cartoon drawing in Figure 4 above. The carbene which is exposed upon irradiation with 355nm light could potentially attach to any of the 5 residues in the target peptide or to either of the termini. Following stitching, and collisional activation of the stitched complex, fragments between the monomer and dimer masses are seen as in figure 3(c). Consider the b_4Y_2 fragment, which represents cleavage of the amide bond between Gly_3 and Gly_4 in the photopeptide as well as cleavage of the amide bond between Gly_1 and Ala_2 in the target peptide. This tells us that the bond formed by the carbene insertion reaction was not on Gly_1 residue or the N-terminus; it does not tell us where on the remaining portion of the target peptide the bond was inserted.

As a metric for gauging the relative localization of bond insertion sites the following measurement is proposed. The identified fragments shall be flagged with numbers corresponding to the particular residue or residues of the target peptide present in the fragment (ions with an intact target peptide will not be flagged and neither will fragments which represent nonspecific neutral losses). For example, the fragment b_4Y_2 would be flagged with 1, 2, 3 and 4. The fragment y_3M^* would be tagged with 3, 4 and 5. All identified fragments would be flagged in this manner and the total ion intensity for all fragments will be integrated. The integrated intensities would then be assigned to each of the flagged numbers and then combined. This would likely cause over counting of ion intensities but would give a general idea if the insertion site was localized to a particular residue or end of the target peptide.

GLGGK* with:					
	1	**2**	**3**	**4**	**5**
PGLMG	2.5	6.5	6.5	6.5	9.3
GPLMG	1.9	1.9	5.4	13.1	17.1
GLPMG	1.1	0.8	1.00	1.4	4.8
GMLPG	1.6	1.6	4.3	37.1	37.8
GAMVG	1.12	1.06	1.06	4.6	12.11
GLLLG	3.00	1.9	0	5.00	11.3

Table 17: Integrated values for each target pentapeptide flag site when mixed with GLGGK* photopeptide.

Consider the values shown for GLGGK* with GAMVG in the table above. The first three residues in the target peptide show similar abundances, but then position 4 (the valine residue) is 4 times the values of any of the first three positions and position 5 is 12 times the value of any of the first three positions. Clearly there is a preference for the more C-terminal portion of the target peptide in this case. Actually, when considering the rest of this table, it is interesting to note that all of the GLGGK* target peptides have the highest proportion of flagging for residue number 5 regardless of the sequence of the target peptide.

*GLGGK with:					
	1	**2**	**3**	**4**	**5**
PGLMG	0	0	1.4	2	2.8
GPLMG	1.5	3.5	4.9	6.3	7.1
GLPMG	0	0	11.1	11.1	12.4
GMLPG	0	1.1	2.7	16.9	16.9
GAMVG	0	0	3.7	6.11	8.6
GLLLG	1.77	0.21	1.23	1.97	2.8

Table 18: Integrated values for each target pentapeptide flag site when mixed with *GLGGK photopeptide.

When one considers the complementary case where the alkyl diazirine group is moved to the N-terminus instead of the C-terminal lysine we do not observe an inversion in the tendency for the C-terminal target residue to be the preferred site. Despite the change of the position of the diazirine photolabel the tendency still seems to be for the diazirine to be near the C-terminus of the target. This suggests that the charged secondary amine of the photo-lysine side chain residue and the secondary amine of the alkylated N-terminus both coordinate to the C-terminal carboxylate of the target peptides, regardless of sequence.

The pentapeptide GLGGK* was also mixed with several highly basic heptapeptides for two reasons. Firstly, the addition of additional basic residues to the combined dimer could result in a multiply charged peptide dimer complex which would enable the sequencing of the stitched dimer complex via ETD in addition to CID. This would potentially provide more specific and

complementary information regarding the stitch site. Secondly, by introducing an Arg residue into the combined complex, the location of the charging proton becomes well defined.

	GLGGK* with:						
	1	**2**	**3**	**4**	**5**	**6**	**7**
KLGPADR	0.51	0.68	1.2	1.2	1.2	1.2	0.66
LKGPADR	1.57	1.57	2.25	2.25	2.25	2.25	0.68
LRGPADK	0.58	0.58	0.58	0.58	0.58	0.32	0
RLGPADK	0	0	0.66	0.66	0.66	0.66	0.66
	***GLGGK with:**						
	1	**2**	**3**	**4**	**5**	**6**	**7**
KLGPADR	0.29	6.12	6.9	6.9	6.9	6.9	0.8
LKGPADR	0.27	0.27	1.3	1.3	1.3	1.3	1
LRGPADK	0	0	0.33	0.33	0.33	0.33	0.33
RLGPADK	0	0	0.53	0.53	0.53	0.53	0.53

Table 19: Stitching locations of GLGGK* and *GLGGK with highly basic heptapeptides.

As can be seen in Table 4 above, the information obtained from the flagging and integrating procedure for heptapeptides targets is less informative than in the cases of GLGGK* or *GLGGK with pentapeptide targets. There is no clear tendency for any particular residue or region of the target peptide to be preferred as a binding site. It is interesting to note here, that despite the presence of an arginine sequestering the charging proton, there is some evidence of fragmentations along the combined dimer complex in locations other than adjacent to the aspartic acid residue.

In an effort to achieve stitching within a doubly charged dimer complex, the photo lysine and N-terminally diazirine alkylated heptapeptides LRGPADK* and *LRGPADK were synthesized and combined with neutral pentapeptides. (The term “neutral” is here used to emphasize that the target peptides contain neither particularly basic nor particularly acidic residues and is not meant to imply charge state neutrality.) Also, photopeptides containing photo leucine and photo methionine (L*RGPADK and M*RGPADK) were synthesized to compare the

relative stitching efficiencies of the various photo labeled residues. The collated results are presented in Table 5 below.

Stitching Efficiency	LRGPADK*			*LRGPADK			M*RGPADK			L*RGPADK		
	MS2	MS3	Overall	MS2	MS3	Overall	MS2	MS3	Overall	MS2	MS3	Overall
GLLVK	87.3	0.79	0.69	89	4.11	3.7	86.2	6.21	5.4	83.9	9.63	8.1
GLLLG	35.8	2.53	0.91	49.6	3.96	2	30.2	10.8	3.3	32.3	17.9	5.8
GAMVG	28.7	2.97	0.85	31.4	6.55	2.1	20.3	17.6	3.6	22.3	23.5	5.2
PGLMG	41.7	3.81	1.59	45.8	11.1	5.1	34.5	12.2	4.2	31.9	14.3	4.6
GPLMG	35.0	6.90	2.43	38.6	7.6	2.9	24.5	16.7	4.1	29.6	21.3	6.3
GLPMG	23.3	3.39	0.79	26.2	27.4	7.2	20.7	21.4	4.4	22.5	28.8	6.5
GMLPG	28.0	3.86	1.08	36	7.66	2.8	22	18.3	4	20.8	23.8	5

Table 20: Photo Labeled heptapeptides with neutral pentapeptide dimer complex stitching efficiencies.

Unfortunately, these heptapeptide dimers were not very helpful in identifying stitching locations. All N-terminal photo tagged heptapeptide dimers when fragmented with CID only gave mB_6 and mB_6+H_2O fragments or nonspecific neutral losses with no other identifiable stitched fragments detected. In retrospect, it is not surprising that this position was the only fragment identified. It is well known that in CID of Arg containing peptides that the charge will be sequestered at the arginine and so the mobile proton model is not applicable.[12] In such cases, Arg containing peptides which also incorporated Asp have shown that Asp is capable of self-directing cleavage with its acidic side chain proton. In the case of the LRGPADK*, no stitched fragments were observed. Rather, upon collisional activation of the complex the only substantial fragment other than intact LRGPADK*-N_2 was the B_6 fragment, consistent with Arg proton sequestration.

Given the observed lack of sequencing information from the heptapeptides dimer complexes the only other attribute that can be considered is the stitching efficiencies. With the two exceptions of dimers containing PGLMG and GLPMG (highlighted in table 5 above) the stitching efficiencies do follow a pattern based on the particular diazirine chromophore. The C-terminal K* is the least efficient at stitching followed by the N-terminal alkylated LRGPADK, followed by photo methionine containing heptapeptides, followed by photo leucine containing

heptapeptides. This stitching efficiency can be summarized as LRGPADK* < *LRGPADK < M*RGPADK < L*RGPADK. Although this set only reflects one example, it can serve as a guide for improvement of stitching efficiencies in future experiments.

5.4. Discussion

These stitching experiments have provided some interesting results. Consider the four pentapeptide photo stitching targets which contain proline residues. Proline has the tendency under CID activation to cause preferential fragmentation at its N-terminal amide bond. In Table 5, the proline is moved sequentially down the chain. By doing so it was hoped that an effect would be observed in terms of the fragments generated by activation of the stitched product. Any stitching that was C-terminal to the proline would be observed and would hopefully be more easy to localize the bond stitching position. As well, the proline amide bond is typically considered to be more basic in the gas phase as shown by studies of proline containing peptides under CID activation. Enhanced cleavage at the proline residue implies that the mobilized protons tend to be present at that position in preference to others. As can be seen in the table 2 above, there was no trend in this manner. The tendency is for the diazirine to attach near the C-terminus regardless of the proline position within the chain. The apparent enhanced basicity of the proline amide bond is apparently insufficient to attract the charge from the photopeptide.

In some cases, fragments were identified in which the target peptide portion was only a single residue such as the y_1M* fragment from the GLGGK*/GAMVG complex. This means that the stitch is fairly well localized to a small area of the target peptide. Unfortunately, it cannot be more specifically localized. The ion intensity in that peak is less than 150 counts and so it is unlikely that mass isolating and fragmenting the y_1M* ion in an MS^4 experiment would work. This particular complex also had a b_4Y_2 ion present, indicating that the stitching position

is nonspecific and that we cannot guarantee a single unequivocal stitching position which provides doubt as to the likelihood of localizing a stitch in an intramolecular context.

CID activation of the putatively stitched dimer complex requires a substantially increased collision energy to dissociate the complex relative to the amount of energy needed to dissociate the non-stitched complex. A normalized collision energy (NCE) of 4 to 5 units were necessary to break up the noncovalent complex but, depending on the particular constituents of the complex, approximately 20 NCE were needed. A possibility that must be considered is that the newly formed covalent bond generated by the diazirine activation in the MS^2 step may actually the weakest bond in the complex and as such would be the first to dissociate upon collisional activation. If this was the case it would bring into question the viability of this method for conformational analysis of gas phase ions. However, given the increased amount of energy required to break up the complex after photolysis there is little doubt that some new bond was formed.

Our attempt to use highly basic photo peptides to increase the charge state of the noncovalent dimer complexes proved to be mostly fruitless. Only a very limited set of the various combinations of dimers resulted in a doubly charged dimer complex. Upon UV photo activation and subsequent fragmentation of the stitched complexes by collisions or electron transfer no new useful information was obtained (data not shown). These fragmentations followed the same pattern as the singly charged dimer complexes, only fragmenting in a very few spots and generating low abundance of stitched fragments.

It is worth noting here that the patterns for the stitching sites in the pentapeptide targets and the lack of pattern in the heptapeptide targets do imply something about the interactions between the photo peptides and their targets. The apparent orientation of the charged secondary

amine groups towards the C-termini of the target peptides, regardless of the position of the diazirine label show that the charge-dipole interactions between the C-terminal carboxylate and the alkyl-diazirine containing secondary amines are very important factors in the orientations of these peptides in the non-covalent dimer complexes. The fact that no observable trend was seen when the highly basic heptapeptides were used as targets emphasizes the import of this observation. With the charging proton sequestered in the arginine residue there is no charge-dipole interaction local to the diazirine containing group and as such no hint of localization of the binding sites.

5.5. Conclusions

Intermolecular gas phase bond formation was achieved using a newly synthesized photo lysine amino acid residue. Stitching locations were unable to be localized due to apparently nonspecific bond formation. Stitching efficiencies were in the range of 0.8 - 11 % showing an improvement over other reported gas phase covalent bond formation reactions efficencies[13], though less than other reported efficiencies.[14] Attempts to direct stitching location by placement of proline residues was inconclusive as the systematic movement of proline did not change the tendency of the most abundant stitched fragments to be located near to the C-terminus of the target peptide nor did it seem to localize the stitching site to the proline position. Use of highly basic photo peptides to increase dimer complex charge state was inconclusive due to sequestering of the proton charge at Arg residues. Use of a second (non-modified) lysine residue in place of Arg could be a fruitful avenue of exploration as the lysine side chain is basic enough to take a charge but not so basic as to fully sequester the charge and would be in competition with the photo-lysine residue. This would enable multiple dimer charge states while simultaneously providing greater sequence information. Regardless of the sequence of the target

peptide, there seems to be a preference toward the C-terminal portion of the target indicating the importance of the charge-dipole interaction in how the peptides are oriented towards each other in the non-covalent complex. Further studies are needed to confirm this phenomenon and further refine the localization of the bond insertion site. Isotopic labeling to distinguish isobaric fragments and computational modeling would also provide complementary evidence.

5.6. References

(1) Lin, S.; He, D.; Long, T.; Zhang, S.; Meng, R.; Chen, P. R. *J. Am. Chem. Soc.* **2014**, *136* (34), 11860–11863.

(2) Lin, S.; Zhang, Z.; Xu, H.; Li, L.; Chen, S.; Li, J.; Hao, Z.; Chen, P. R. *J. Am. Chem. Soc.* **2011**, *133* (50), 20581–20587.

(3) Zhang, M.; Lin, S.; Song, X.; Liu, J.; Fu, Y.; Ge, X.; Fu, X.; Chang, Z.; Chen, P. R. *Nat. Chem. Biol.* **2011**, *7* (10), 671–677.

(4) Korneev, S. M. *Eur. J. Org. Chem.* **2011**, *2011* (31), 6153–6175.

(5) Mihalca, R.; Kleinnijenhuis, A. J.; McDonnell, L. A.; Heck, A. J. R.; Heeren, R. M. A. *J. Am. Soc. Mass Spectrom.* **2004**, *15* (12), 1869–1873.

(6) Marek, A.; Pepin, R.; Peng, B.; Laszlo, K. J.; Bush, M. F.; Tureček, F. *J. Am. Soc. Mass Spectrom.* **2013**, *24* (11), 1641–1653.

(7) Marek, A.; Tureček, F. *J. Am. Soc. Mass Spectrom.* **2014**, *25* (5), 778–789.

(8) Carpino, L. A.; Han, G. Y. *J. Am. Chem. Soc.* **1970**, *92* (19), 5748–5749.

(9) Merrifield, R. B. *J. Am. Chem. Soc.* **1963**, *85*, 2149–2154.

(10) Going, C. C.; Williams, E. R. *Anal. Chem.* **2015**, *87* (7), 3973–3980.

(11) Shigdel, U. K.; Zhang, J.; He, C. *Angew. Chem.* **2008**, *120* (1), 96–99.

(12) Wysocki, V. H.; Tsaprailis, G.; Smith, L. L.; Breci, L. A. *J. Mass Spectrom.* **2000**, *35* (12), 1399–1406.

(13) Lee, S.; Valentine, S. J.; Reilly, J. P.; Clemmer, D. E. *J. Am. Chem. Soc.* **2011**, *133* (40), 15834–15837.

(14) McGee, W. M.; McLuckey, S. A. *Proc. Natl. Acad. Sci.* **2014**, *111* (4), 1288–1292.

Chapter 6.

Gas Phase Action Spectroscopy Measurements of New Diazirine based Photo-Lysine Chromophores and Organic Dye Molecules.

Abstract Photodissociation action spectroscopy is performed on two charge states of a diazirine labeled pentapeptide, GLGGK*, and the well-known organic dyes crystal violet and rhodamine B. When compared against theoretical modeling, the action spectra of the organic dyes show the Density Functional Theory method cam-B3LYP may not be suitable for these experiments. The experimental spectrum of Rhodamine B measured on a sector type mass spectrometer shows experimental evidence for the existence of a dark triplet state. The strongest absorbance band is a multiphoton process while a minor band at lower photon energies requires only a single photon. An explanation for this unexpected behavior is presented.

6.1. Introduction

It has become standard procedure when characterizing a new molecule to measure the absorbance bands of the molecule. Such information can lead to bonding clues when attempting to assign structure to a completely unknown species. In particular, spectroscopy reveals the presence of highly conjugated systems or perhaps the presence of heteroatoms. As such, gas phase studies are an integral part of the full identification of a molecule's true spectroscopic features and elimination of those due to an ion coordinated to several solvent molecules. As well, spectroscopy is completely orthogonal to other methods such as mass spectrometry or various chromatographies. An absorbance spectrum can tell the difference between two molecules with identical molecular weights. As an example, consider a photo-leucine amino acid molecule.

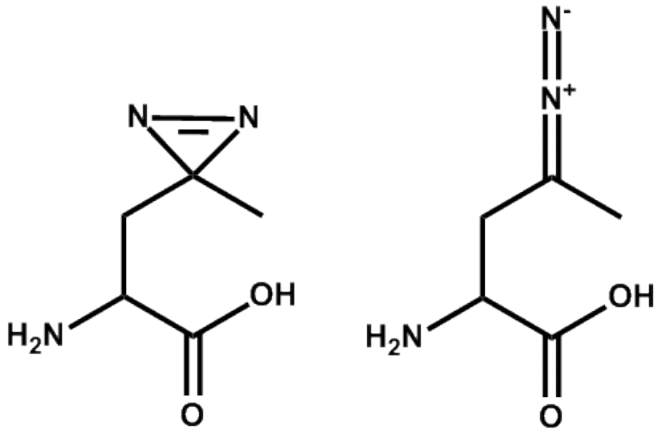

Scheme 10: Structures of isobaric molecules which could be distinguished via spectroscopy. Left: photo-Leucine, 2-amino, 4-(diazirine)pentanoic acid. Right: 2-amino, 4-diazo-pentanoic acid.

The photon absorbing group that gives the amino acid its name is a diazirine ring analogous to a cyclopropene consisting of two nitrogen atoms bound to each other and to the same carbon atom. See Scheme 1. If instead of being bound in a ring the nitrogens were bound linearly the resulting diazo group would have a very different spectrum. Diazo absorbs in the visible region while diazirine absorbs in the near UV. The two species would have the same mass to charge ratio in a mass spectrum and would likely be indistinguishable via ion mobility due to their similar sizes.

As a method for distinguishing between species, action spectroscopy is a truly powerful method. But, such a measurement is difficult from a practical standpoint. In a condensed phase measurement, light from the instrument is passed through the sample and the resulting decrease in intensity is measured. Following Beer's Law for extremely dilute samples, the typical gas phase ion cloud is too diffuse for measurement via the decrease of light intensity alone. Instead, the method of focus in this chapter looks at the "action" of the light. The ion of interest is irradiated with light and, if that energy is sufficient for bond cleavage the ions will fragment. Tracking these fragmentations as a function of the wavelength of the incident light give rise to action absorbance spectra. This method does not show absorption of non-fragment inducing photons.

The synthesis of photo-Lysine as described in chapter 5 coupled a known chromophore onto a new substrate with potentially complicating factors which may have effects on the chromophore's previously known absorbance band such as the observation that solvent molecules affect the absorbance characteristics of ionic and molecular species by as much as tens of nanometers.[1] . The intention for attaching this chromophore to lysine was to provide a new site for potential photostitching studies using the third harmonic of the Nd:YAG laser at 355nm. This diazirine chromophore, when incorporated into a purely nonpolar leucine or pseudo-methionine has a band maximum at 360nm. When it is localized near a charge carrying site this charge perturbation carries the possibility of a band shift and thus the effectiveness of the proposed stitching diminishes. Charge states are known to have effects on ion absorbances.[2] Diazirine groups have been shown to have different absorption band locations depending on the substrate to which they are coupled.[3] Attaching a diazirine tag to the lysine amine could potentially result in an absorbance band that is shifted relative to photo leucine or photo methionine. It is worthwhile then to measure the band maximum of the newly synthesized chromophore in the gas phase to ensure the utility and location of the absorbance bands.

Organic dye molecules have been known since ancient times and one of the most well studied classifications of species in the condensed phases. The study of these molecules in the gas phase is less complete. To date there have been no reports of gas phase spectra for the crystal violet molecule and only reports of gas phase fluorescence for rhodamine B.[4,5] Computational modeling of organic dyes still do not accurately predict experimental spectra and much effort is being made to improve these results.[6] In an effort to probe this problem, a C3 symmetric molecule (crystal violet) and an asymmetric dye molecule (rhodamine B) are considered.

This work also reports on the gas phase action spectroscopy of singly and doubly protonated GLGGK* in the region between 300 and 420nm. The action absorbance spectra of crystal violet and rhodamine B were measured in the region between 420 and 610nm. Scheme 2 below shows all three chromophores studied.

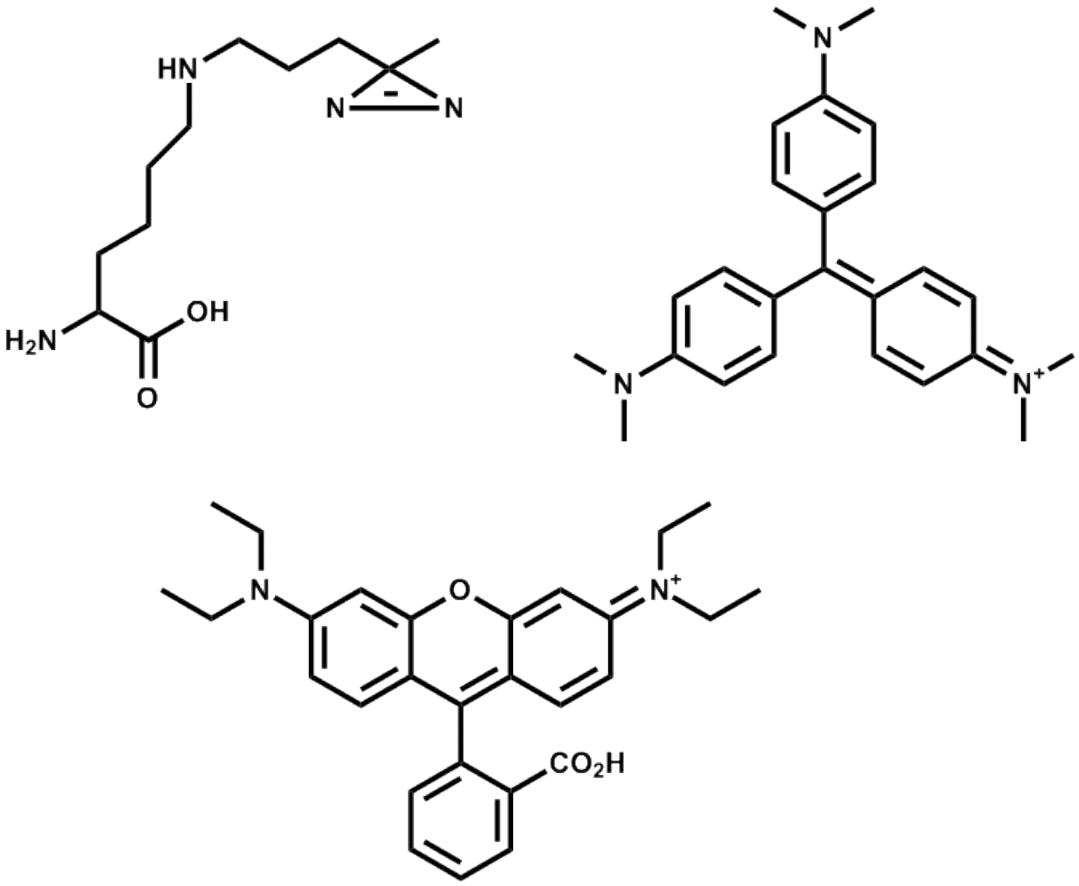

Scheme 11: The three chromophores studied using action spectroscopy in this chapter. Top left: Photo Lysine, Top Right: Crystal Violet. Bottom: Rhodamine B.

6.2. Experimental

6.2.1. Materials and Synthetic Methods All peptides used in this study were synthesized in house using standard fmoc[7] solid phase peptide synthetic methods.[8] The side chain of lysine was modified to photo-lysine by the procedures discussed chapter 5. Fmoc-Lys(Mtt)-Wang resin was purchased from Bachem USA (Torrance, CA). Most amino acids were purchased from Sigma-Aldrich with fmoc-protected N-termini and acid cleavable side chain protecting groups. Peptides

were synthesized on Wang resin purchased from Bachem America (Torrance, CA). Fmoc-Lys(Mtt)-OH was purchased from Chempep (Wellington, FL). Solvents were from Fisher and were reagent grade or better. Crystal Violet and Rhodamine B were purchased from Sigma-Aldrich. All chemicals were used as received.

6.2.2. Calculations All calculations were performed using the Gaussian09 suite of programs. Crystal Violet was optimized with the CAM-B3LYP density functional (DFT) method utilizing the 6-31+G(d,p) basis set. The energy of this optimized structure was then calculated with a higher basis set and the same DFT method (CAM-B3LYP/6-311++G(2d,p). Oscillator strengths for crystal violet were calculated as well. Rhodamine B singlet and triplet ground states were also calculated in this manner as well as the oscillator strengths for the singlet structure. The rhodamine B singlet and triplet structures were subjected to time dependent DFT and the energies of the first eight excited states for each multiplicity were ascertained.

6.2.3. Mass Spectrometry/Action Spectroscopy Peptides were dissolved in solutions of MeOH-H_2O-Acetic Acid (50:50:1) at 10 μM concentrations. Organic dyes were dissolved in the same mixed solvent as the peptides or alternatively in deionized water only, both cases at 10μM.

Solutions were electrosprayed into the vacuum interface of a Thermo Fisher LTQ:XL linear ion trap instrument with optional ETD module from a custom micro-electrospray source. The instrument was modified by replacing the rear vacuum manifold plate with a custom plate containing a transparent vacuum port. The ion volume for the ETD reagent generating ion volume had a 1mm hole drilled in the center, coaxial to the center of the ion trap.

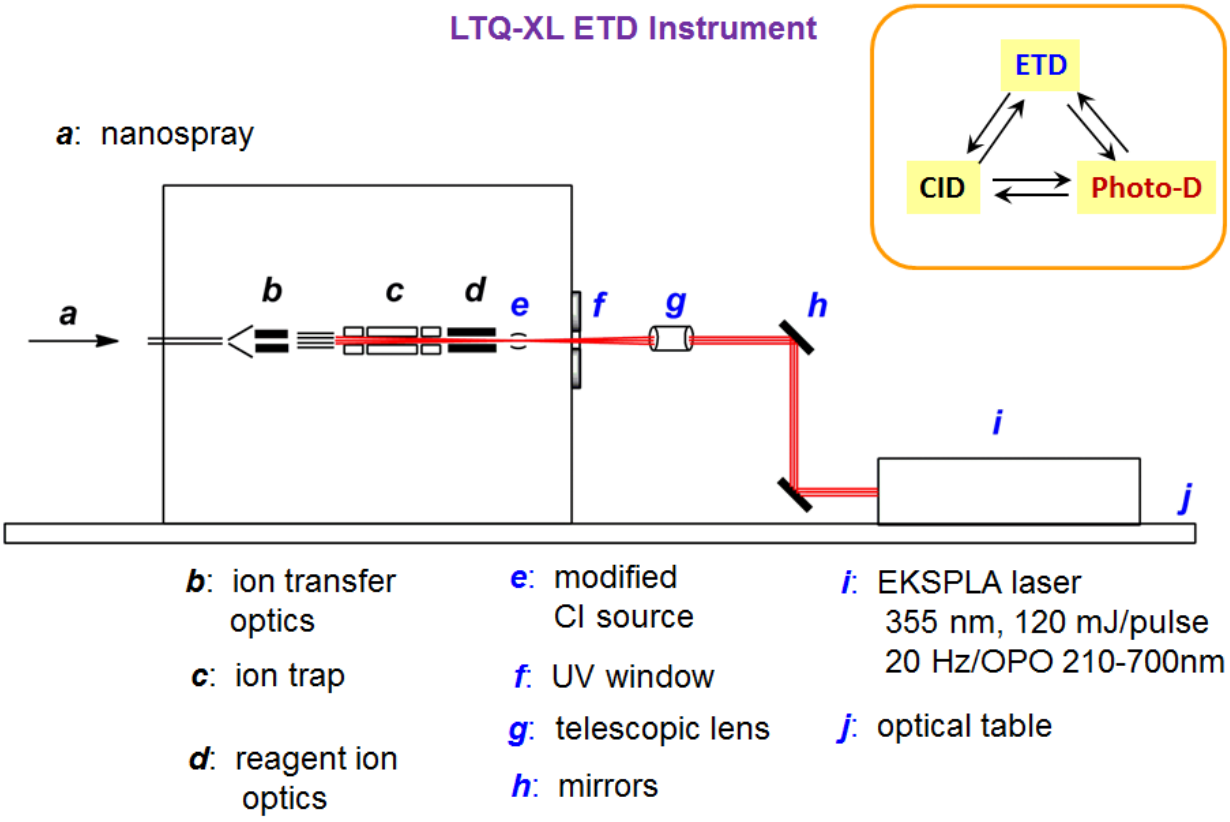

Figure 35: Schematic Diagram of the modified LTQ linear ion trap instrument.

Singly and doubly charged peptide ions were individually isolated in the trap using an isolation width of 2 *m/z*. The peptides were subjected to ETD (for 200ms) and CID (for 30ms at 14 normalized collision energy units) fragmentation to verify sequence. The isolated peptide ions were then stored in the trap for 1000ms and irradiated with light from an optical parameter oscillator (OPO) PG140 series from Ekspla (Vilnius, Lithuania) pumped by a pulsed Nd:YAG laser operating at 20Hz with a 3-6ns pulse duration. Fragment ions were then resonantly ejected from the trap and detected. The changing relative amounts of ions were monitored as a function of the wavelength provided by the OPO and used to generate action absorbance spectra. All mass spectra recorded in the visible wavelength region were recorded with the OPO detuned such that no pulse of photons registered as more than 3 mJ on the power meter.

A homebuilt sector type mass spectrometer, see instrument schematic in Figure 2, was also used to generate action absorbance spectra. This instrument consists of an electrospray ion source followed by a series of skimmers, lenses and a 14 pole ion guide leading to a octopole trap where ions are stored for 25 milliseconds before being extracted in bunches and then accelerated through a 50kV potential. The ions of interest were then mass selected by a bending magnet before passing through a region where they were allowed to interact with light from an OPO whose description is similar to that above.

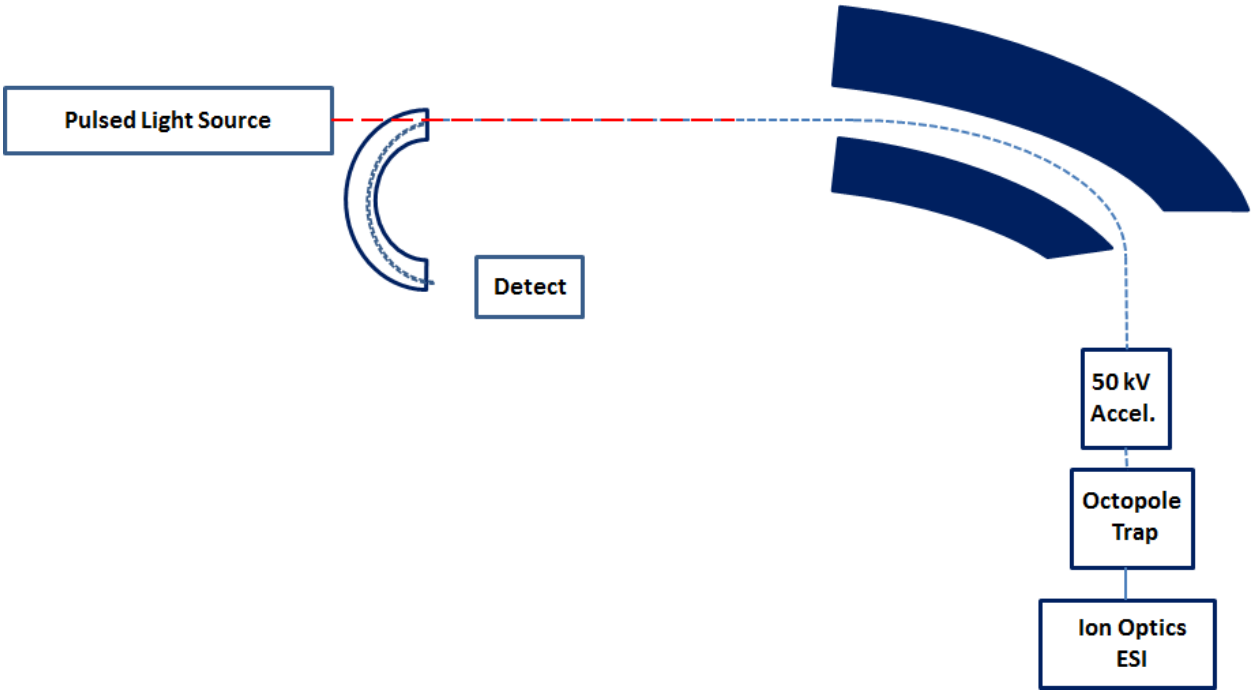

Figure 36: Schematic of sector type mass spectrometer used in these studies.

Product ions were then analyzed with an electrostatic analyzer and counted by a channeltron detector. Laser light was only allowed to interact with every other ion bunch to reveal the true photo induced fragment ions through comparison between LASER ON and LASER OFF data. In cases where the expected absorbance was between 300 and 420nm a homebuilt add-on module was used which mixed the 1064nm fundamental with visible light output from the OPO

to increase the intensity of the laser pulse as output from the OPO in this region is typically much weaker than in other regions.

The laser light of the OPO was fixed at the center of the absorbance bands for each charge state of GLGGK* and each band for the organic dyes and the fragment ion intensity was monitored as a function of the applied laser power. A series of absorbtive filters were placed in the laser beam path to scale the applied laser power.

6.3. Results and Discussion

6.3.1. GLGGK* Action absorbance spectra generated on the sector based instrument for the two different charge states of photo lysine containing peptide GLGGK* are shown in Figure 3. Figure 3(a) shows the action absorbance data monitoring the formation of the $\boldsymbol{y_3}$-N_2 fragment ion from the doubly charged peptide cation precursor (black) and the loss of N_2 fragment channel from the singly charged peptide cation. Figure 3(b) shows the results of smoothing this data for clarity using a weighted polynomial regression function.

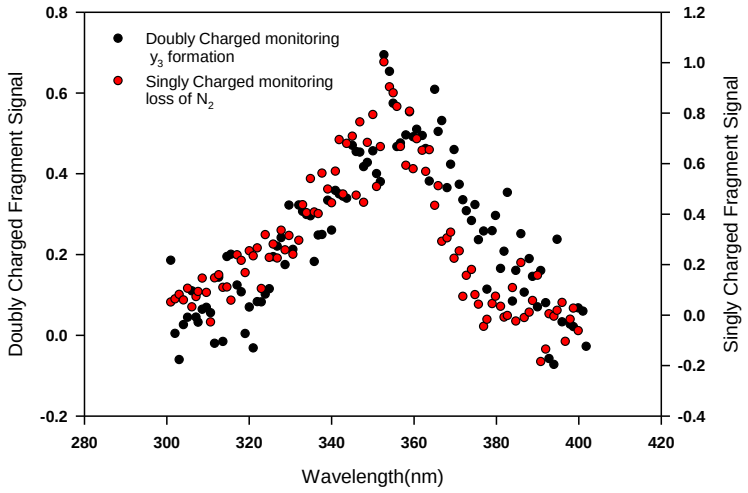

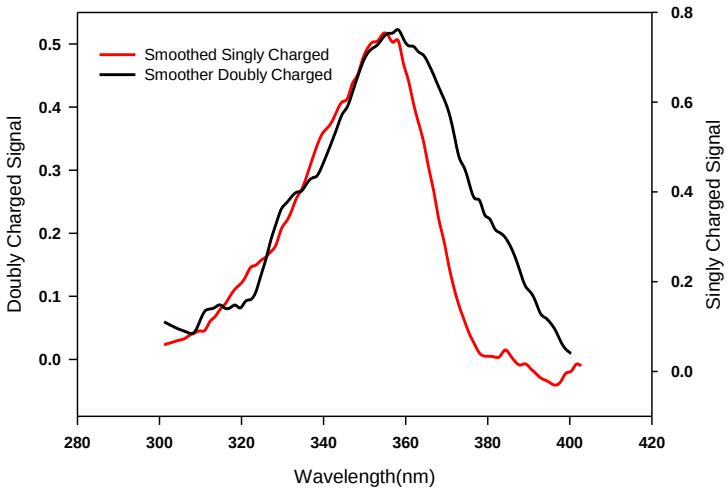

Figure 37: (a) TOP: Overlaid action spectra of singly and doubly charged GLGGK* peptide ions. (b) BOTTOM: Overlaid action spectra of GLGGK* peptide ions with smoothing applied for clarity.

What can be seen from this data is that charge state plays a minimal role in the location of the band maximum for the GLGGK* peptide. The center of the maximum for the singly charged GLGGK* ion is only shifted by approximately 5nm from the center of the doubly charged ion. The doubly charged ion does show a wider band than the singly charged ion. Power dependence measurements, shown in Figure 4, show that both charge states of GLGGK* absorb single photons in the 360nm band.

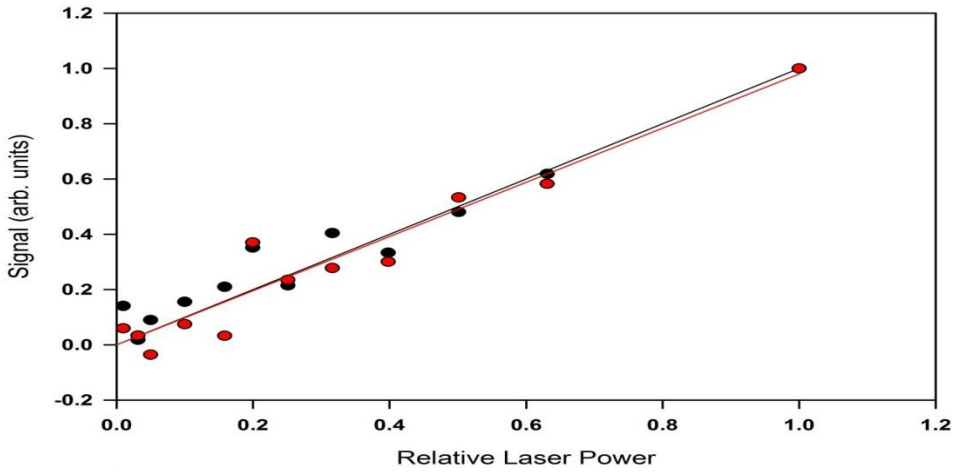

Figure 38: Power dependence plots for singly and doubly charged GLGGK* peptide ions with linear fits applied. Red: Singly Charged, Black: Doubly Charged

Photo induced dissociation (PID) mass spectra were recorded by setting the magnetic field of the bending magnet to permit transmittance of the singly or doubly charged precursor ions. The same LASER ON and LASER OFF difference measurements were carried out with the wavelength of the laser system fixed on the wavelength of the absorbance band maximum. The voltages of the electrostatic analyzer were then progressively varied such that the mass to charge ratio which was allowed to pass through varied from 10 to 510 *m/z* in the case of the singly charged GLGGK* ion in steps of unit mass to charge. In the case of the doubly charged precursor ion, the *m/z* scan range was 10 to 254 *m/z* and 270 to 530 *m/z* so as to prevent exposing the sensitive channeltron detector to the very intense parent ion beam. As can be seen in Figure 5 below, the singly charged GLGGK* showed only one fragmentation channel, loss of 28 *m/z*, assigned as loss of elemental nitrogen from the diazirine ring.

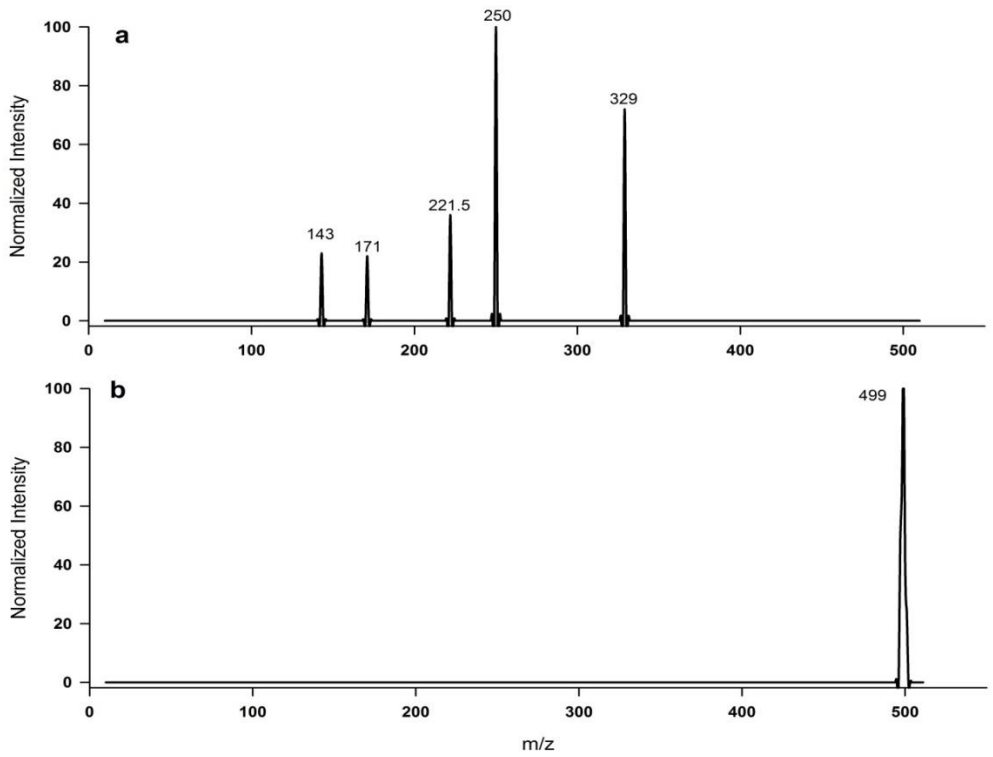

Figure 39: PID mass spectra of GLGGK* precursor ions. BOTTOM: PID MS of singly charged GLGGK*. TOP: PID MS of doubly charged GLGGK*.

Doubly charged GLGGK* showed several channels most of which show loss of N_2 followed by additional fragmentation. The primary fragmentation channel observed is *m/z* 250 which corresponds to the singular loss of N_2 from the doubly charged precursor ion. The second most intense product ion was assigned as being the $\boldsymbol{y_3}$ ion following the loss of N_2. There were significant amounts of $\boldsymbol{b_2}$ ion which represents the complementary N-terminal fragment to the $\boldsymbol{y_3}$. This $\boldsymbol{b_2}$ could also lose carbon monoxide, CO, to give rise to the abundant $\boldsymbol{a_2}$ product ion. There was a minor doubly charged ion which corresponded to the loss of N_2 and the N-terminal glycine residue. Finally, a very minor product ion corresponding to the mass to charge of $\boldsymbol{y_1}$**-2H** was observed as well.

In summary, the GLGGK* did not show substantial spectroscopic differences between charge states. Both the singly and doubly protonated peptide ions absorb photons very close to the 355nm wavelength of the laser light. The doubly charged ions did show a much greater tendency to fragment upon absorption of the same photon. This could be explained by considering Coulombic effects. Breaking a backbone covalent bond between the two charges would be assisted by the extra repulsive energy from the charges mutually repelling one another. This would result in a substantially reduced energy barrier for the cleavage of these bonds. In addition, the Coulomb repulsion between the fragments would lower the energy barrier for dissociation of the complex following bond cleavage.

6.3.2. Crystal Violet Action absorbance spectra for crystal violet were recorded on both the ion trap and sector type instruments. The crystal violet compound is a permanent ion, needing no charging proton from the electrospray process to form singly charged ions. Crystal violet was electrosprayed from both a composite solvent of methanol and water as described in the experimental section above as well as from deionized water. There was no observed difference

in the ions introduced from either solvent. The canonical structure of crystal violet is shown in Scheme 2 above. Note that the calculated structure shows a threefold symmetry with the delocalized charge centered at the central carbon atom rather than out at one of the amine nitrogen atoms. The parent crystal violet ion was mass selected with an isolation width of 2 *m/z* to include any isotopologues and then subjected to PID by varying wavelengths from the OPO. The PID mass spectrum recorded at 550 nm is shown below in Figure 6 as an example of the fragmentations induced. The gas phase extinction coefficient for crystal violet is evidently very high as this example spectrum was recorded as a single pulse experiment and as can be seen the single pulse lead to extensive fragmentation and a rich spectrum of fragments. Fragments *m/z* 356, 340, 311, 284, 268, 239, 235, and 165 corresponding to losses of 16, 32, 61, 88, 104, 133, 137 and 207 mass units, respectively, were selected to be monitored for generation of action spectra intensities.

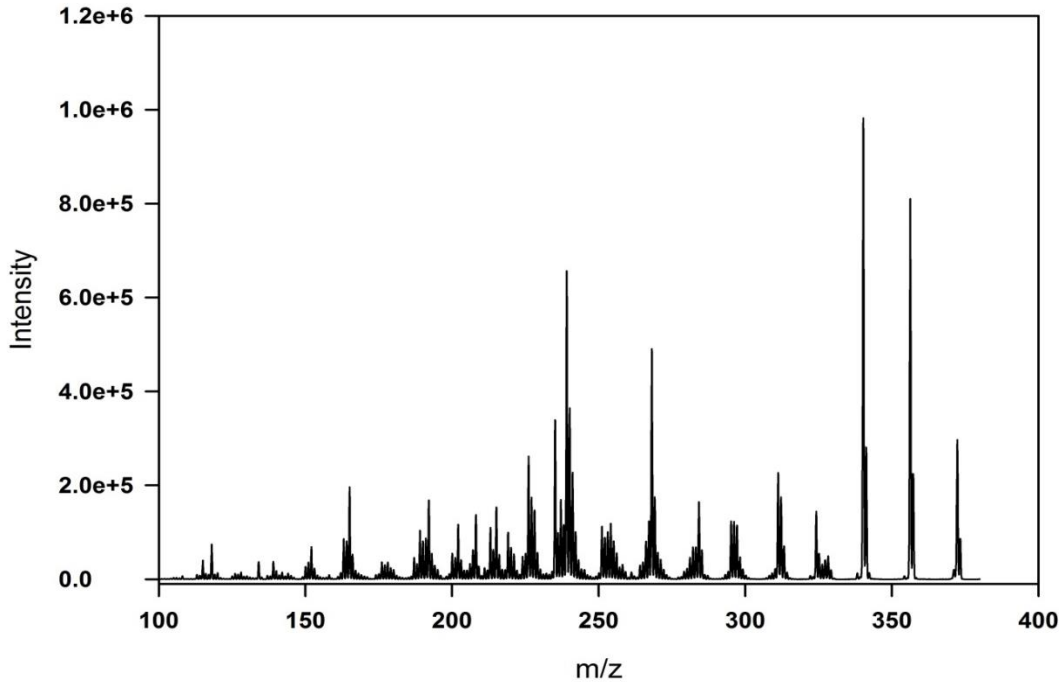

Figure 40: PID mass spectrum of Crystal Violet generated on LTQ instrument. Precursor ions were trapped for 100 ms and irradiated with 1 pulse at 550nm.

The resulting mass resolved action spectrum of crystal violet is shown in the figure below.

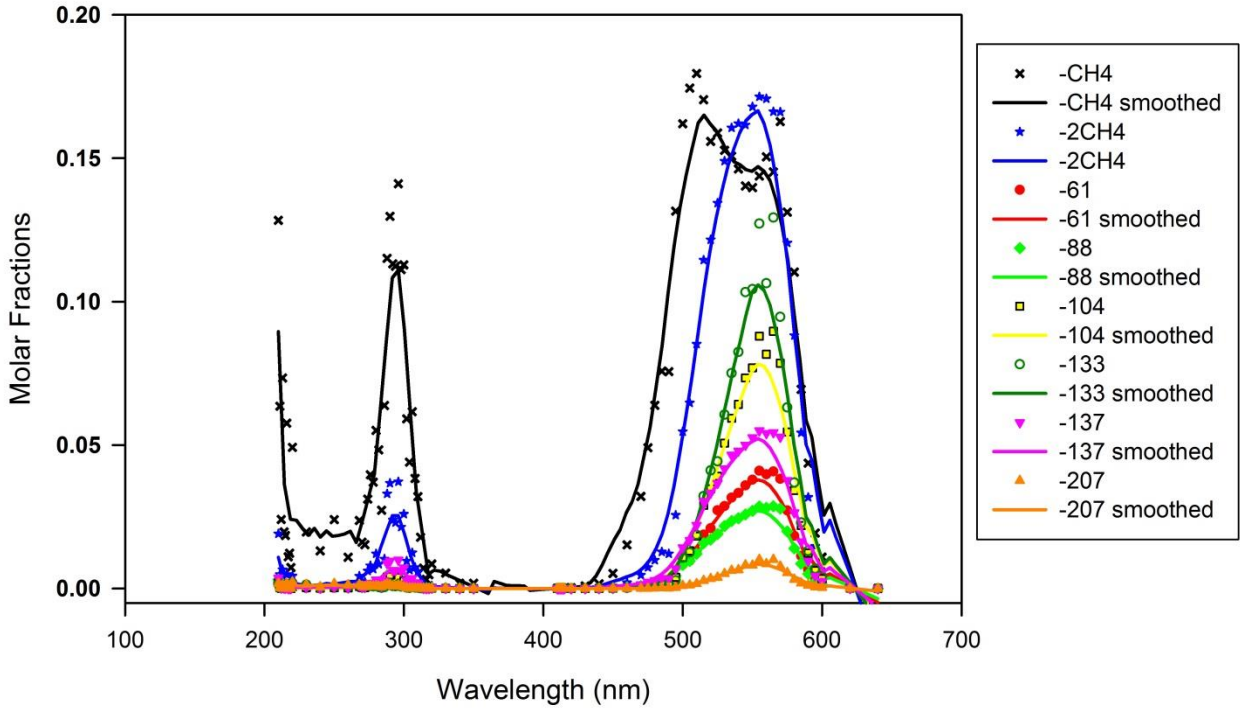

Figure 41: Mass resolved action spectrum of Crystal Violet from LTQ instrument.

This mass resolved action spectrum above shows some very interesting traits. Firstly, it appears to show that the fragment channel corresponding to losses of two methane molecules is initiated at longer wavelengths than that of single methane loss. This behavior would be counter intuitive when one remembers that longer wavelengths correspond to photons of lower energies. Loss of two methane molecules from an ion should be a higher energy process than the loss of a single methane. Also, note the asymmetry of the single loss of methane band. This is experimental evidence that there are likely two strong absorbance bands close together in the 500 - 600nm region. The shape of the absorbance bands mirrors that of crystal violet in the solution phase(data not shown), but is substantially shifted towards the blue.

In order to verify the results of this experiment, the action spectra of the crystal violet ions were also ascertained using the sector based instrument described above. Due to the nature of the sector instrument, it is not possible to simultaneously monitor the relative abundances of

fragment ions from a single pulse measurement. Instead, each fragment ion is monitored independently and as such the instrument is not suitable for comparing the relative amounts of fragment ions. Instead the useful comparisons will be the width of the absorbance bands and the locations of the centers. PID fragments identified on the sector instrument include *m/z* 356, 340, 328, 251, and 134. The action spectrum from the sector based instrument for crystal violet monitoring the single and double losses of methane are shown in Figure 8 below.

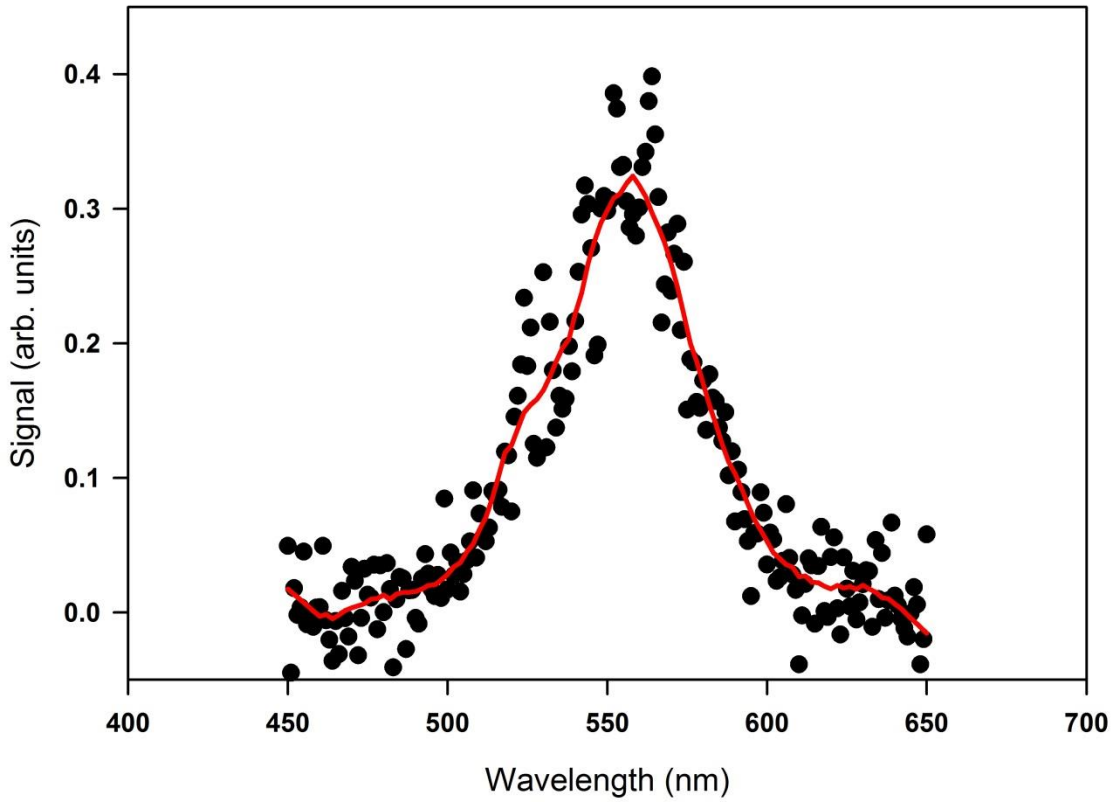

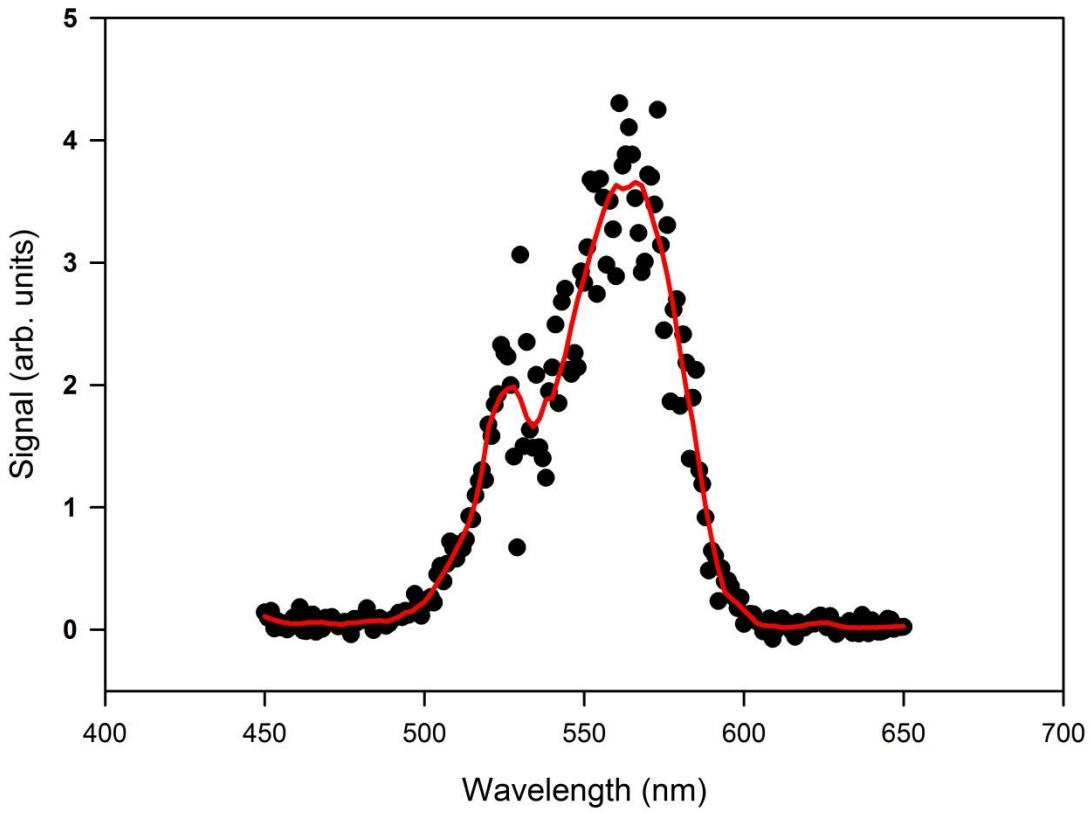

Figure 42: TOP: Action spectrum of Crystal Violet monitoring the loss of a single methane molecule. BOTTOM: Action spectrum of Crystal Violet monitoring the loss of two methane molecules.

The single loss of methane can be seen in the figure above. The absorbance band is centered around 560 nm and can be seen to have some asymmetry as there appears to be a small shoulder on the shorter wavelength side of the maximum. The action spectrum monitoring the double methane loss is shown below. As can be seen from the plot, the center of the absorbance band is again at 560 nm and there is more evidence of a small shoulder on the shorter wavelength portion of the band. These data are in agreement with the data measured on the ion trap instrument in the location of the absorbance bands and there is some evidence that the asymmetry measured on the ion trap is also showing up in the sector instrument. The onset of the absorbance bands for the single and double methane losses are also at approximately the

same position so this provides no evidence for or against the apparent preference for double methane loss.

The oscillator strengths from cam-B3LYP/6-311++G(2d,p) for crystal violet are shown in the table below. As can be seen upon inspection, the calculated wavelengths are in a stark disagreement with experimental results. Given that the values found from both the ion trap and sector based instruments match up, this calls into question the accuracy of the DFT method as a spectroscopic predictor. A difference of over 100nm (0.64eV) between the strongest band from theory and experiment is substantial. As well, it is worth noting that the observed band around 300nm is not predicted at all by the calculations. The apparent double band observed in experiment at the longest wavelength peak is not even hinted at in the calculated results either.

Crystal Violet Calculated frequencies and Oscillator Strengths cam-B3LYP/6-311++G(2d,p)				
Wavelength (nm)	**F**		**Wavelength (nm)**	**F**
435	0.8235		233.1	0.0576
434.98	0.8246		233.08	0.059
295.07	0.0025		228.96	0.1179
295.05	0.0025		228.93	0.1182
293.49	0		223.98	0.0549
278.48	0.0009		218.43	0.0176
262.97	0.0918		218.42	0.0176
262.96	0.0922		213.75	0.0132
248.44	0.0481		213.74	0.0133
235.22	0		213.41	0.0019

Table 21: Frequencies and Oscillator Strengths from cam-B3LYP6-311++G(2d,p) for crystal violet.

Power dependence measurements for the single methane loss from crystal violet and double methane loss from crystal violet were made. Figure 9 below shows the power dependence for all monitored fragments on the sector type instrument. What can be seen is that all fragments monitored, except for *m/z* 340, are fit by a third degree power function. The double methane loss is not able to be fit by a third degree power function and instead needs to be fit by a fourth degree power function. Clearly, the single and double methane losses require different numbers

of photons. It can be concluded then that the loss of two methane molecules from crystal violet is not happening with less energy than the single methane loss. Rather it takes an additional photon at the same wavelength to induce the additional methane loss.

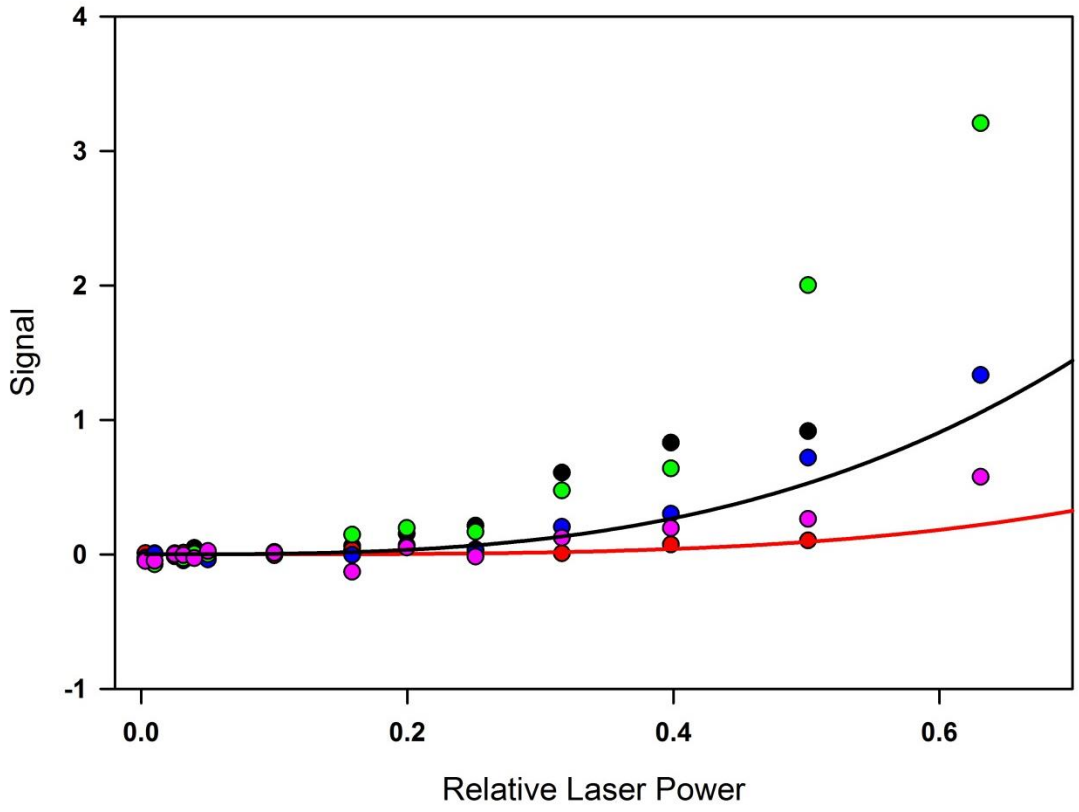

Figure 43: Power dependence plots for Crystal Violet following various fragmentation channels. BLACK: Single methane, loss of 16. RED: Double methane, loss of 32. BLUE: Fragment *m/z* 328. GREEN: Fragment *m/z* 251. PINK: Fragment *m/z* 134.

There are noteworthy differences between the data recorded on the ion trap and sector instruments. First, one can note that the shapes of the absorbance bands are different. The loss of methane on the ion trap instrument gives rise to an asymmetric peak giving the appearance of two closely located peaks superimposed upon each other. The absorbance band of the loss of methane on the sector instrument appears to be mostly a symmetric peak with a small shoulder on the shorter wavelength side, rather than looking like two overlapping, but separate bands. Second, the number and identities of fragment ions identified differ between the two instruments. As can be seen in the PID mass spectrum from the ion trap above, there are dozens of possibly

identifiable peaks whereas the sector instrument only observed 5 fragments. Also, three of the fragments identified in the sector instrument do not appear in the mass spectrum from the ion trap.

These differences can be explained by considering the nature of the two different instruments. The sector instrument involves ions at very high kinetic energies (50 keV per charge) and involves a very short timescale, on the order of microseconds. The sector instrument also maintains a vacuum pressure of approximately 10^{-6} Torr. The ion trap mass spectrometer has a time scale that is much larger than the sector instrument. In this particular experiment, ions were trapped for 100ms prior to being ejected from the trap and detected. This difference in timescale would allow many dissociations to occur that might not have had the opportunity to occur in the sector instrument. Also, the ion trap uses a bath gas at a few milliTorr[9] of pressure to collisionally cool the ions for storage, and as such the ions in the trap are subjected to energy transfer collisions which could both excite or de-excite the ions. Considering these two factors, it is quite reasonable to see differences of these type between different instruments.

6.3.3. Rhodamine B Action spectra of rhodamine B were collected using the linear ion trap instrument. A PID mass spectrum from the ion trap instrument is shown in Figure 10 below. The ions were trapped for 200ms and subjected to 3 pulses from the OPO at 520nm. The dominant product ion was 44 mass units below the parent ion and was assigned as being due to the loss of CO_2 from the carboxylic acid group.

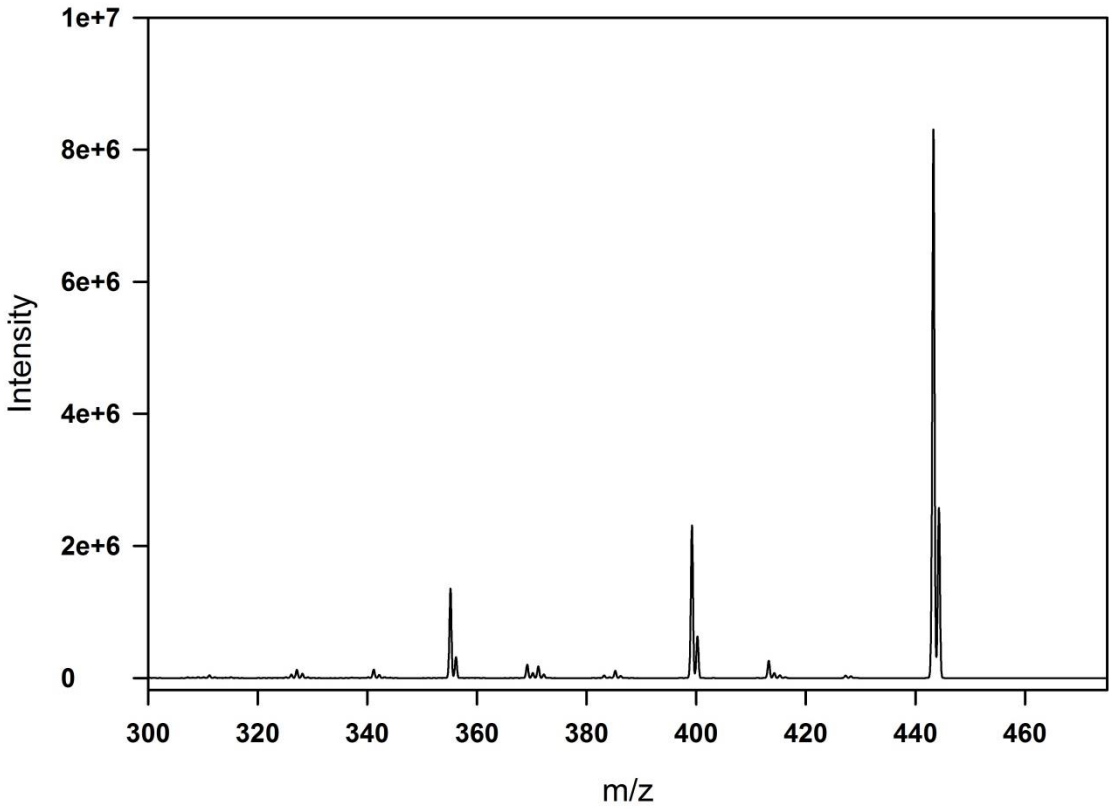

Figure 44: PID MS from LTQ instrument. Ions were trapped for 200ms and subjected to 3 laser pulses at 520nm.

Three fragment ions were identified with sufficient signal strength for action spectra monitoring. Fragment ions *m/z* 413, *m/z* 399 and *m/z* 355 were monitored. The mass resolved action absorbance spectrum can be seen below in Figure 11. The ion trap derived action spectrum shows four distinct peaks. Maxima are located at 280, 350, 480 and 520nm. In the ion trap, no observable fragmentation occurred above 560nm. As in the case of crystal violet, the rhodamine B spectrum is very similar to that in the solution phase but again is shifted towards the blue. The loss of CO_2 was the most abundant product at all wavelengths surveyed.

The calculated results for absorbance frequencies and oscillator strengths for rhodamine B are shown in Table 2. Again, it can be seen that there is extremely poor agreement between experimental and theoretical results. Clearly, this DFT method needs improvement before confidence can be placed in its spectroscopic predictive abilities. The experimentally observed

double bands at 480 and 520 nm are not present in the calculated bands, nor is there even a hint of the 350 nm UV band.

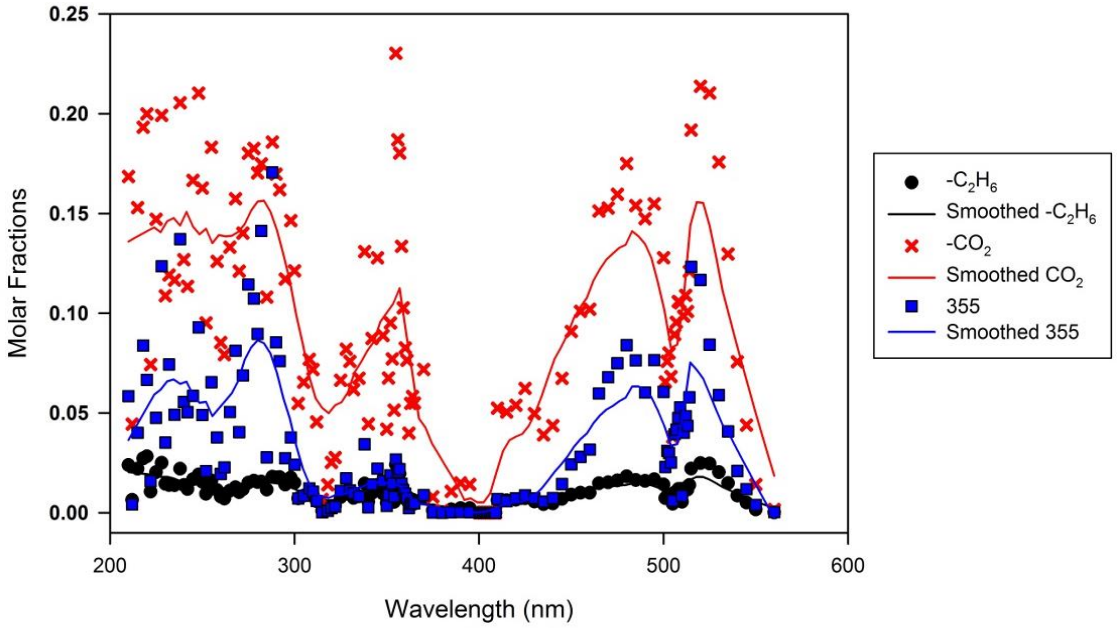

Figure 45: Mass resolved action spectra from Rhodamine B. BLACK: Loss of Ethane *m/z* 413. RED: Loss of CO2, *m/z* 399. BLUE: Fragment *m/z* 355.

Rhodamine B Calculated frequencies cam-b3lyp/6-311++G(2d,p)		
Wavelength (nm)		**F**
423.3		1.0092
337.78		0.0074
281.29		0.0632
280.59		0.0073
268.52		0
263.33		0.2397
261.09		0.0114
253.72		0.2555
244.17		0.0092
242.33		0.0071

Table 22: Frequencies and Oscillator Strengths from cam-B3LYP/6-311++G(2d,p) for Rhodamine B.

The action spectrum of rhodamine B, monitoring the loss of CO_2, was measured using the sector instrument as well, shown below in Figure 12. The sector instrument again showed two absorbance bands in the region from 420 nm to 650 nm. There was good agreement with the

location of the band maxima between the two instruments and as with the crystal violet, the relative heights of the absorption bands were different. Between trials, the instrument conditions were adjusted to verify the best timing between laser pulse and ion bunch arrival. With the improved timing, too many photo product ions were formed and the channeltron detector was becoming saturated. In order to reduce the overall ion signal, the action of rhodamine B was measured with a 0.6 OD filter in place. This revealed a previously unknown third absorbance band in the 420 - 650nm range, also seen in Figure 12.

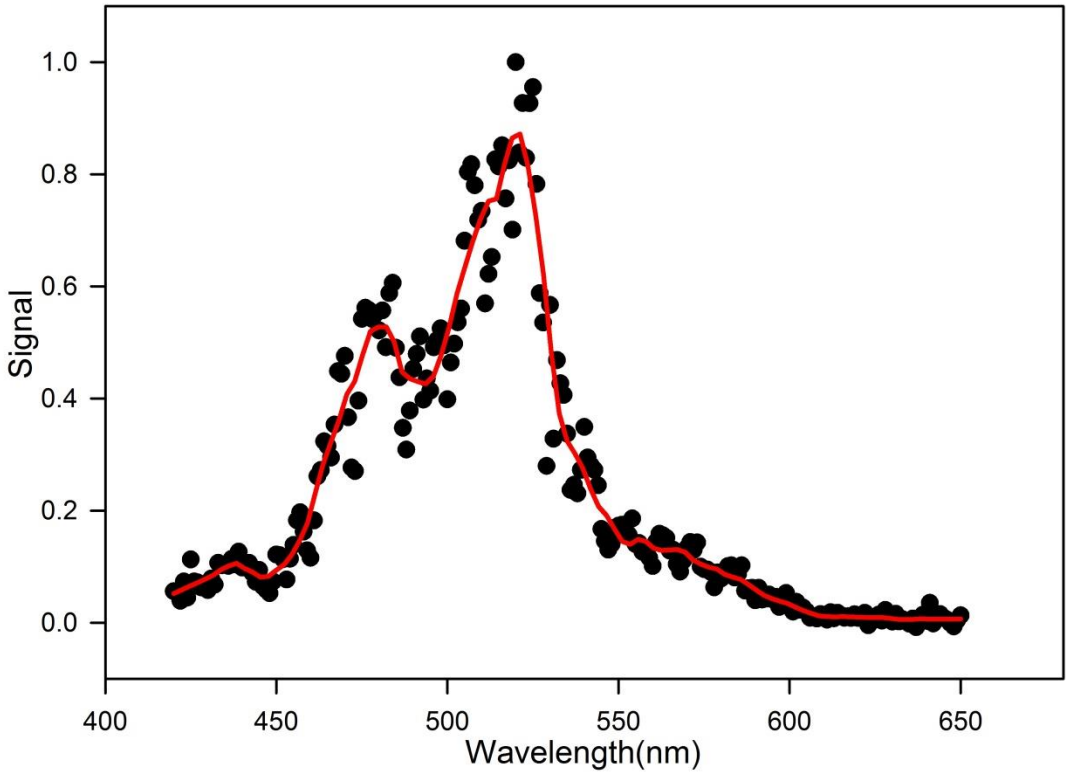

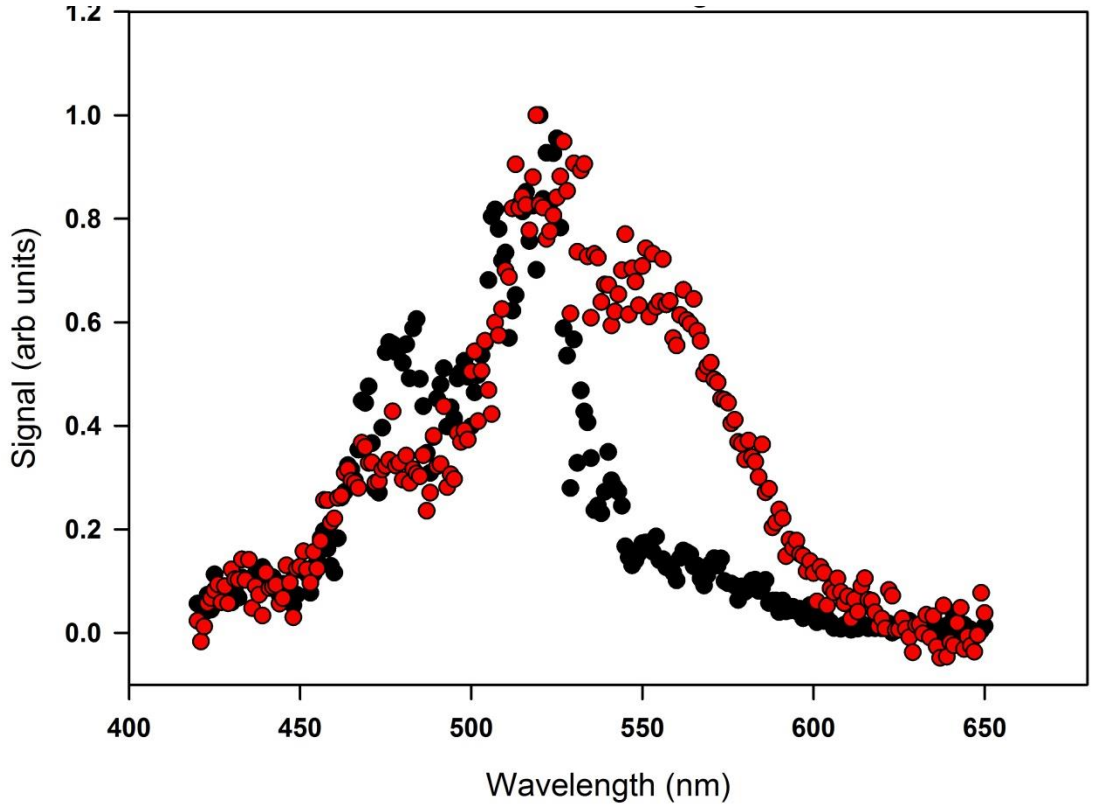

Figure 46: (a) Action spectrum of rhodamine B monitoring CO2 loss fragment channel. Two band maxima at 480 and 520nm are clear. (b) Action spectrum of CO_2 loss from rhodamine B with and without filter. BLACK: Unfiltered. RED: Filtered.

Power dependence measurements provide an explanation for this behavior. When measured at 520nm, the power dependence on the formation of the *m/z* 399 fragment shows a multiphoton process. When measured at 560 nm, the dissociation of rhodamine b to form *m/z* 399 is shown to take only a single photon, as can be seen in Figure 13. This poses an interesting question…why does a single lower energy photon cause dissociation when it takes multiple higher energy photons to form the same product? Also interesting is the presence of measurable absorbance (meaning fragmentation) above 560nm on the sector based instrument. As noted before, there were no detectable photo product ions measured in the ion trap above 560nm. It is likely that the helium bath gas in the ion trap would collisionally de-excite ions and the energies of photons at 560nm and longer would be insufficient to overcome the cooling effect of the bath gas.

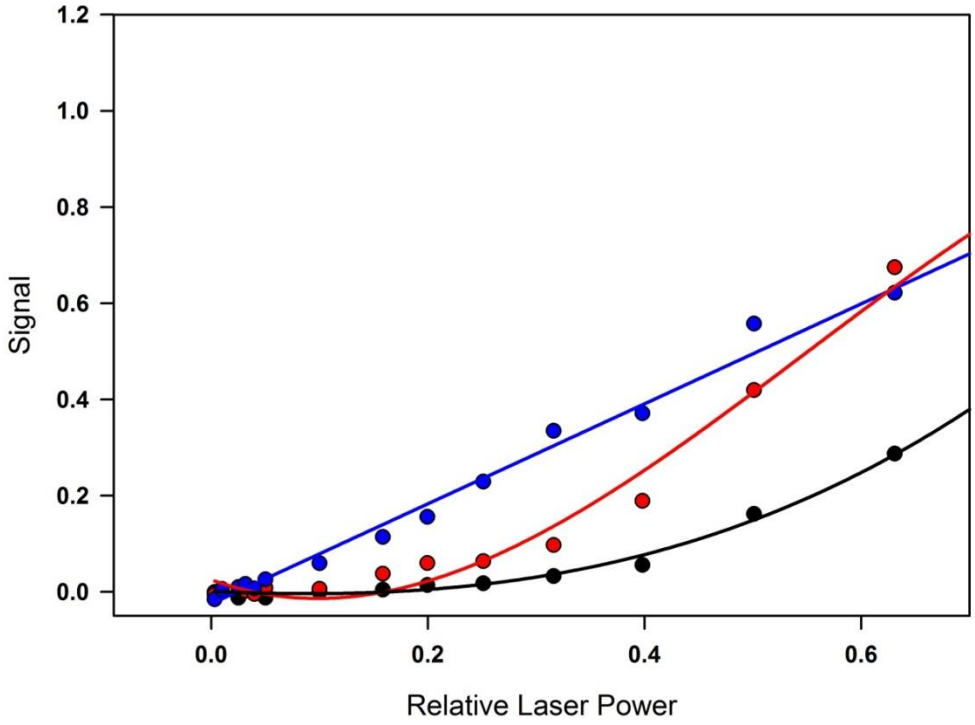

Figure 47: Power dependence plots for CO_2 loss at three different wavelengths. BLUE: 560nm, RED: 520nm, BLACK: 480nm.

In the sector instrument, the vacuum is much higher at ~10^{-6} than the ~3mTorr of He gas in the trap so collisions with neutrals is much less likely to occur especially given the differences in the time scales of the two instruments.

Rhodamine dye ions are known to form triplet states in the gas phase.[10] Rhodamine ions stored in a quadrupole ion trap for fluorescence studies were shown to be able to be optically pumped into a "dark" triplet state. Reaction with dioxygen in the buffer gas quenched the "dark" triplet state and returned the ions to the excitation-fluorescence cycle. We posit that a similar phenomenon is happening with our action absorbance spectra of rhodamine B. At wavelengths of 520nm and 480nm the rhodamine B system can be excited to a state (A) above the triplet ground state in energy (as shown in Figure 14 below). This state can then cross to the lower energy non-dissociating triplet ground state.

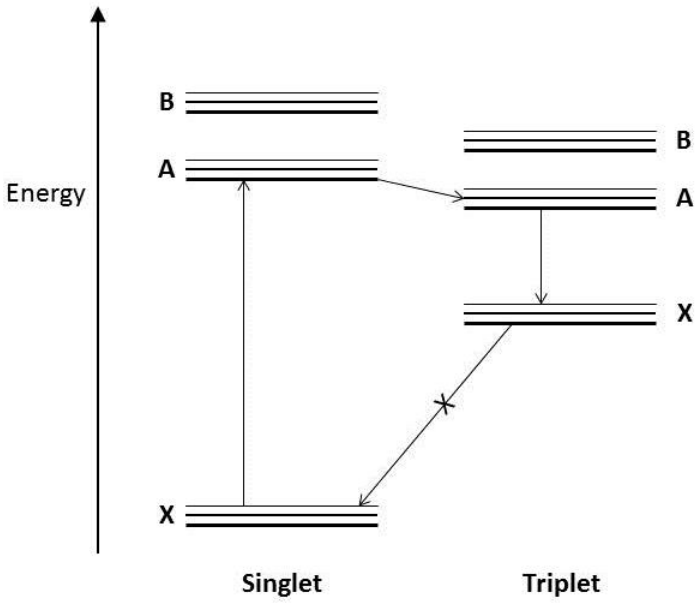

Figure 48: Jablonski diagram showing the ground (X) singlet and triplet states as well as the first (A) and second (B) excited states for each spin multiplicity. The transition between ground states is shown with an X through it to indicate that our experiments cannot observe such a transition.

Energies calculated for the rhodamine B spin systems are shown in Table 3. These values are close to the values reported by Greisch et al.[5] As can be seen in the table, the calculated values show a slight energy gap between the energies of the 480 or 520nm photons and the gap between the singlet ground and first excited states. All TD-DFT calculations are known to exaggerate the first excited state energy values and there are likely to be improvements to energy values for ground state structures if calculated using higher basis sets. Such considerations show that our model cannot be rejected purely from computational considerations.

In addition to rhodamine dyes, there is evidence of similar phenomena within nitrosyl heme systems.[11] These results suggest that "dark" triplet states can form for these systems as well and require multi-photon processes to dissociate and that dissociations requiring fewer, lower energy photons are simultaneously possible.

Relative Rhodamine B Energies (eV)									
State	**X**	**A**	**B**	**C**	**D**	**E**	**F**	**G**	**H**
Singlet	0	2.93	3.67	4.41	4.42	4.71	4.75	4.89	5.08
Triplet	1.83	2.66	3.17	4.08	4.09	4.32	4.51	4.55	4.59

Table 23: CAM-B3LYP/6-311++G(2d,p) single point energies for singlet and triplet ground (X) states and first 8 excited states (A-H) from CAM-B3LYP/6-31+G(d,p) optimized structures.

The triplet state can be stable such that no decay to the ground singlet state occurs without a triplet quencher present.[10] Absorbance of additional photons provides the necessary energy to rise to an excited state and dissociate. The energy for the first excited singlet state is such that photons at energies of 560nm are too low for it to be reached and instead proceeds directly to dissociation.

6.4. Conclusions

The action absorbance spectrums of doubly and singly charged GLGGK* peptide, crystal violet and rhodamine B were measured on both an ion trap type and sector type mass spectrometer and compared to theoretically predicted absorbances. The charge state appeared to have little to no influence on the location of the absorbance band for the diazirine chromophore. Crystal Violet experimental action absorbance bands showed poor agreement with computationally predicted absorbance bands utilizing the best methods available to our group, showing poor agreement for location and even a mismatched number of absorbances. Power dependence measurements showed that crystal violet double methane loss was not a lower energy process than single methane loss. Rather it showed that the double methane loss channel required an additional photon over that of the single methane loss. Rhodamine B also showed poor agreement between our experimental measurements and absorbances predicted computationally. Additionally, rhodamine B showed interesting behaviors indicating the possibility of a long-lived triplet state being formed and requiring additional photon absorbance events to fragment from that state.

6.5. Acknowledgements

I wish to thank Professor Steen Brønsted Nielsen and the members of his research group in the department of Physics and Astronomy at Aarhus University in Aarhus, Denmark for their hospitality during my visits to their lab and their assistance with acquisition of the sector based action spectroscopy data. It was a very rewarding experience visiting and one I will always be grateful for having had.

6.6. References

(1) Pedersen, S. Ø.; Byskov, C. S.; Turecek, F.; Nielsen, S. B. *J. Phys. Chem. A* **2014**, *118* (24), 4256–4265.

(2) Byskov, C. S.; Weber, J. M.; Nielsen, S. B. *Phys. Chem. Chem. Phys.* **2015**, *17* (8), 5561–5564.

(3) Korneev, S. M. *Eur. J. Org. Chem.* **2011**, *2011* (31), 6153–6175.

(4) Sagoo, S. K.; Jockusch, R. A. *J. Photochem. Photobiol. Chem.* **2011**, *220* (2–3), 173–178.

(5) Greisch, J.-F.; Harding, M. E.; Kordel, M.; Klopper, W.; Kappes, M. M.; Schooss, D. *Phys. Chem. Chem. Phys.* **2013**, *15* (21), 8162.

(6) Goerigk, L.; Grimme, S. *J. Chem. Phys.* **2010**, *132* (18), 184103.

(7) Carpino, L. A.; Han, G. Y. *J. Am. Chem. Soc.* **1970**, *92* (19), 5748–5749.

(8) Merrifield, R. B. *J. Am. Chem. Soc.* **1963**, *85*, 2149–2154.

(9) Schwartz, J. C.; Senko, M. W.; Syka, J. E. P. *J. Am. Soc. Mass Spectrom.* **2002**, *13* (6), 659–669.

(10) Kordel, M.; Schooss, D.; Neiss, C.; Walter, L.; Kappes, M. M. *J. Phys. Chem. A* **2010**, *114* (17), 5509–5514.

(11) Wyer, J. A.; Jørgensen, A. V.; Møller Pedersen, B.; Brøndsted Nielsen, S. *ChemPhysChem* **2013**, *14* (18), 4109–4113.